EXPERIMENTAL INVESTIGATIONS OF THE CHARACTERISTICS OF LOW AND ATMOSPHERIC PRESSURE PLASMAS

by

Turgay Çoruhlu

Submitted to Graduate School of Natural and Applied Sciences
in Partial Fulfillment of the Requirements
for the Degree of Doctor of Philosophy in
Physics

Yeditepe University

2022

EXPERIMENTAL INVESTIGATIONS OF THE CHARACTERISTICS OF LOW AND ATMOSPHERIC PRESSURE PLASMAS

APPROVED BY:

Prof. Dr. Necdet Aslan .....
(Thesis Supervisor)
(Yeditepe University)

Prof. Dr. S. Sinan Keskin .....
(Marmara University)

Prof. Dr. Metin Turan .....
(Yeditepe University)

Prof. Dr. Uğur Yahşi .....
(Marmara University)

Assist. Prof. Dr. Serhat Iştın .....
(Yeditepe University)

DATE OF APPROVAL: ..... / ..... / 20.....

I hereby declare that this thesis is my own work and that all information in this thesis has been obtained and presented in accordance with academic rules and ethical conduct. I have fully cited and referenced all material and results as required by these rules and conduct, and this thesis study does not contain any plagiarism. If any material used in the thesis requires copyright, the necessary permissions have been obtained. No material from this thesis has been used for the award of another degree.

I accept all kinds of legal liability that may arise in case contrary to these situations.

Name, Last Name Turgay Çoruhlu

Signature .....

ACKNOWLEDGEMENTS

There would be a long list of who are support me. I would like to thank:

Prof. Dr. Necdet Aslan: for accepting me as a doctoral student, teaching and guiding me during my work.

Prof. Dr. Uğur Yahşi and Prof. Dr. S. Sinan Keskin from Marmara University: for their support and constructive criticism throughout my doctoral studies.

Assoc. Prof. Dr. Ercüment Akat: for his role as a thesis follow-up committee member.

Decedent Prof. Dr. Peter Pokrowsky (R.I.P): for realizing my visit to Zweibrücken, Germany, and introducing me to nano-world.

Detlev Cassell and Rainer Lilischkis: for their help me in using cleanroom and metrology laboratory of Hochschule Kaiserslautern.

Sedat Bayraklı: for his life-saving technical help, particularly when my computer got down twice.

Sabriye Ana, my grandfather Fehmi Çoruhlu, aunt İsmet Çoruhlu for their support and encouragement.

Davut Şişman, my inspirational mathematics teacher from İyidere High School, who read poems regularly as well as teaching algebra and geometry.

Lotha, Felix, Reuben, Anna, Tina, and Miriam of Hochschule Kaiserslautern; and Mehmet, Melda, Tuba, Kenan, Eylem, Mostafa and Eray of Yeditepe University: for creating friendly and joyful working atmosphere.

Mikail Halil, my beloved son; and a beautiful, stubborn, and self-sacrificing Black Sea woman, Fahriye Kurt, my mother: for their unconditional love and morale.

ABSTRACT

EXPERIMENTAL INVESTIGATIONS OF THE CHARACTERISTICS OF LOW AND ATMOSPHERIC PRESSURE PLASMAS

In this thesis, the technological applications of low and atmospheric pressure plasmas in different industrial fields such as medicine, energy, and agriculture have been studied experimentally.

First, silver and copper metals were coated with magnetron sputtering on cotton fabric for medical applications such as preventing hospital-acquired infections. Studies with Escherichia coli and Staphylococcus aureus bacteria have shown that metal-coated textiles are more antibacterial than uncoated ones.

Secondly, single-layer indium tin oxide (ITO) and three-layer ITO/Ti/ITO (ITI) structures on glass were fabricated by magnetron sputtering method and characterized for photovoltaic applications. It has been qualitatively demonstrated that the ITI structure, in which titanium is used as the intermediate metal layer, is up to three times more conductive than the electrode using only ITO, without compromising its transparency. It has been reported for the first time that ITI structures show Surface Plasmon Resonance (SPR) effect.

Finally, it has been shown that the treatment of tea seeds (Camellia Sinensis [L.] Kuntze) with cold atmospheric plasma enhances seed germination, seedling growth, plant hormones, and antioxidant enzyme activities.

ÖZET

DÜŞÜK VE ATMOSFERİK BASINÇ PLAZMALARIN KARAKTERİSTİKLERİNİN DENEYSEL İNCELENMESİ

Bu tezde düşük ve atmosferik basınç plazmaların tıp, enerji ve tarım gibi farklı endüstriyel alanlardaki teknolojik uygulamaları deneysel olarak calışılmıştır.

İlk olarak hastane kaynaklı enfeksiyonları önlemek gibi medikal uygulamalar için mıknatıssal saçtırma yöntemi ile pamuk kumaş üzerine gümüş ve bakır metaller kaplanmıştır. Escherichia coli ve Staphylococcus aureus bakterileriyle yapılan çalışmalarda metal kaplanmış tekstillerin kaplanmamış olanlara göre daha antibakteriyel olduğu gösterilmiştir.

İkinci olarak, fotovoltaik uygulamalar için mıknatıssal saçtırma yöntemi ile cam üzerine tek katmanlı indiyum kalay oksit (ITO) ve üç katmanlı ITO/Ti/ITO (ITI) yapılar üretilmiştir ve karakterizasyonu yapılmıştır. Titanyumun ara metal katmanı olarak kullanıldığı ITI yapısının sadece ITO kullanılan elektrota göre saydamlık özelliğini yitirmeden üç kata kadar daha iletken olduğu gösterilmiştir. ITI yapısının Yüzey Plazmon Rezonans (SPR) etkisi gösterdigi ilk kez rapor edilmiştir.

Son olarak, çay tohumlarının (Camellia Sinensis [L.] Kuntze) soğuk atmosferik plazma ile muamele edilmesinin tohum çimlenmesi, fide büyümesi, bitki hormonları ve antioksidant enzimlerin aktivitesini arttırdığı gösterilmiştir.

TABLE OF CONTENTS

ACKNOWLEDGEMENTS iv
ABSTRACT v
ÖZET vi
TABLE OF CONTENTS vii
LIST OF FIGURES x
LIST OF TABLES xiv
LIST OF SYMBOLS/ABBREVIATIONS xvi
1. INTRODUCTION 1
1.1. MOTIVATION AND OUTLINE OF THE DISSERTATION 1
1.2. PLASMA PHYSICS AND TECHNOLOGY 2
1.2.1. Definition and Historical Remarks 2
1.2.2. Classification of Plasmas 4
1.2.3. Applications of Plasma Technology 6
1.3. PLASMA CHARACTERISTICS 7
1.3.1. Distribution functions, plasma temperature 8
1.3.2. Debye Length 9
1.3.3. Plasma Frequency 10
1.3.4. Composition - Ionization Degree 11
1.3.5. Magnetized - Nonmagnetized Plasmas 11
1.3.6. Criteria of Plasma 12
1.4. DISCHARGE IGNITION 12
1.4.1. Breakdown in DC fields 13
1.4.2. Breakdown in High Frequency Fields 14
1.4.3. Glow Discharge Plasma 15
1.5. SUSTAINMENT OF DISCHARGES 16
2. THIN FILM TECHNOLOGY: DEPOSITION TECHNIQUES AND PROCESSES ... 19
2.1. THIN FILM GROWTH 20
2.1.1. Film Structure 20
2.2. INTERACTIONS OF IONS WITH SURFACES 22
2.3. SPUTTERING TECHNOLOGY 24

2.3.1. The Mechanism of Sputtering....24
2.3.2. Sputtering as a Deposition Process....26
2.3.3. DC-Diode Sputtering....27
2.3.4. RF Sputtering....27
2.3.5. Bias Sputtering....29
2.3.6. Reactive Sputtering....29
2.3.7. Magnetron Sputtering....30
3. CHARACTERIZATION TOOLS AND METHODS....35
3.1. DETERMINATION OF FILM THICKNESS....35
3.1.1. Stylus-Method Profilometry....35
3.1.2. Quartz Crystal Microbalances....36
3.2. MEASUREMENT OF OPTICAL TRANSMITTANCE....39
3.2.1. Spectroscopic Ellipsometry....39
3.2.2. Photoluminescence Spectroscopy....42
3.3. MEASUREMENT OF SHEET RESISTANCE....44
3.4. SURFACE MORPHOLOGY....48
3.4.1. Scanning Electron Microscopy....48
3.4.2. Energy Dispersive X-Ray Spectroscopy....51
3.4.3. Atomic Force Microscopy....52
3.5. ASSESSMENT OF ANTIBACTERIAL ACTIVITY OF TEXTILES....54
3.6. HIGH PERFORMANCE LIQUID CHROMATOGRAPHY....55
4. ANTIBACTERIAL TEXTILES....58
4.1. EXPERIMENTAL DETAILS....58
4.1.1. Coating of Cotton Textiles....58
4.1.2. Parallel Streak Method....58
4.2. RESULTS AND DISCUSSION....59
4.2.1. Antibacterial Activity of Ag Coated Cotton Towards Escherichia coli and Staphylococcus aureus....59
4.2.2. Antibacterial Activity of Cu-Coated Cotton Towards Escherichia coli and Staphylococcus aureus....61
4.2.3. Antibacterial Activity of Ag Coated Lancet Towards Escherichia coli and Staphylococcus aureus....62

4.2.4. Mechanism of Action....63
5. TRANSPARENT AND CONDUCTIVE ELECTRODES....69
5.1. TRANSPARENT CONDUCTIVE OXIDES....69
5.1.1. Indium Tin Oxide....70
5.1.2. ITO/Metal/ITO Structures....71
5.2. EXPERIMENTAL DETAILS....72
5.2.1. The First Set of Experiments....75
5.2.2. The Second Set of Experiments....76
5.2.3. The Third Set of Experiments....79
5.3. RESULTS AND DISCUSSION....87
5.3.1. Structural Composition....87
5.3.2. Sheet Resistance....88
5.3.3. Optical Transparency....89
5.3.4. Lorentz and Drude Models....89
5.3.4.1. Surface Plasmon Resonance....94
5.3.4.2. Plasmonic Quality Factor....95
6. COLD ATMOSPHERIC PLASMA TREATMENT OF TURKISH TEA SEEDS....98
6.1. PLASMA AGRICULTURE....98
6.2. PLASMA TREATMENT OF TEA....98
6.3. EXPERIMENTAL WORK....100
6.4. RESULTS AND DISCUSSION....101
6.4.1. Seed Germination and Seedling Growth....101
6.4.2. Surface Properties....102
6.4.3. Plant Hormones and Antioxidant Enzyme Activity....103
7. CONCLUSIONS....110
REFERENCES....111

LIST OF FIGURES

Figure 1.1. The four states of matter [2] 2

Figure 1.2. Areas of plasma processing applications [6] 6

Figure 1.3. Paschen curves for DC electric field 14

Figure 1.4. Types of self-sustaining gas discharges 15

Figure 1.5. Basic processes occur in glow discharge plasma 17

Figure 2.1. Thin film growth techniques 19

Figure 2.2. Structure zone model developed by Movchan, and extended by Thornton and Anders [10] 21

Figure 2.3. Thin film growth modes 23

Figure 2.4. Interactions of ions with surfaces 24

Figure 2.5. The phases of thin film formation 26

Figure 2.6. Particles bombarding the substrate in sputter deposition 28

Figure 2.7. NANOVAK NVSS350 Magnetron Sputtering System 30

Figure 2.8. Schematic of NANOVAK Magnetron Sputtering System 31

Figure 2.9. Side view of NANOVAK Magnetron Sputtering System 32

Figure 2.10. Top view of NANOVAK Magnetron Sputtering System 33

Figure 2.11. VAKSIS PVD Handy 3M Magnetron Sputtering System 33

Figure 2.12. VAKSIS Dual DC and RF Magnetrons 34

Figure 3.1. Schematics of stylus profilometer 36

Figure 3.2. DEKTAK3 Surface Profilometer 37

Figure 3.3. NanoMap 500LS Scanning Contact Surface Profilometer 38

Figure 3.4. Ellipsometry technique....40

Figure 3.5. SENTECH SE850 Ellipsometry....41

Figure 3.6. Acton SP2300A Spectrometer....43

Figure 3.7. Linear arrangement of one, two and four point probe....45

Figure 3.8. Square arrangement of four point probe....46

Figure 3.9. Sheet resistance measurement system consist of (a) semiconductor parameter analyzer and (b) four point probe head....48

Figure 3.10. The resulting electrons and photons after the electron beam interacts with the sample....49

Figure 3.11. Schematic view of SEM components....50

Figure 3.12. Thickness of thin films can be determined by using SEM....51

Figure 3.13. Schematic view of AFM components....52

Figure 3.14. Resolution of HPLC....56

Figure 4.1. E. coli with (a) Ag coated cotton, and (b) uncoated textile....60

Figure 4.2. S. aureus with (a) uncoated textile, and (b) Ag coated cotton....61

Figure 4.3. Control (a) S. aureus and (b) E. coli....64

Figure 4.4. Cu coated cotton with (a) S. aureus and (b) E. coli....65

Figure 4.5. E. coli with (a) Ag coated and (b) uncoated lancet....66

Figure 4.6. S. aureus with (a) uncoated and (b) Ag coated lancet....67

Figure 5.1. Crystal structure of ITO....70

Figure 5.2. Top view of IMI deposition....72

Figure 5.3. Side view of IMI structures....73

Figure 5.4. ITO monolayer and IMI trilayer structures....74

Figure 5.5. ITO monolayer deposition....77

Figure 5.6. ITO-Ag-ITO multilayers on glass....78

Figure 5.7. The cracks due to the temperature of the magnetron sputtering....79

Figure 5.8. EDX analysis of IAI multilayer thin films....80

Figure 5.9. SEM images of the cross-sections of ICI and ITI on glass for SE-2....81

Figure 5.10. EDX Analysis of IAI Multilayer for SE-2....81

Figure 5.11. EDX Analysis of ICI Multilayer for SE-2....82

Figure 5.12. EDX Analysis of ITI Multilayer for SE-2....83

Figure 5.13. AFM images of the intermediate layer of IAI and ICI structures for SE-2....83

Figure 5.14. AFM images of the incorporated layer of ITI with different coating times of Ti for SE-2....84

Figure 5.15. Transmission spectra of ITO monolayers and ITI multilayers for SE-2....85

Figure 5.16. Profilometry for deposition rate for ITO (VAKSİS) for SE-3....86

Figure 5.17. SEM images of the cross-sections of ITO and ITI deposited on glass for SE-387

Figure 5.18. Optical transmittance of ITO and ITI thin films on glass for SE-3....90

Figure 5.19. Transmittance spectra of ITO and ITI thin films deposited on SLG for SE-3.91

Figure 5.20. Transmittance spectra of ITO and ITI thin films deposited on BK7 for SE-3.92

Figure 5.21. Excitation of surface plasmons (D:Dedector, L:Laser,M:metal)....95

Figure 5.22. SPR intensity of Ti....96

Figure 5.23. Comparison of SPR intensities of Ag, Cu, and Ti....97

Figure 6.1. Home-made CAP system: 1) Earthing, 2) HV electrode, 3) air inlet, 4) ground electrode, 5) nozzle, 6) plasma plume, and 7) tea seeds 100

Figure 6.2. Plasma-treated samples are 3-fold greater than the controlled group 102

Figure 6.3. (a) 2-minute, and (b) 4-minute PTS and the control sample 103

Figure 6.4. 2019 set 104

Figure 6.5. Seed germination rate 105

Figure 6.6. (a) Seed germination percentage, (b) Germination index 106

Figure 6.7. SEM images plasma treated and untreated tea seeds 107

Figure 6.8. HPLC results for antioxidant enzyme activities 108

Figure 6.9. HPLC results for plant hormones activities 109

LIST OF TABLES

Table 1.1. Classification of plasmas....5

Table 4.1. Deposition parameters for Ag and Cu coatings....59

Table 4.2. Explanations of symbols used in tables for antibacterial activity....59

Table 4.3. Inhibition zones of uncoated cotton with E. coli and S. aureus....62

Table 4.4. Inhibition zones of Ag-coated cotton with E. coli....62

Table 4.5. Inhibition zones of Ag-coated cotton with S. aureus....63

Table 4.6. Inhibition zones of Cu coated cotton with E. coli....63

Table 4.7. Inhibition zones of Cu coated cotton with S. aureus....65

Table 4.8. Inhibition zones of uncoated lancet (E. coli and S. aureus Control)....66

Table 4.9. Inhibition zones of silver coated lancet for E. coli....67

Table 4.10. Inhibition zones of silver coated lancet for S. aureus....68

Table 5.1. The classification of conducted experiments....73

Table 5.2. Deposition parameters of IAI for SE-1....75

Table 5.3. The coating time and thicknesses of ITO monolayers SE-1....75

Table 5.4. Measurement of the film thickness of IAI multilayers SE-1....75

Table 5.5. Deposition parameters of SE-2....76

Table 5.6. The structure of the samples prepared for SE-3....85

Table 5.7. Deposition conditions for SE-3....87

Table 6.1. Literatur review on plasma treatment of tea....99

Table 6.2. Process parameters for seed treatment....101

Table 6.3. Investigated phytohormones and antioxidant enzymes. 106

LIST OF SYMBOLS/ABBREVIATIONS

Cu	Copper
Ag	Silver
Ti	Titanium
ITO	Indium tin oxide
TCO	Transparent conductive oxide
IAI	ITO/silver/ITO
ICI	ITO/copper/ITO
ITI	ITO/titanium/ITO
SE-1	First set of experiments
SE-2	Second set of experiments
SE-3	Third set of experiments
R_s	Sheet resistance
APPJ	Atmospheric pressure plasma jet
CAP	Cold atmospheric plasma
GD	Glow discharge
MS	Magnetron sputtering
NP	Nano particle
Q_f	Quality factor
SPO	Surface plasma oscillations
SPR	Surface plasmon resonance
AFM	Atomic force microscopy
SEM	Scanning electron microscopy
EDX	Energy dispersive X-ray spectroscopy
HPLC	High Performance Liquid Chromatography
PTS	Plasma treated samples
LB	Luria-Bertani

1. INTRODUCTION

1.1. MOTIVATION AND OUTLINE OF THE DISSERTATION

In this dissertation, the applications of low and atmospheric pressure plasmas in different branches of industry such as energy, medicine, and agriculture are investigated. It consists of the following chapters:

Chapter 1 reviews plasma physics and technology through definition, classification, characteristics and applications of plasmas.

Chapter 2 briefly mentions about thin film deposition techniques and then gives the basics of magnetron sputter deposition and the properties of glow discharge in detail.

Chapter 3 gives the theory and working principles of the characterization tools or methods used in this study. This includes stylus profilometry, spectroscopic ellipsometry, scanning electron microscopy, atomic force microscopy, four point probe method, high-performance liquid chromatography, and antibacterial activity assessment protocols.

Chapter 4 is related to the application of magnetron sputtering for antibacterial surface treatment of textiles. In this chapter, the results of antibacterial activity tests of metal coated textiles are presented.

Chapter 5 is about another application of magnetron sputtering for photovoltaics. ITO-metal-ITO multilayer structures as transparent conductive electrodes are investigated. Optical transmittance and electrical conductance results are demonstrated.

Chapter 6 is about plasma agriculture. The effects of cold atmospheric plasma treatment on seed germination, plant hormones and antioxidant activity of tea seeds are demonstrated.

Chapter 7 summarizes the main results and highlights original contributions.

1.2. PLASMA PHYSICS AND TECHNOLOGY

1.2.1. Definition and Historical Remarks

Plasma is significantly ionized gas which is generally known as the 4 th state of matter. It consists of charged and neutral particles: electrons, ions, photons, atoms, free radicals, molecules, etc. Macroscopically plasma is a quasi-neutral particle system that exhibits collective behavior and obeys Maxwell-Boltzmann statistics [1]. Everything was plasma at the beginning of the universe, so it is also called as the first state of matter, and 99% of the visible universe is in the plasma state. The Sun, the majority of stars, and a sizeable portion of the interstellar medium are included. Consequently, plasmas are fundamental to the universe.

Historically, although William Crokes defined plasma as radiant matter in 1879, it was Irving Langmuir who invented term "plasma" for the first time in 1928. He stated that the ionized gas contains equal number ions and electrons, which is called plasma approximation, and described this balanced region as plasma.

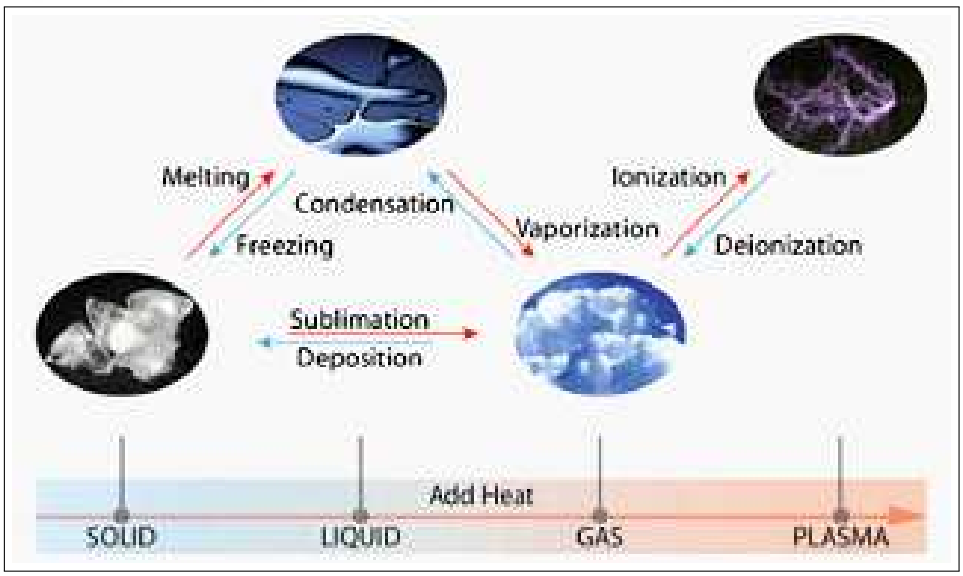


Figure 1.1. The four states of matter [2]

If enough energy is provided to matter, the four states of matter can exist as shown in Figure 1.1. The solid matter becomes a liquid by melting and is converted into a gas by vaporizing. Supplying further energy results in dissociation of the individual atoms into positively charged ions and electrons, so called ionization, and the gas turns into plasma phase.

Any ionized gas is not defined as a plasma since there is some degree of ionization in any gas. The amount of ionization is low until the ionization energy U is only a few times $k_B T$, where T is the gas temperature in Kelvin, and k_B is the Boltzmann constant. The plasma becomes fully-ionized if the temperature is increased further. This explains why plasmas exist at high temperatures, i.e. million degrees in the center of the Sun.

Plasmas can be classified as natural and man-made. The examples of natural plasmas are lightning and Northern lights. The examples of man-made plasmas are neon lights and welding arcs.

The development of solar flares and sunspots, the acceleration of high-velocity winds that travel outward from the Sun and other stars, the production of radio emissions from the Sun and other astrophysical objects, the formation of planetary radiation belts, and the acceleration of cosmic rays are all related to plasma physics.

Except in exceptional circumstances, the low temperatures and high pressures that are frequently seen in the Earth's atmosphere do not favor the production of plasmas. Lightning is most likely the plasma phenomenon that occurs in the ionosphere of the Earth most frequently. The electrical currents in a lightning discharge cause the atmospheric atmosphere to become ionized and heat up to a very high temperature. Due to the high rate of recombination, the resultant plasma only lasts for a small scale of a second. Ball lightning described as tiny luminescent spherical object is a rare phenomenon usually associated with thunderstorms and can last up to tens of seconds.

The aurora is another occurrence of terrestrial plasma that is easily seen at high latitudes and is caused by high energy electrons and ions hitting the atmosphere at altitudes of $80-100\ km$. At higher altitudes, between 100 and several hundred kilometers, a thick plasma called the ionosphere surrounds the Earth. Because of low recombination rate at high altitudes, the ionospheric plasma is created by UV radiation from the Sun and also occurs on the darkside of the Earth. As a reflector for low-frequency radio signals, the ionosphere is crucial for radio communication.

At much higher altitudes, a zone of magnetized plasma called the magnetosphere surrounds the Earth. All of the magnetized planets have now had their planetary magnetospheres

examined, and they show many of the plasma processes that are thought to take place at magnetized astronomical objects like neutron stars [3].

Basic plasma physics has many industrial applications. The effort to develop controlled thermonuclear fusion is one of the most significant of these. Controlled fusion necessitates extremely high temperatures since fusion requires $10^7\ K$, or more to overcome the Coulomb force nuclei. Fluorescent lights and other numerous plasma-related technologies, including electric arc welders and plasma etching machines, are often used in daily life. High tech devices includes traveling wave tubes, magnetrons, ion engines for spacecraft propulsion, MHD generators that generate energy from high-temperature gas jets, and a variety of surface modification treatment techniques.

1.2.2. Classification of Plasmas

As shown in Table 1.1, there are several parameters to classify plasmas: Temperature, frequency, pressure, etc. (T_e, T_i and T_g are temperatures of electrons, ions and gas, respectively [4]).

The sort of plasma that is best suitable for a given application relies on the needed pressure range. The most frequent method of heating a plasma is to use electrical field ($\vec{E}$). The various inertias of electrons and ions cause the plasma to differ depending on the frequency of the $\vec{E}$. Additionally, since charged species primarily follow the magnetic field $\vec{B}$ lines along with rotation, $\vec{B}$ can be used to control the electrons and ions in a plasma. According to the frequency of the applied $\vec{E}$ utilized for plasma creation, there are four type plasmas [5].:

- DC Plasmas: Plasma is created between cathode and anode electrodes, and a direct current (DC) carried by the free ions and electrons in the plasma flows through the system. When charged species are shielded from the edge of the plasma by $\vec{B}$, the density of the plasma can be increased.

- AC Plasmas (kHz): The ions and electrons are capable of tracking the oscillation of $\vec{E}$, since the frequency of $\vec{E}$ is sufficiently low. Applications requiring great power and a large area commonly use AC plasmas. The current at the electrodes is created by both electrons and ions.

Table 1.1. Classification of plasmas

Parameters	**Type(s)**
Temperature	-low temperature plasmas (less than $2000°K$) -high temperature plasmas (above $2000°$K)
Pressure	-low pressure plasmas $< 0.075\,Torr$ -moderate pressure plasmas $\approx 7.5\,Torr$ -high pressure plasmas
Frequency	-DC discharge -pulsed DC (kHz) -RF discharge (MHz) -microwave discharge (GHz)
Thermodynamic Equilibrium	-nonthermal or nonequilibrium plasmas $T_e >> T_i \approx T_g$ -thermal or equilibrium plasmas $T_e \approx T_i \approx T_g$
Ionization Degree	-weakly ionized plasmas $10^{-6} - 10^{-1}$ -fully ionized plasmas ≈ 1
Neutrality	-neutral -nonneutral
Magnetization	-magnetic -nonmagnetic
Other	dusty plasmas

- RF Plasmas (MHz): An RF plasma has an $\vec{E}$ having a frequency similar to radio waves. Since the $\vec{E}$ is so strong that only electrons can follow its oscillation while ions are essentially at rest. Displacement current, not conduction current, dominates the plasma current. As a result, it is possible to layer non-conducting materials over plasma electrodes, which is necessary for treating insulators like silicon oxide with plasma.

- Microwave Plasmas (GHz): In a GHz plasma, the electrons can simply follow the $\vec{E}$ since the frequency $\vec{E}$ is so high. However, due to an electromagnetic wave's limited skin depth in a conductive medium, the electromagnetic wave cannot fully enter the plasma. Resonant heating of the electrons is made feasible by adding a second $\vec{B}$.

Both at atmospheric pressure and at low pressures, these four different forms of plasma can be produced. These plasmas can approach to thermal equilibrium $T_e \approx T_i \approx T_g$ owing to the high collision rate at high pressures.

1.2.3. Applications of Plasma Technology

Plasma technology has many industrial applications from health to energy as shown in Figure 1.2 [6]. Particularly, low-pressure plasma sources have been implemented in micro-fabrication. The scientific and technological interest in cold atmospheric plasma has been grown recently. Plasma medicine is an emerging field of this technology, which is related with the medical applications of physical plasmas. Similarly, utilization of plasma in agriculture called plasma agriculture have gained popularity recently.

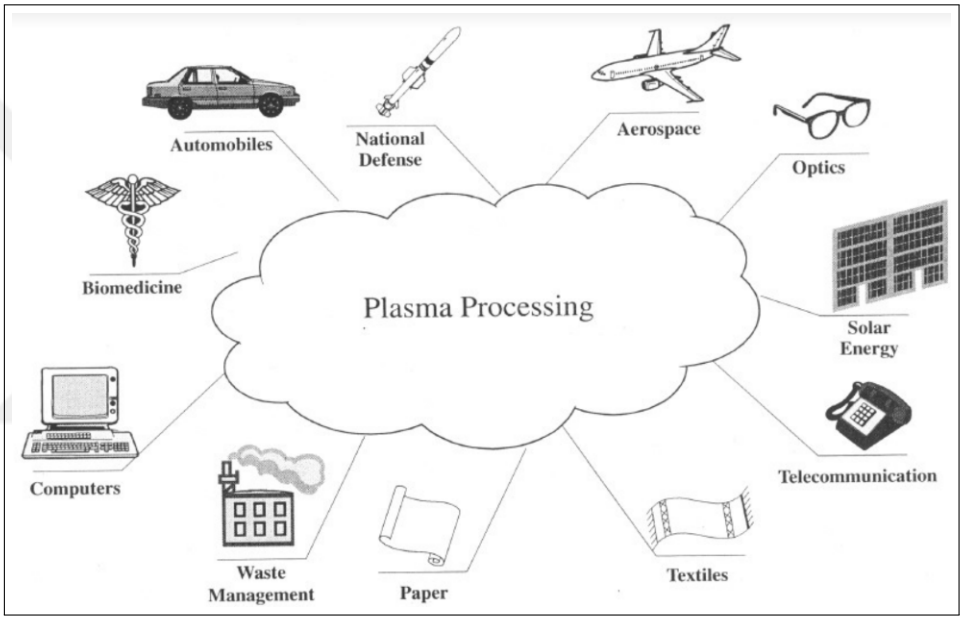


Figure 1.2. Areas of plasma processing applications [6]

Some examples of applications can be given as follows:

- Coatings: Wear or corrosion resistant coatings on tools or metals, optical thin films, high performance ceramics, barrier coatings on plastics, micro-fabrication of integrated circuits
- Plasma etching: Microelectronics.
- Light generation: Plasma lightning (fluorescent or arc lamps), LED, LCD, plasma displays
- Plasma processing: Production of new chemicals and material systems, plasma cutting

- Aeronautics and space: Actuators for next generation airplanes, improved combustion techniques, plasma propulsion
- Environment: Gas conversion, degradation of organic pollutants in water, micro-plasmas for gas sensors
- Plasma medicine: Disinfection and sterilization of medical equipment, blood coagulation, dental care, plasma diagnostics and electro-surgery
- Plasma agriculture: Food preservation, packaging in food industry, seed germination, improved agricultural yield
- Energy: Tokamaks, stellerators

In this work, the applications of low and atmospheric pressure plasmas in the industries of energy, medicine and agriculture were studied. Antibacterial coatings on textiles and lancet, and transparent conducting electrodes for photovoltaic applications were fabricated by using low pressure plasma deposition, and cold atmospheric pressure plasma was used to treat seeds for improving germination.

1.3. PLASMA CHARACTERISTICS

Regarding their distinguishing characteristics, the various plasma types can be defined. These variables characterize the system's crucial length and time scales as well as the energy that is stored in a plasma [5]. These fundamental plasma parameters serve as the foundation for evaluating a given plasma configuration and identifying the best option for a certain application.

1.3.1. Distribution functions, plasma temperature

According to their degrees of freedom, the energy in a plasma is stored in the movement of the plasma species, which can be translational, vibrational, rotational and or electronic excitation. A so-called distribution function $f(\vec{x}, \vec{v})$ that represents the likelihood of finding a single species in the plasma at a given position x in space and the velocity $\vec{v}$ is used to describe

each degree of freedom. Assuming that numerous collisions between the plasma particles result in thermal equilibrium, the distribution function $f(\vec{v})$ for a homogeneous plasma in space is called as Maxwell Boltzmann distribution function (MBDF) (for electrons):

$$f(\vec{v}) = \left(\frac{m}{2\pi k_B T}\right)^{3/2} \exp\left(-\frac{\frac{1}{2}mv^2}{k_B T}\right) \tag{1.1}$$

with m the electron mass, and v the velocity of the electron. From MBDF the average kinetic energy $\overline{E}$ of a particle can be found as:

$$\overline{E} = \frac{\iiint \frac{1}{2}mv^2 f(v) d^3v}{\iiint f(v) d^3v} = \frac{3}{2}k_B T \ . \tag{1.2}$$

It is possible to calculate the root mean square speed $\overline{v}$ which is equal

$$\overline{v} = \sqrt{\frac{8k_B T}{\pi m}} \ .$$

For Argon atoms at $20^0 C, \overline{v} = 394\ m/s$, which is slightly greater than speed of sound.

The particle current density, J_e, (in units: hits per second per m^2) is

$$J_e = \frac{1}{4} n_0 \overline{v} \ ,$$

where n_0 is the number density.

However, in the majority of low temperature plasmas, it is necessary to characterize various species using at least a few MBDFs at various temperatures. Even using individual temperatures in situations where non-equilibrium is prominent is incorrect if $f(\vec{v})$ greatly deviates from the MB distribution.

1.3.2. Debye Length

Since the potential difference $V_p - V_f$ where V_p and V_f are plasma and floating potentials repels electrons, the isolated substrate will gain a net positive charge (a space charge) around it. In glow discharge plasmas, the space charge creates a sheath having the space charge

density ρ.

Poisson's equation gives the relation between potential V with distance x and net space charge in this region:

$$\frac{d^2V}{dx^2} = -\frac{\rho}{\epsilon_0}\,.$$

This is the one-dimensional form of Poisson's equation, where ϵ_0 is the permittivity of free space. Since electric field E is given by

$$E = -\frac{dV}{dx}$$

then

$$\frac{dE}{dx} = \frac{\rho}{\epsilon_0}\,, \tag{1.3}$$

which implies that E changes in regions of net charge. If the density of electron density varies as $n_e(x)$, then Equation (1.3) yields

$$\frac{d^2V}{dx^2} = -\frac{e}{\epsilon_0}\left[n_i - n_e\,(x)\right] \tag{1.4}$$

where $\rho = e(n_i - n_e)$ is used for charge density. Using Boltzmann relation

$$n_e\,(x) = n_e \exp\left(\frac{eV}{kT}\right)$$

and substituting into Equation (1.4) and remembering that $n_e = n_i$ for the undisturbed plasma, we obtain

$$\frac{d^2V}{dx^2} = -\frac{en_i}{\epsilon_0}\left[1 - \exp\left(\frac{eV}{kT}\right)\right]\,.$$

When $eV \ll kT$, using Taylor's expansion one gets

$$\exp\left(\frac{eV}{kT}\right) \approx 1 + \frac{eV}{kT}$$

thus Equation (1.4) turns into

$$\frac{d^2V}{dx^2} \approx \frac{e^2n_i}{kT\epsilon_0}V\,,$$

whose solution is

$$V(x) = V_0 \, exp\left(-\frac{|x|}{\lambda_D}\right)$$

where

$$\lambda_D = \left(\frac{\varepsilon_0 k T_e}{n_e e^2}\right)^{1/2} \cong 7434\left(\frac{T_e}{n_e}\right)^{1/2}$$

is called Debye length. It is the minimum neutral region in neighborhood of a wire in the plasma, where the quasi-neutrality holds. For industrial plasmas $T_e = 3 - 10\,eV$, $n_e = 10^{16-18}\,particles/m^3$ and $\lambda_D \cong 0,1 - 0,5\,mm$.

1.3.3. Plasma Frequency

By analyzing the typical frequencies or time scales of a plasma, one can estimate how it will react to alternating $\vec{E}$. This can be inferred from the straightforward illustration of a plasma volume in which the electrons are dispersed over a distance δ in one direction in front of a background of stationary ions. At the boundaries of the electrodes and vacuum chamber, net positive and negative surface charges are build up as a result of this displacement. An $\vec{E}$ consequently forms, counteracting the initial displacement δ. If the kinematics of the problem is solved for the problem, following characteristic frequency is obtained:

$$\omega_p = \left(\frac{ne^2}{\varepsilon_0 m}\right)^{1/2} \tag{1.5}$$

where ω_p is the frequency of oscillation of plasma. Making a similar derivation for ions, the electron and ion plasma frequencies can be defined by Equation (1.5) using their masses.

Plasma frequency, also called Langmuir frequency, can be written as

$$\omega_p \approx 9{n_e}^{1/2}\,Hz\,.$$

There is a relation between Debye length and plasma frequency:

$$\lambda_D \,.\omega_p = \left(\frac{kT_e}{m_e}\right)^{1/2} \approx \overline{v_e}$$

where $\overline{v_e}$ is the thermal velocity of the electrons in the plasma.

1.3.4. Composition - Ionization Degree

The percentage of the number of charged species to the total number of all plasma species, known as the ionization degree, can be used to describe low temperature plasmas. While DC or RF plasmas have a few percent degree of ionization; in magnetized high density fusion plasmas, it is almost 100%.

It is necessary to have an equal number of + and − charges in a certain volume for the plasma to be quasi-neutral. It is also feasible for negative ions to develop by electron attachment when electronegative plasma gases like O_2 or fluorine are used. The expression for a plasma's degree of electronegativity is $\alpha = n_{neg}/n_e$, and it achieve high values for a plasma mostly made up of + and − ions. After turning off a plasma, a unique circumstance could arise in the afterglow. Unlike an electronegative plasma's afterglow, where the electrons join with the walls and +ions again over a period of a few microseconds, an ion-ion plasma is created when the residual + and − ions decay over a significantly longer period of time.

1.3.5. Magnetized - Nonmagnetized Plasmas

Plasma heating and control are fundamentally based on the sensitivity of plasmas to $\vec{E}$ and $\vec{B}$. Due to the $\vec{B}$ lines restricting their mobility, the employment of $\vec{B}$s specifically enables the formation of high performance plasmas and efficient plasma species confinement. Nevertheless, in the majority of technological plasma systems, the magnetic confinement for ions and electrons may differ. Any magnetic confinement technique requires that the Larmor radius of the charged species be lower than the absolute dimension of the plasma in order for it to work. Furthermore, the Larmor radius must be significantly smaller than the mean free path in order for the charged species to follow the $\vec{B}$ lines instead of being arbitrarily scattered by numerous collision. At low temperatures and low pressures (i.e. Pa), $100\,mT$ is typically utilized in industrial plasmas, at which the electrons are easily magnetized in volume of a few liters. At atmospheric pressures, the very short mean free path prevents any magnetization of the plasma, which would need magnetic field intensities of $10\,T$ or even more.

1.3.6. Criteria of Plasma

For the neutral gas atoms, kinetics energy is equal to thermal energy, i.e.,

$$\frac{1}{2}m\overline{v^2} = \frac{3}{2}kT\,.$$

The averaged energy is characterized by the kT term which has a value of $1/40\ eV$ at $290\ K$.

The number of particles in Debye sphere is given by

$$N_D = \frac{4}{3}\pi\, n_e {\lambda_D}^3 = 1,37x10^6 \frac{T_e^{3/2}}{n_e^{1/2}}$$

and plasma parameter, Λ,

$$\Lambda = 4\pi\, n_e {\lambda_D}^3\,.$$

The plasma criteria are given by:

$$L \gg \lambda_D \quad , \quad \Lambda \gg 1$$

1.4. DISCHARGE IGNITION

Plasmas are mainly created by electric discharges. The process of creating free charge carriers in a dielectric medium due to an external field results in the production (breakdown or ignition) of such discharges. The breakdown process is an antagonism between production and loss of free charge carriers, and takes place over a threshold described by a breakdown E_b or breakdown voltage V_{bd}. Typically, the V_{bd} is higher than the required voltage to maintain the discharge. The threshold value is influenced by the chemical structure and density of the medium, the frequency of the applied field, the geometry and material of the electrodes.

1.4.1. Breakdown in DC fields

The $\vec{E}$ created between the cathode and anode gives the free electrons the energy they need to ionize the atoms in the medium around them. Thus, the number of free electrons grows

exponentially, which is also called avalanche. The avalanche forms both in time and space in DC fields as the electrons float along the $\vec{E}$. The first Townsend coefficient, α, describes the process empirically, and it can be written as

$$\alpha = Ap \exp(-Bp/E)\,, \tag{1.6}$$

where A and B are constants dependent on the gas, and p is the pressure of the gas.

The volumetric particle losses per unit length is given by the second Townsend coefficient β. These losses can be result from both electron attachment or recombination in the gas volume. Volumetric losses are mostly neglected and hence this parameter is usually omitted.

The surface generation of electrons is described by the third Townsend coefficient γ. Typically, it indicates how many secondary electrons were released per ion that impinged on the walls. Secondary electrons can, however, also be emitted as a result of photon absorption or metastables. The third Townsend coefficient of the secondary electrons generated by ion impact is defined as γ_i.

The breakdown takes place between anode and cathode electrodes at a distance d and the electrons move towards the anode. The electrons in the electron avalanche must be sacrificed for the discharge to proceed after they reach the anode. Therefore, new seed electrons are required. The seed particles in a self-sustaining discharge are ejected from the cathode by secondary electron emission from impinging ions. It is crucial for charge carrier amplification that the number of ions produced during ionization can reproduce enough seed electrons to generate the same number of ions during the avalanche process as in the previous stage. This give rise to a phenomenon called as the Paschen criterion.

It provides a relationship between V_{bd}, and the product of discharge gap and the pressure of gas, $p \cdot d$:

$$V_{bd} = \frac{B(pd)}{C + ln(pd)}\,. \tag{1.7}$$

Here, the constants A and B are the same as in Equation (1.6) and $C = ln\frac{A}{ln(1/\gamma_i+1)}$. Scaling laws are applicable since V_{bd} depends on the product pd not two parameters solely. Figure

1.3 shows the characteristics form of the Paschen curve for DC field. It has a minimum at:

$$(pd)_{min} = \frac{exp(1)}{A} ln\,(1/\gamma_i + 1)\ ,\quad V_{min} = B(pd)_{min} \tag{1.8}$$

and V_{bd} increases steeply for $pd < (pd)_{min}$. This necessitates a large boost in the $\vec{E}$ and ionization efficiency. When pd is greater than $(pd)_{min}$, V_{bd} increases almost linearly with pd since $\vec{E}$ shrinks in wider gaps, resulting in a slower acceleration of the electrons, The breakdown voltage must be raised to make up for this because at higher pressures, the electrons collide too frequently and lose energy before they can ionize.

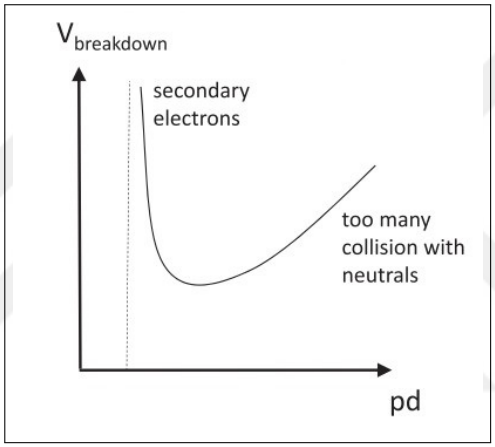


Figure 1.3. Paschen curves for DC electric field

1.4.2. Breakdown in High Frequency Fields

The electron avalanche may only form in time at high frequencies, not in space, which makes the plasma breakdown under oscillating $\vec{E}$ different from the DC case. In such instance, additional mechanisms are needed since the displacement current flows instead of a DC current, which was once necessary to maintain a continuous discharge. The essential equilibrium at alternating $\vec{E}$s must be maintained in the time average as a balance between energy gained from the $\vec{E}$ and losses due to electron collisions with the neutral gas.

1.4.3. Glow Discharge Plasma

The applied voltage and current determine the kind of discharge that develops following the breakdown: Townsend discharge, normal glow discharge (GD), abnormal GD, or arc discharge. Since no external ionizing agent, such as heat or X-ray radiation, is required to sustain any of these discharges, they are called as self-sustaining [16].

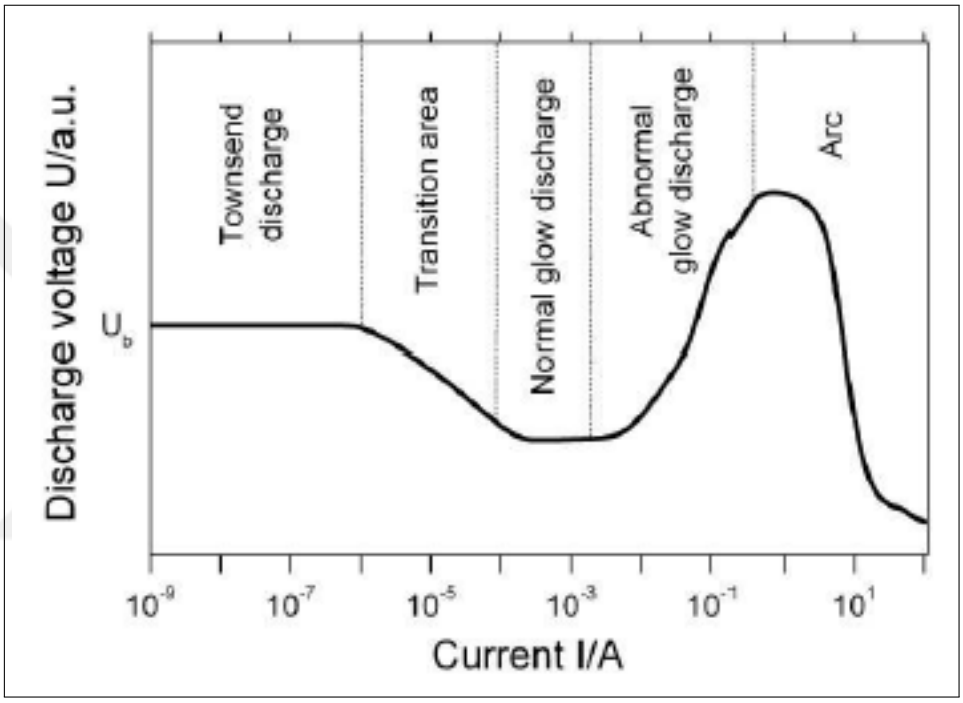


Figure 1.4. Types of self-sustaining gas discharges

The Townsend discharge's ionization degree is so low that the charge density has no impact on the $\vec{E}$ since the voltage is equal to the breakdown potential U_b. The voltage across the electrodes starts to fall at increasing currents (for instance, at elevated pressures), but after a certain current, the decline ceases, demonstrating the normal GD. The crucial peculiarity of this mode is that the current density does not fluctuate. When the cathode area is completely used up, the current density begins to rise, increasing the voltage as well. The ascending area of the $U - I$ curve in Figure 1.4 corresponds to this discharge, which is considered abnormal. An arc develops when the discharge current is sufficiently high (about $1\ A$).

The following parameters are necessary for the GD to form: a relatively low pressure of $1 - 10\,Torr$, a low current of $10^{-6} - 10^{-1}\ A$, and a relatively high voltage of several hundred

to thousands of volts.

The typical normal GD has some varying dark and bright regions. The diversity in the speeds of ion and electrons; and distinct energy of electrons repelled from the cathode owing to the negative cathode potential determines those regions.

The fundamental processes occur in GD plasma are depicted in Figure 1.5. The ground state and excited states are indicated, respectively, by superscripts 0 and $*$. The argon metastable atoms are represented by Arm^*. The bombardment of the negatively charged cathode with the positive ions leads to secondary electron emission and resulting in the ejection of the atoms from the cathode, so called sputtering (See Section 2.3).

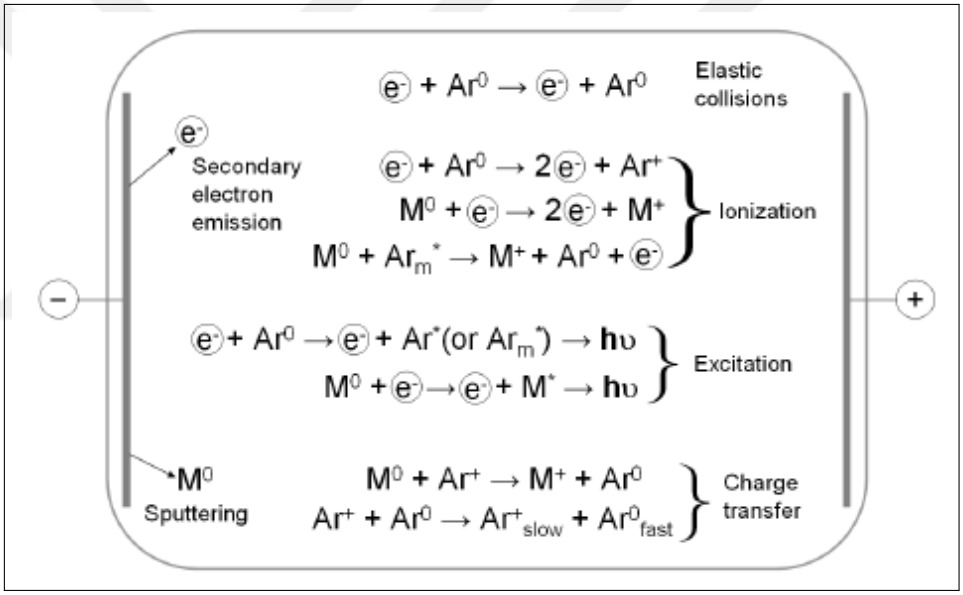


Figure 1.5. Basic processes occur in glow discharge plasma

1.5. SUSTAINMENT OF DISCHARGES

DC discharges: The cathode and anode electrodes are connected to a DC power supply through a ballast resistor. A zone of negative space charge (negative glow) is formed in front of the cathode during breakdown, shielding the external $\vec{E}$. The prerequisites for a plasma hold in the nearby, nearly field-free region (positive column). Small ambipolar fields in this area move the current needed to maintain the discharge. A plasma sheath develops close to the anode to balance the varying electron and ion mobilities. Operating currents for

this so-called glow discharge range from a few to a few hundred mAs. The seed electrons needed to maintain discharge functioning are continually supplied by ion-induced secondary electrons at the cathode. However, at smaller currents, the influence of secondary electrons is inadequate to maintain the discharge, necessitating volume ionization by background radiation. The so-called dark (Townsend or corona) discharge is seen during this regime. The electrodes may heat up at very high currents, which could result in thermionic emission of electrons. Due to the high efficiency of this method, ampere-range currents can be reached using just modest voltages. A supposedly heated arc develops.

RF discharges: By applying oscillating $\vec{E}$ at radio frequencies, plasmas can be produced. This has the significant benefit that displacement currents dominate the plasma and thus insulating electrodes can be utilized. There are two versions:

- Capacitive coupled plasma (CCP): In the system's electrical circuit, two electrodes combine to form a capacitor that confines the plasma volume. While the second electrode is often operated by an RF generator at normal voltages of several hundred volts, the first electrode is typically grounded. Typically, an LC-network-based matching device connects the RF-generator to the electrode.

- Inductively coupled plasma (ICP): An alternating $\vec{B}$ is used to induct the $\vec{E}$s into the plasma. The RF generator is coupled to a coil in this instance, and the alternating $\vec{B}$ creates an oscillating $\vec{E}$ within the plasma volume that ultimately generates an RF plasma current. A transformer's secondary coil is the plasma.

2. THIN FILM TECHNOLOGY: DEPOSITION TECHNIQUES AND PROCESSES

The processes PVD and CVD are used to deposit an extremely thin layer of material, defined as thin films [7], onto substrates. They are mostly utilized in the manufacturing of semiconductors, where the required connections are created by very thin layers of n- and p-type materials. The primary distinction between PVD and CVD is the kind of procedures each uses. While CVD involves chemical processes, PVD merely uses physical forces to deposit the layer. PVD uses evaporation to gasify a pure source material. The required thin film layer is then produced by the condensation of evaporating material onto the substrate material. The entire process does not involve any chemical reactions. This class includes sputtering and evaporation.

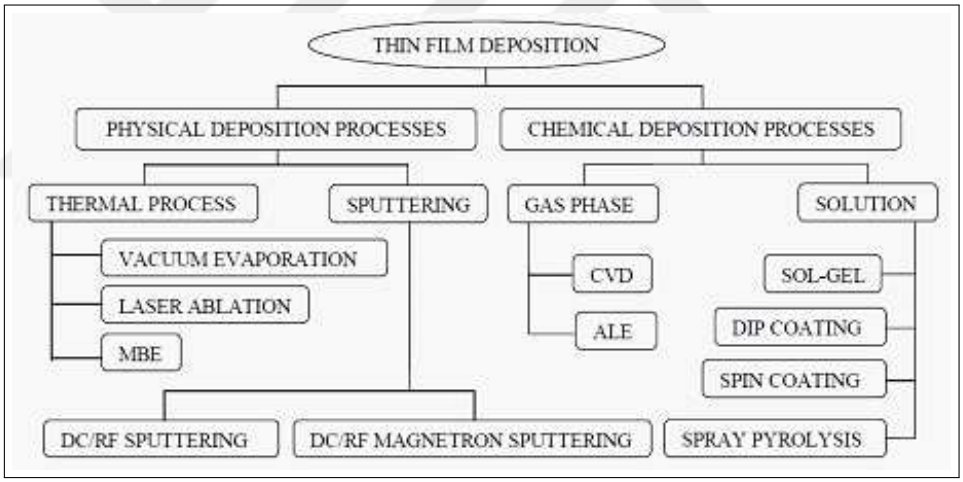


Figure 2.1. Thin film growth techniques

Spray pyrolysis, sol-gel, and pulsed laser ablation are a few more deposition methods for growing thin layers. The choice of deposition techniques is influenced by a number of variables, including the consistency and quality of the films, the expense and complexity of the equipment, and the unique drawbacks of each process. Electron beam evaporation and DC or RF magnetron sputtering are two methods applied in industry. Among these, magnetron sputtering yields high deposition rates and excellent film quality.

2.1. THIN FILM GROWTH

2.1.1. Film Structure

Temperature of substrate and plasma parameters are very important in thin film deposition and different models are utilized for quality coating. Condensation of atoms on surfaces place in three steps:

1. Atoms hit he surface, and their kinetic energy is transferred to the surface, then they attach to the surface.

2. Atoms on the surface move along the surface until they find positions of lower energy or till they are desorbed and leave the surface.

3. Condensed atoms diffuse inside solid state (volume diffusion).

Films are mainly produced in three different structures as a function of substrate temperature T_s and melting temperature T_m.

1. $T_s/T_m < 0.25$ for metals, and $T_s/T_m < 0.30$ for molecules: Adatoms are less mobile and the surface roughness cause big problems for adatoms to move around. Small crystallites grow like grass with very porous structure and with many voids.

2. $0.25(0,30) < T_s/T_m < 0.45$: Higher mobility case. Some voids are closed, grass structure remains. Density rises, lateral sizes increases, surface roughness is low.

3. $T_s/T_m > 0.45$: Volume diffusion increases and films recrystallizes. Larger crystallites are formed and relatively smooth surface is obtained.

This simple model developed by Movchan and Demchishin [8] is valid for most materials and it shows the limitation of evaporation. It must be noted that Zone 3 cannot be reached by many materials (See Fig. 2.2).

J. A. Thornton [9] developed a model for sputtering which includes more effects:

- The particles cary more energy (from $0.1 - 0.2\,eV$ to $4 - 40\,eV$)

- Collisions with gas result in different impact angles
- Significant interaction of surface and plasma is observed
- Increased bias voltage changes film growing.

These effects influence mainly the film at low temperature. The transition zone T is characterized by fibre-like dense structures with smooth surface. To correctly position zone T the interactions between deposited particles and plasma have to be taken into account:

- Atoms lose energy due to collisions.
- Mobility drops with increasing pressure.
- Zone boundaries shift to higher T_s/T_m ratios.

Bias voltage at the substrate shows the opposite effect. Ions are accelerated towards substrate and increase surface energy. Mobility is enhanced. Zone boundary shifts to smaller T_s/T_m values with higher bias voltage. Structure Zone Model (SZM) is used when the film thickness is greater $100\,nm$ [10].

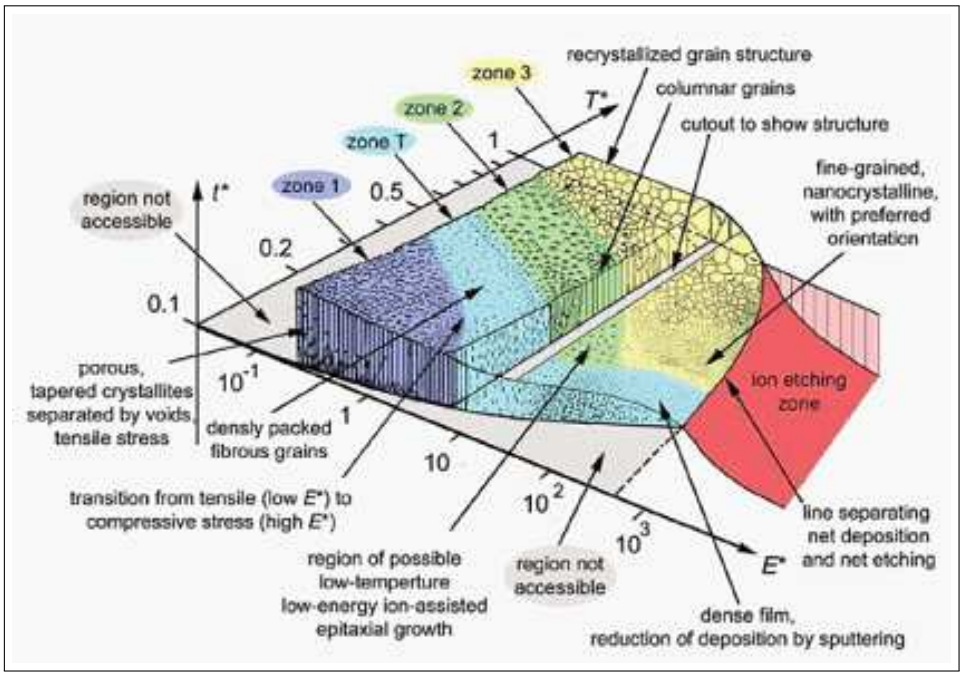


Figure 2.2. Structure zone model developed by Movchan, and extended by Thornton and Anders [10]

The film growth is governed by thermodynamics and kinetics. There are three principal

modes (See Fig. 2.3) of film growth as follows:

- **Layer by layer (2D), or Frank-van der Merve (FvdM), growth mode** corresponds to the situation where the bond between the film's atoms and the substrate is stronger than the bond between them. As a result, purely two-dimensional growth occurs, with each layer being finished before the next layer begins to grow.

- **Island (3D), or Vollmer-Weber (VW), growth mode** represents the case where the bond between film atoms and one another is stronger than the bond between them and the substrate. In this instance, 3D islands begin to form and expand right on the substrate's surface.

- **Layer plus island, or Stranski-Krastanov (SK), growth mode** refers to the intermediate situation between FvdM and VW growth. A fully formed 2D layer is followed by the development of 3D islands. The nature and thickness of the intermediate layer (i.e. the SK layer) rely on the specific case [11,12,13].

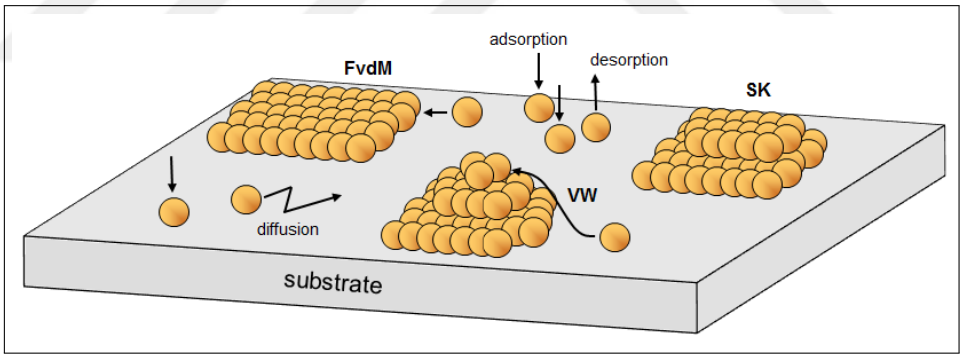


Figure 2.3. Thin film growth modes

Shigesato et al [14] demonstrated that the early stages of Tin-doped Indium Oxide (ITO) thin film growth is in Vollmer-Weber mode. Similarly, growth of metal films begin with islands formation [11].

2.2. INTERACTIONS OF IONS WITH SURFACES

Consider that an ion hits the surface of a solid target. In this case, possible scenarios are as follows: [17]:

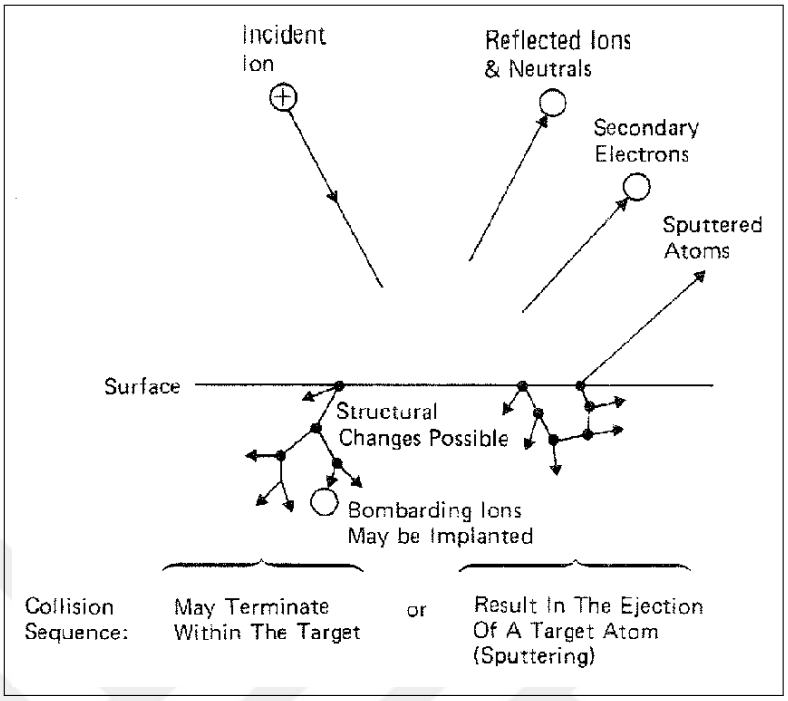


Figure 2.4. Interactions of ions with surfaces

- Reflection: It might be reflected, or probably neutralized in the process.
- Emission: Due to the impact of the ion, the target atoms to eject electrons called as a secondary electron emission.
- Implantation: It might get buried inside the target, which is the phenomenon of ion implantation.
- Defects: Its impact might give rise to some structural defects such as vacancy of atoms and interstitials in the target.
- Sputtering: The ion impact may causes collision cascade among atoms of the target, and possibly resulting in the ejection of some of these atoms. This process is called as sputtering.

2.3. SPUTTERING TECHNOLOGY

2.3.1. The Mechanism of Sputtering

The interaction of the incident ion and the target atoms, as well as the following interactions among the latter, can be thought of as a sequence of binary collisions in the energy range most pertinent to sputter deposition. An ion or a neutral atom could have been the incident particle. Ions are typically utilized because an electric field can accelerate them without much difficulty, but neutrals are problematic in this regard. The impacting species are actually essentially neutral.

A collision cascade is a succession of collisions that occur in the target as a result of the first collision at the surface. It will mostly depend on luck whether this cascade causes an atom to be sputter-ejected from the target's surface or if it diverts into the target's interior, slowly converting the energy of the first hit into lattice vibrations, or heat. Therefore, it should come as no surprise that sputter ejection is not very effective, with only around 1% of the incident energy typically returning as the energy of the sputtered atoms.

Fortunately, the contacts in a sputtering target are sufficiently close together that we only need to take into account interactions between near neighbors. A binary collision is characterized by the energy transfer function

$$\frac{4m_i m_t}{(m_i + m_t)^2}$$

where m_i and m_t are the masses of the colliding atoms. A chain of such collisions leads to the sputtering.

The proportion of the density of target atoms (molecules) ejected to impinging ion gives the sputtering yield S. In other words, S gives efficiency

$$S = \frac{\text{number of released atoms}}{\text{number of impacting ions}}.$$

We would expect S to depend on the m_i and m_t respectively, and on the energy E of the impinging ion. The energy transfer process from the impinging ion to the sputtered atoms should be viewed as sputtering generally, and S would be proportional to the energy stored

in a thin layer close to the surface. Hence,

$$S = \frac{3\alpha}{4\pi^2} \frac{4m_i m_t}{(m_i + m_t)^2} \frac{E}{U_0}$$

where U_0 is the surface binding energy of the sputtered material, and α is a monotonic increasing function of m_t/m_i.

If an ion impacts on a substrate about $10\,nm$ are influenced. About 1000 atoms are participating, decay time is approximately $10^{-11}\,s$. Most of the energy causes oscillations, heats up the target. Target means cathode material to be disintegrated. Kinetic energy is about $2 - 10\,eV$. All kinds of materials can be sputtered.

2.3.2. Sputtering as a Deposition Process

The majority of the material used in sputter deposition arrives the substrate in atomic or molecular form. The atom moves around the substrate in a manner that is controlled by its binding energy to it and is impacted by both the substrate's nature and temperature. Energy-wise, the substrate's surface resembles an egg carton, with each depression acting as a temporary resting place or adsorption site for the atoms that are depositing and diffusing. The atom will either hop out of the egg carton or over the barrier and into an adjacent site at each hop, re-evaporating in the process.

The probability of creating the atomic pair will be dependent on the deposition rate. Later, the doublets will be united by other single atoms to form triplets, quadruplets and so on. This is called as the nucleation stage of thin film formation, giving rise to the formation of semi-stable islands. Next stage is the island growth stage. Throughout this phase, the size of the islands grow. At the end, they grow sufficiently large to unite; which is called as the coalescence or agglomeration stage. TEM observations demonstrates that the islands frequently show liquid-like character during coalescence. Coalescence proceeds until the film reaches continuity (See Fig. 2.5). Sometimes the average film thickness may reach to several hundreds nanometers. Hence, the film features hills and valleys during the agglomeration stage.

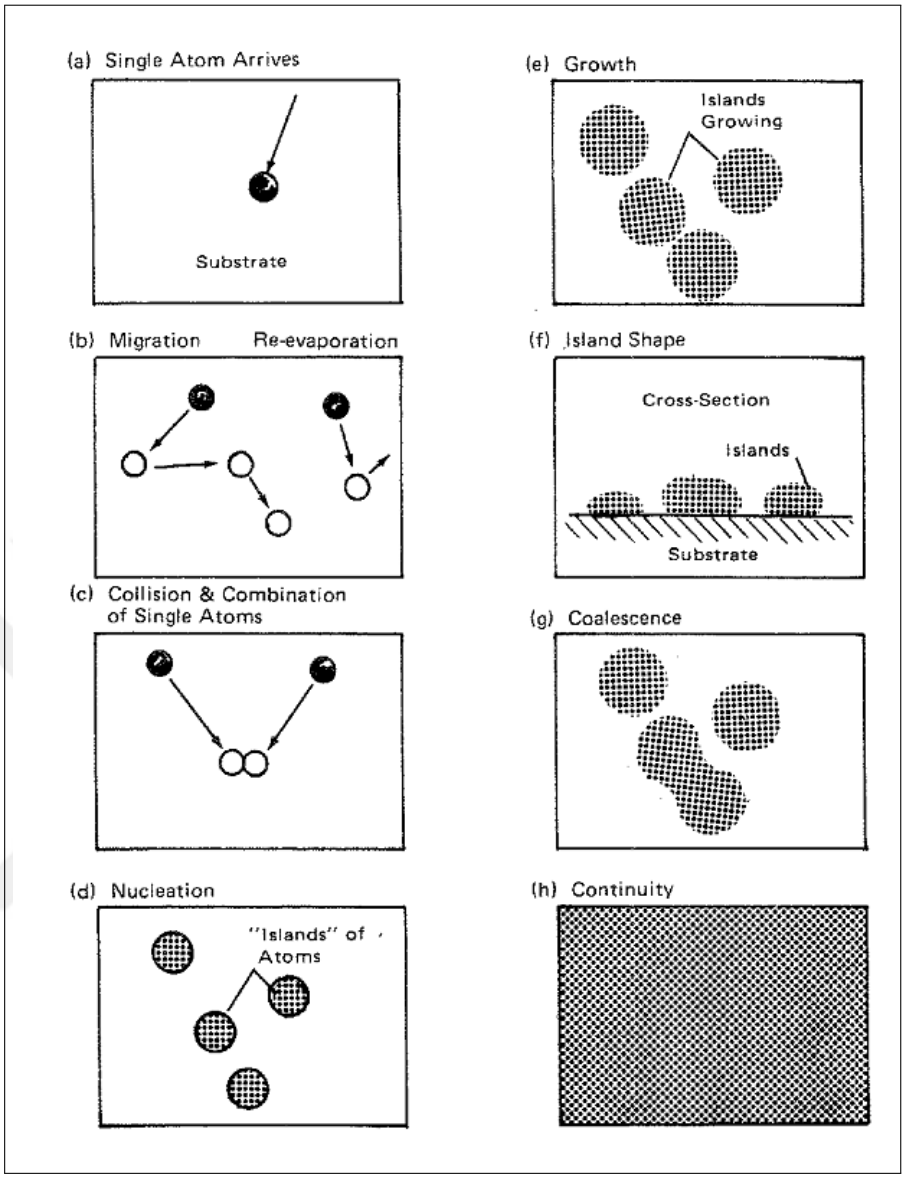


Figure 2.5. The phases of thin film formation

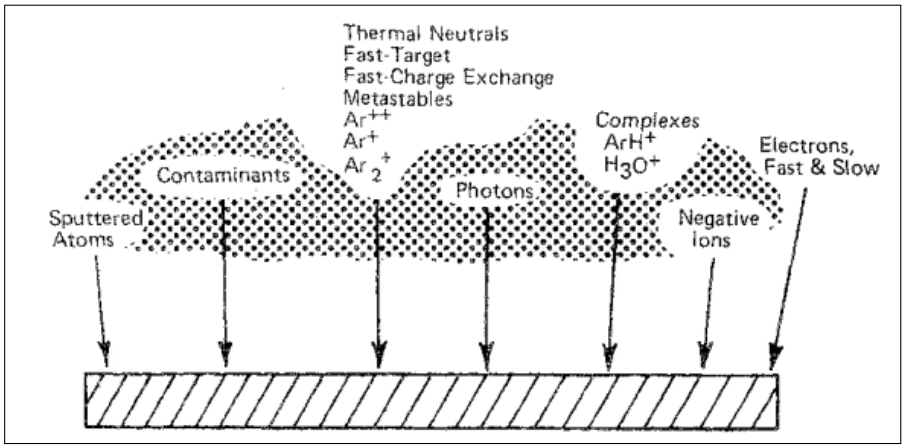


Figure 2.6. Particles bombarding the substrate in sputter deposition

Each island generally has either one crystal or a few crystals during the island stage. The orientation of each island will vary randomly on a polycrystalline substrate, resulting in a polycrystalline film. The substrate structure on a single crystal substrate may dictate the island orientations so that growth and coalescence gives rise to a single crystal film. This the phenomenon is called as epitaxy.

Mobile surface atoms have a greater probability of finding energetically favorable positions in the growing film. Increased substrate temperature enhances mobility. However, because it also takes time to find a low energy lattice position, low deposition rate, too, promotes the crystal growth.

Thin film structure is sensitively dependent on the growing conditions. In contrast to evaporation, the sputtering is extremely complex process having numerous variables. As depicted Figure 2.6, the substrate and film will be exposure to various kinds of bombardment during the film growth.

2.3.3. DC-Diode Sputtering

In DC sputtering, the cathode is connected to negative. Housing and substrates are connected to positive. In this configuration only conductive material such as metals can be sputtered.

2.3.4. RF Sputtering

For RF sputtering, three arrangements are possible:

1. Excitation by a coil outside generates plasma and DC voltage is applied to the electrode.
2. Two targets of same material are used. RF voltage is applied between them, both are eroded.
3. One electrode is coupled with a capacitor to the RF source. Due to the higher mobility of the electrons the cathode is negatively charged, attracts positive ions and is eroded.

Not only metals and semiconductors but also isolators can be sputtered using RF arrangements. However, the sputter rates are lower than for conductors. Sputtering rate rises with RF power.

2.3.5. Bias Sputtering

Substrates are not always connected to ground. Sometimes they are set to negative voltage in order to obtain a constant bombardment of ions on the growing films. Gas and defects are driven out. Bias voltage should not exceed $150\,eV$ because there are many ions are deeply impacted.

2.3.6. Reactive Sputtering

Not all atoms come from the target. At least one component comes from the sputtering gas. For example, the sputtering of Ti using Ar/O_2 mixture gives TiO_2 or if Al is sputtered in an Ar/O_2 mixture, Al_2O_3 is deposited.

Simple metallic targets can be used which give high sputter rates. Sometimes the chemical reaction takes place at the target and thin isolating films are growing at the surface, which drops down the sputter rate.

Many hard films such as carbides, nitrides or oxides to reduce wear, corrosion or for decoration

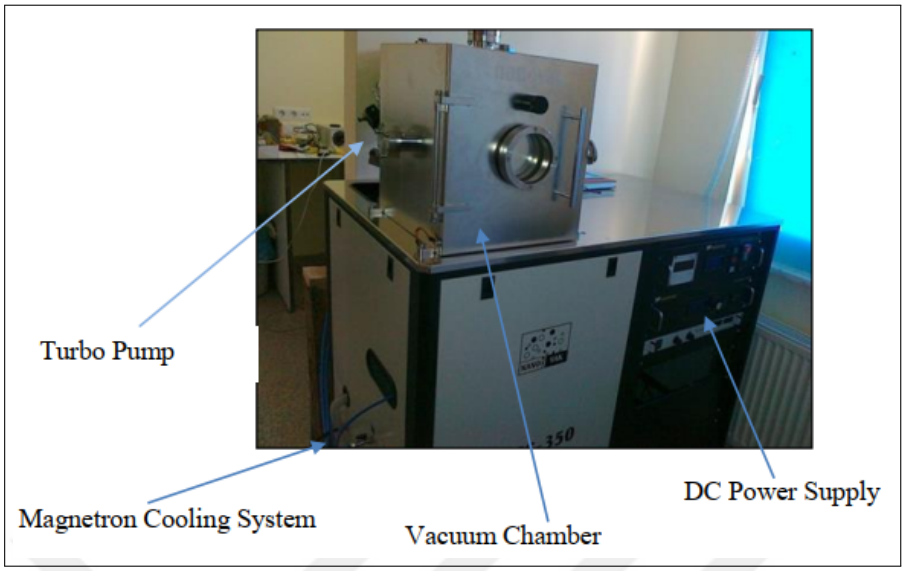


Figure 2.7. NANOVAK NVSS350 Magnetron Sputtering System

(TiN-gold, CiN-silver) can be obtained by reactive sputtering.

2.3.7. Magnetron Sputtering

Industrial applications like mass production use magnetron sputtering. Figure 2.7 and Figure 2.11 are two examples of commercially available magnetron sputtering systems which were used in this study. Magnets are applied behind the target as shown in Figure 2.8 and Figure 2.9. The superposition of $\vec{E}$ and $\vec{B}$ forces the electrons to move on spherical or spiral orbits (See Figure 2.10). The pathways of electrons significantly extended and hence many more ions are generated directly before the target, so erosion rises and gives much higher sputter yield. Changing geometry causes changes in sputtering characteristics. Multi-magnetron systems like Figure 2.12 are widely used.

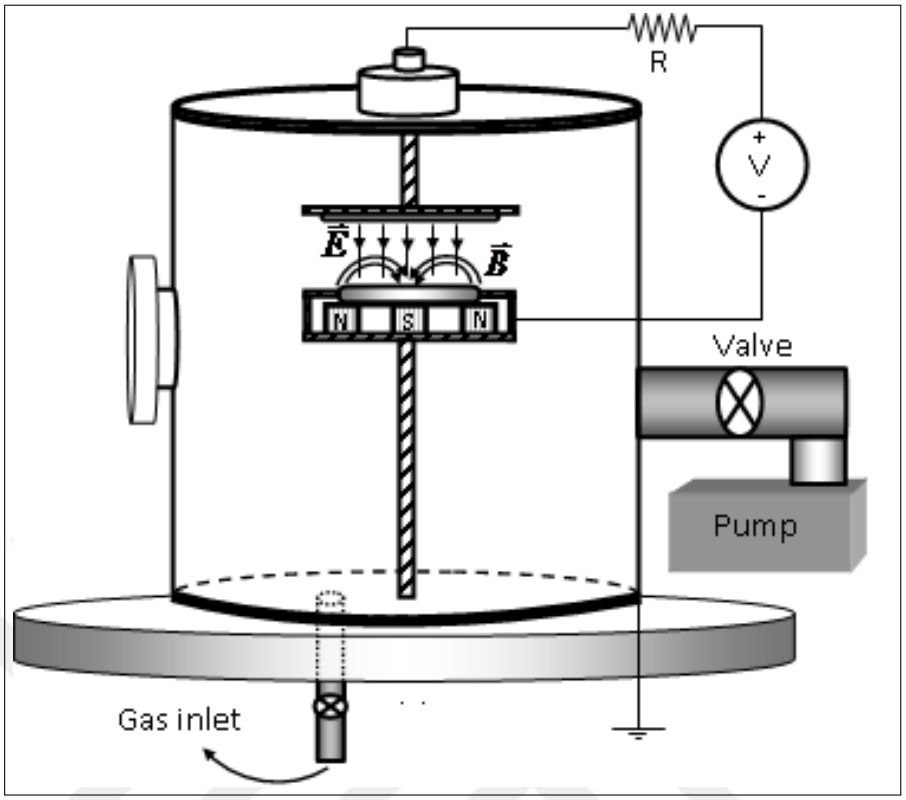


Figure 2.8. Schematic of NANOVAK Magnetron Sputtering System

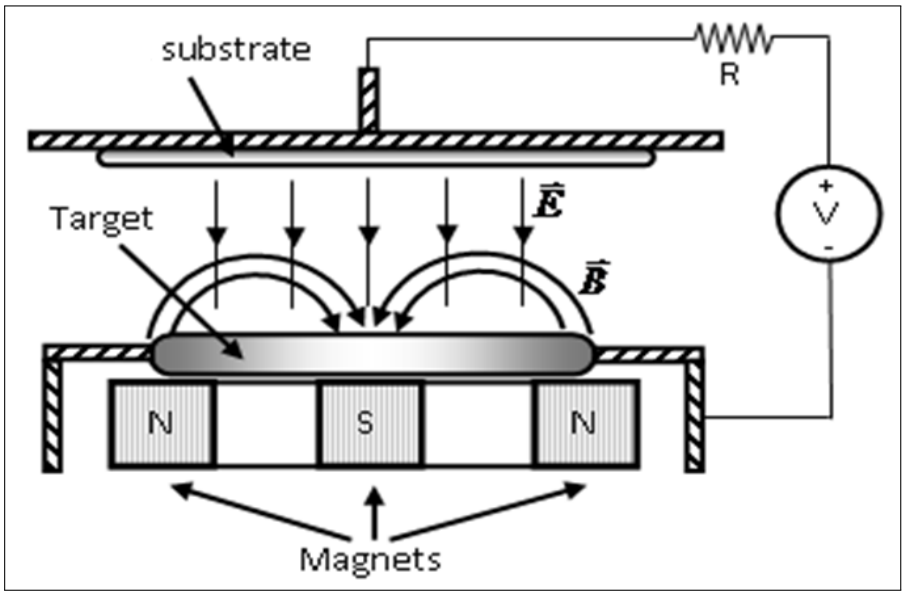


Figure 2.9. Side view of NANOVAK Magnetron Sputtering System

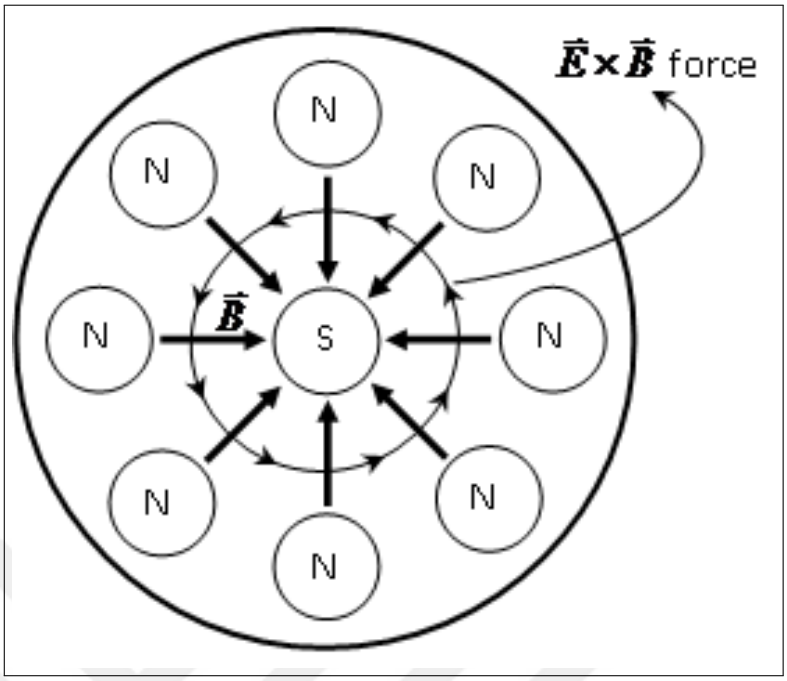


Figure 2.10. Top view of NANOVAK Magnetron Sputtering System

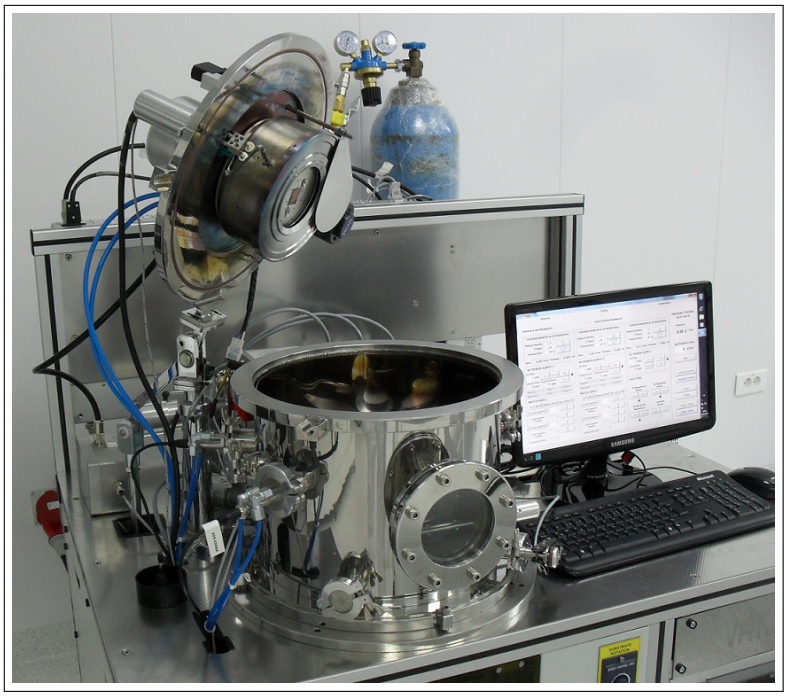


Figure 2.11. VAKSIS PVD Handy 3M Magnetron Sputtering System

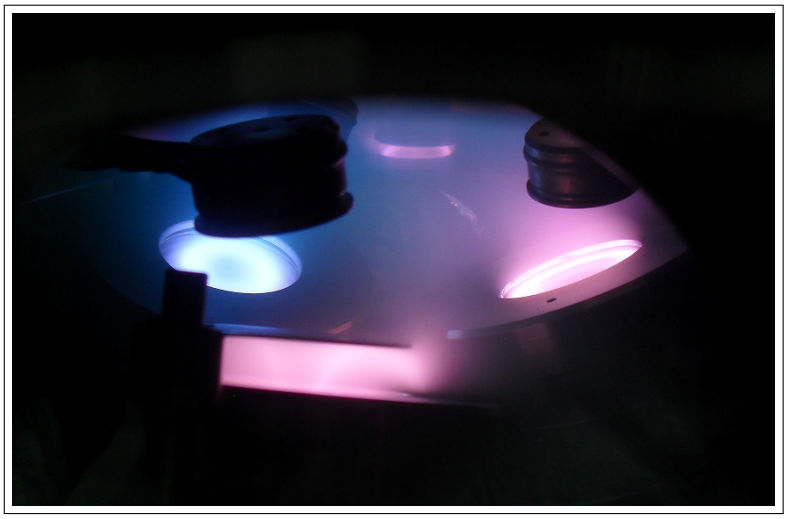


Figure 2.12. VAKSIS Dual DC and RF Magnetrons

3. CHARACTERIZATION TOOLS AND METHODS

3.1. DETERMINATION OF FILM THICKNESS

Film thickness is vitally important because it influences thin film properties. The measurement of film thickness can be divided into two groups such that

1. Mechanical methods: Stylus Profilometry, Weight Measurement, Crystal Oscillators, etc.

2. Optical methods: Interferometry, Step Gauges, Ellipsometry, etc.

We will mention about stylus profilometry, quartz crystal microbalances and ellipsometry methods which were used to obtain the film thickness of our samples.

3.1.1. Stylus-Method Profilometry

The stylus profilometry is based on tracking the mechanical motion. It is designed to sketch the topography of a film-substrate as shown in Figure 3.1. A diamond needle having a tip diameter of $210\,mm$ is used for the electromagnetic pickup. The force can be tuning uo from 1 to $30\,mg$, and vertical magnifications of 10^4 up to 10^6 are achievable. The height of the corresponding step-contour trace gives the film thickness. There are a few factors restricts to take accurate measurements:

1. Scratching and stylus penetration of films. This can occasionally be an issue with very soft films such as In, and Sn.

2. Roughness of the substrate. As a result, there is confusion about where the step is since there is too much noise introduced into the measurement.

3. Vibrating apparatus. the equipment. To reduce background vibrations, robust supports and proper shock mounting are crucial.

Figure 3.2 and Figure 3.3 are two commercial surface profilometers which were used in this study. The leveling and measurement processes in contemporary devices are

computer-controlled. In order to magnify areas of interest and produce the best profile fits, the vertical stylus movement is digitalized.

For the purpose of standardizing measurements, calibration profiles are made available. The vertical resolution is $1\,nm$, and the measuring range is $20 - 65\,mm$.

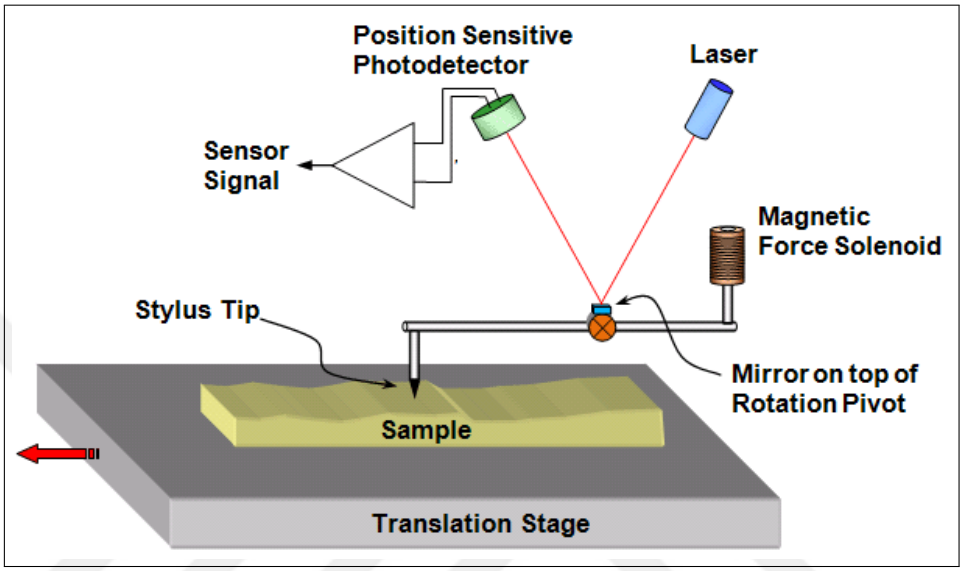


Figure 3.1. Schematics of stylus profilometer

3.1.2. Quartz Crystal Microbalances

The quartz crystal microbalance (QCM) method is employed for measuring the film thickness during deposition. It makes use of a quartz crystal oscillator and can measure the film's mass. The thickness can be calculated from the density of film.

Consider homogeneous, vibrating elastic plates whose elastic moduli, density, and dimensions affect their resonance frequencies. The resonant frequency is altered by the increase in mass brought on by the thin film deposition. Typically, metal film electrodes are placed atop AT quartz crystals that are placed inside the chamber near the substrate. The fundamental frequency f is given by

$$f = \frac{v_q}{2t_q}$$

where v_q is the velocity of elastic wave and t_q is thickness of the plate. (It is equal to half the wavelength of the transverse wave, too). The mass dm deposit on one of the crystal electrodes

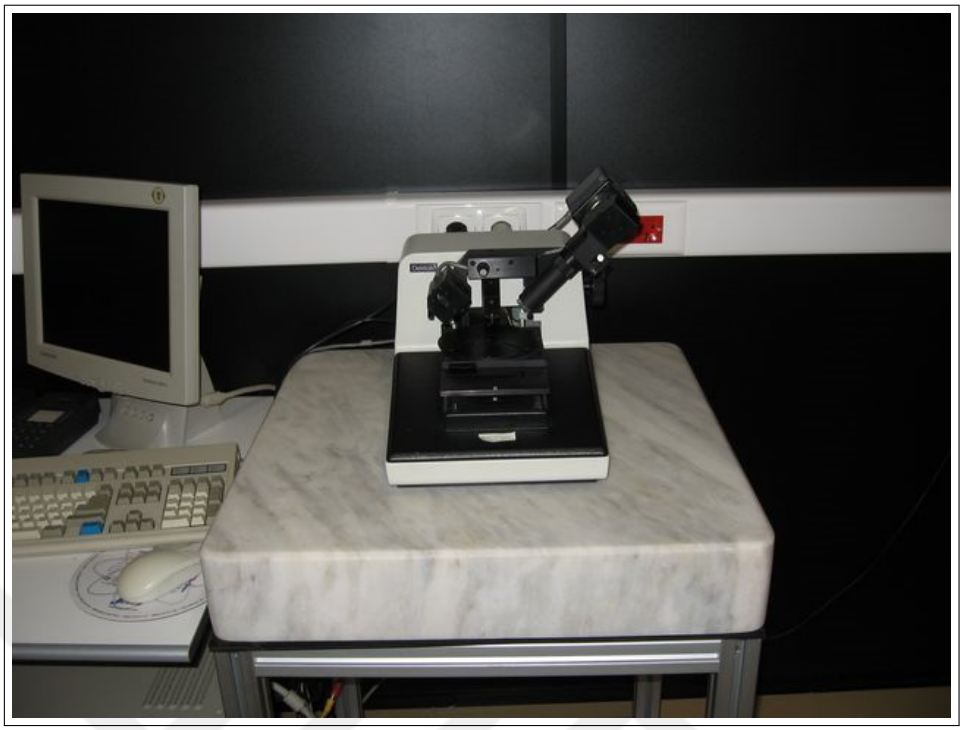


Figure 3.2. DEKTAK3 Surface Profilometer

leads to an increase in film/crystal thickness given by

$$dt = \frac{dm}{A\rho}$$

where A is the film area and ρ is the film density. One combine these two equations to obtain the change in frequency

$$df = -\frac{2f^2}{v_g\rho}\frac{dm}{A}$$

which is called Sauerbrey equation. From this equation mass change due to that frequency change can be calculated.

Quartz crystal oscillators are mostly used to measure rate of deposition rather than the thickness of film. Plasma can disturb the system and the frequency measurement value may be very different from what the profilometer reads.



Figure 3.3. NanoMap 500LS Scanning Contact Surface Profilometer

3.2. MEASUREMENT OF OPTICAL TRANSMITTANCE

3.2.1. Spectroscopic Ellipsometry

Ellipsometry is the most effective optical method for characterizing thin films. Rather than the intensity the change of polarization due to the interaction with the film structure is measured. Normally the light is elliptically polarized. Ellipsometry can be done in reflection or transmission. There are many different set-ups, here is the principle: A light beam with defined polarization hits the sample at a certain angle of incidence. The polarization changes and this change of polarization is measured. To do so, a polarizer is rotated in front of the detector.

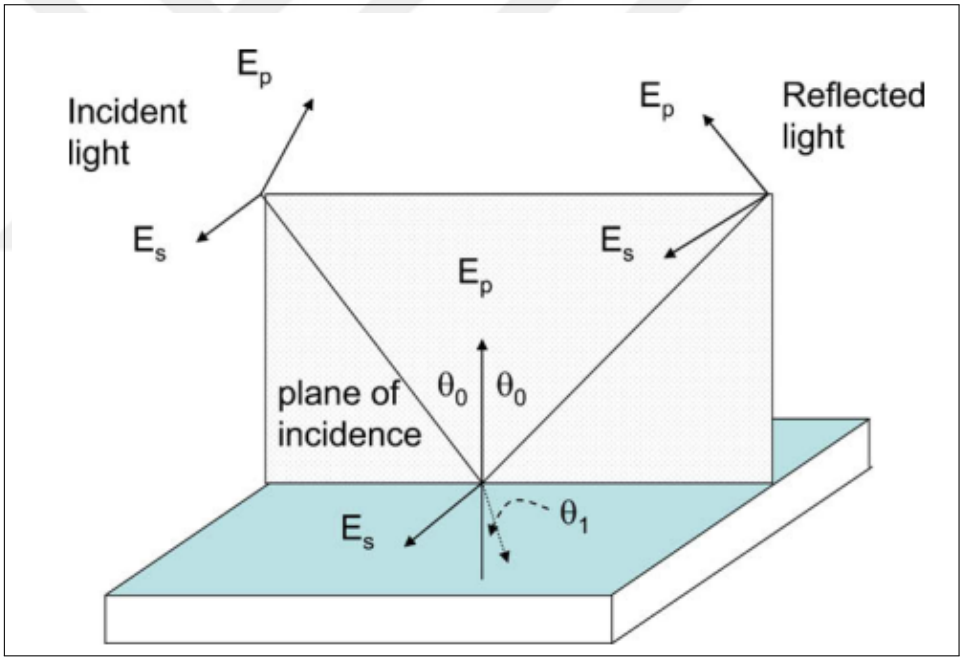


Figure 3.4. Ellipsometry technique

Figure 3.4 shows the theory of ellipsometry technique. Ellipsometry lives with the difference between *p*- and *s*-light in respect of amplitude and phase. Therefore the polarizer has to be adjusted in such a way that both *p*- and *s*-light hits the sample.

Let us suppose the reflection is measured and the electric fields of reflected *p*- and *s*-polarized



Figure 3.5. SENTECH SE850 Ellipsometry

light are

$$r_p = E_p \exp[i(\vec{k} \times \vec{r} - \omega t + \Delta_p)]$$
$$r_s = E_s \exp[i(\vec{k} \times \vec{r} - \omega t + \Delta_s)].$$

Dividing these two equations to get the fundamental formula of ellipsometry

$$\frac{r_p}{r_s} = \tan \Phi \exp(i\Delta)$$

where Φ is the quotient of the field amplitudes of p- and s-polarized light wave

$$\tan \Phi = \frac{E_p}{E_s},$$

and Δ is the phase shift between the p- and s-polarized light wave

$$\Delta = \Delta_p - \Delta_s$$

The ellipsometer measures Δ and Φ of each film structure.

A commercial ellipsometry device that used in this study is shown in Figure 3.5.

3.2.2. Photoluminescence Spectroscopy

The ultraviolet-near-infrared spectrophotometer (UV-NIR) is a device that can measure the absorption, transmittance or reflectance in the spectral region ($230 - 1400\,nm$). In this region of the electromagnetic spectrum, electronic transitions occurs in molecules, and therefore, the composition of the materials have a direct impact on absorption, reflection, and transmittance.

By using a monochromator to hold the excitation light at a fixed wavelength, different fluorescent light waves emitted from a sample can be detected. The opposite of this is true for the excitation spectrum. The excitation light is made multicoloured with the use of a monochromator, and the emission light is maintained at a fixed wavelength. By gathering all of the scattering wavelengths produced by various excitation wavelengths and combining them, the excitation map is measured. A data set in three dimensions is produced. Excitation and emission wavelength affect emission intensity. The contour map is typically depicted.

In Figure 3.6, a commercial spectrophotometer is shown, which was used in this study.

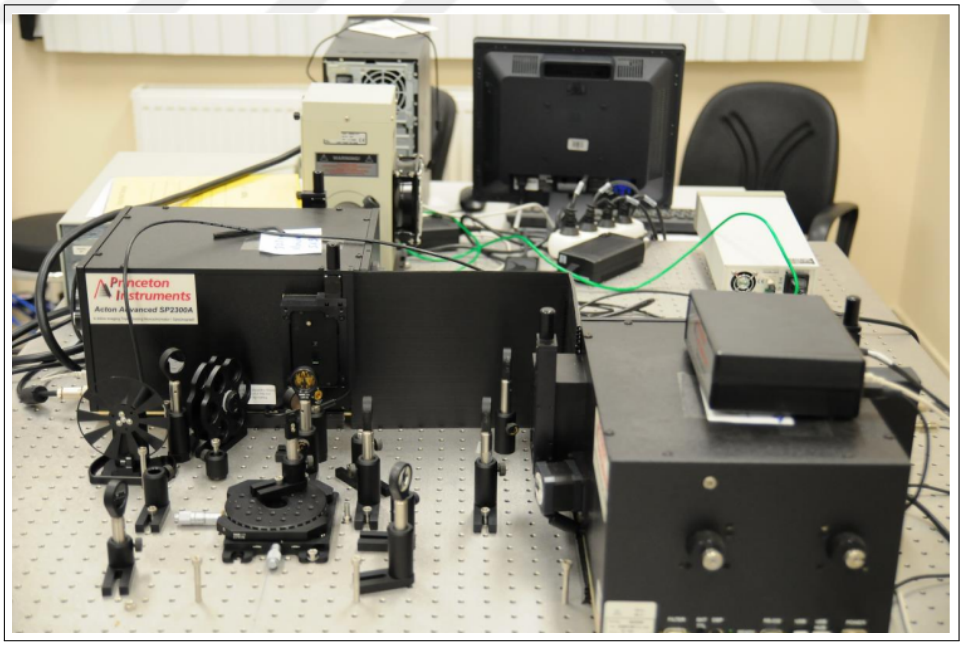


Figure 3.6. Acton SP2300A Spectrometer

3.3. MEASUREMENT OF SHEET RESISTANCE

If electrical current is applied by a tip into a thin homogeneous film of infinite area, the current is homogeneously distributed over the area.

Isoclinical lines which combines points of constant current are concentric circles around the tip. If I_0 is the applied current, then it is homogeneously distributed along the circumference of the circle of radius r

$$I(r) = \frac{I_0}{2\pi r} .$$

Therefore the voltage between two points with radii r_1 and r_2 is given by

$$\Delta U = \int_{r_1}^{r_2} \frac{\rho}{t} \frac{I_0}{2\pi r} \, dr = \frac{\rho}{t} \frac{I_0}{2\pi} \, \ell n \frac{r_2}{r_1} .$$

The measurement of the sheet resistance $\frac{\rho}{t}$ is usually done by means of a four point probe. Two arrangements of the four tips are in use: Linear arrangement (Figure 3.7) and square arrangement (Figure 3.8).

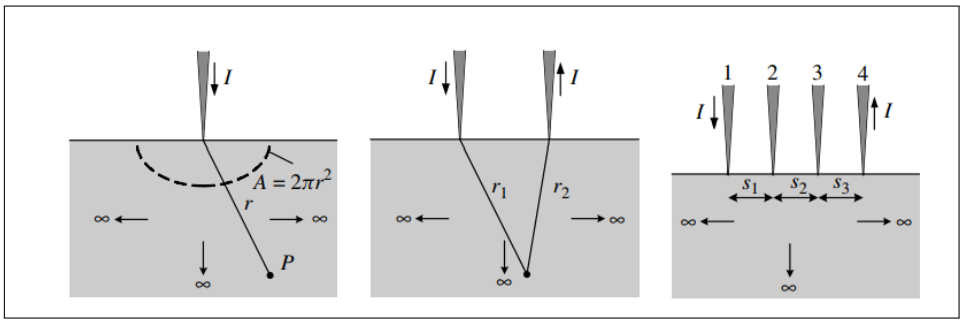


Figure 3.7. Linear arrangement of one, two and four point probe

The current is applied from a constant current source through P_1 and P_4. The voltage between P_2 and P_3 is measured. Due to I_1 the current applied to P_1 the voltage between P_2 and P_3 is given by

$$\Delta U_1 = \frac{\rho}{t} \frac{I_1}{2\pi} \, \ell n \frac{s_1 + s_2}{s_1} .$$

Due to I_4 the current applied to P_4 the voltage between P_2 and P_3 is given by

$$\Delta U_4 = \frac{\rho}{t} \frac{I_1}{2\pi} \, \ell n \frac{s_3}{s_2 + s_3} .$$

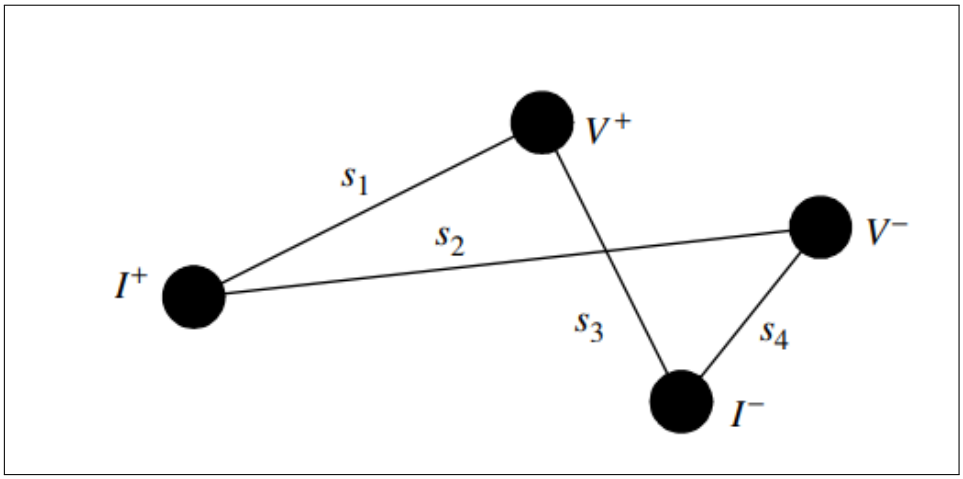


Figure 3.8. Square arrangement of four point probe

Since $I_1 = -I_4 = I$ the total voltage is

$$\Delta U = \Delta U_1 + \Delta U_4 = \frac{\rho}{t}\frac{I_1}{2\pi}\left(\ell n\frac{s_1 + s_2}{s_1} - \ell n\frac{s_3}{s_2 + s_3}\right).$$

In normal arrangements the tips are evenly spaced:

$$s_1 = s_2 = s_3 = s$$

therefore

$$\Delta U = \frac{\rho}{t}\frac{I}{\pi}\,\ell n2$$

and

$$\frac{\rho}{t} = \frac{\pi}{\ell n2}\frac{\Delta U}{I}$$

or

$$\frac{\rho}{t} \cong 4,532\,\frac{\Delta U}{I} \tag{3.1}$$

is found. In literature, instead of $\frac{\rho}{t}$, R_s or $R_\blacksquare$ are used for sheet resistance and its unit is ohms per square.

The current is applied from a constant current source through P_1 and P_2. The voltage is

measured between P_3 and P_4

$$\Delta U = \frac{\rho}{t}\frac{I}{2\pi}\left(\ell n\frac{\sqrt{s_2^2+s_4^2}}{s_2}+\ell n\frac{\sqrt{s_3^2+s_4^2}}{s_3}\right).$$

In a square arrangement all distances are equal:

$$s_1 = s_2 = s_3 = s_4 = s\,.$$

so

$$\Delta U = \frac{\rho}{t}\frac{I}{\pi}\ell n\sqrt{2}$$

and

$$\frac{\rho}{t} = \frac{\pi}{\ell n\sqrt{2}}\frac{\Delta U}{I}$$

or

$$\frac{\rho}{t} \cong 9,06\,\frac{\Delta U}{I} \tag{3.2}$$

is obtained. The formulas 3.1 and 3.2 are valid when the probes are sufficiently far from the other surfaces of the sample [20,21]. The linear arrangement is the most common four-point probe configuration. The square arrangement is widely used as contacts to square semiconductor samples [22].

The dimensions of our slides is enough to use formula (3.1), i.e. $d/s >> 1$ and $t/s << 1$.



(a) (b)

Figure 3.9. Sheet resistance measurement system consist of (a) semiconductor parameter analyzer and (b) four point probe head

In this study, Agilent-HP-4155A Semiconductor Parameter Analyzer and 4-point pobe head by Jandel, which are shown in Figure 3.9, were used to measure the sheet resistance.

3.4. SURFACE MORPHOLOGY

3.4.1. Scanning Electron Microscopy

By capturing secondary or backscattered electrons produced by the specimen with a high energy electron beam, a scanning electron microscope (SEM) monitors the surface topography and structure of the specimen. The resulting images provide great amount information regarding sample features owing to their high resolution and degree of magnification compared to a light microscope. When an electron hits the surface, backscattered electrons, excited lower energy ($< 50\,eV$) secondary electrons, Auger electrons and characteristic X-rays are created as shown in the Figure 3.10. Each of these electrons and photons can be employed to provide information about sample by helping of different types of detectors [18].

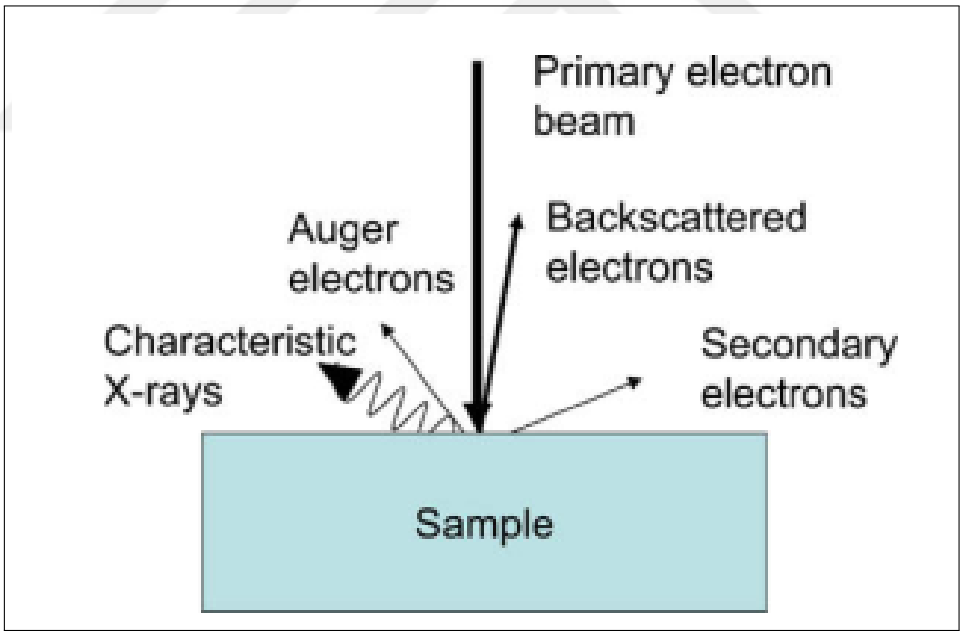


Figure 3.10. The resulting electrons and photons after the electron beam interacts with the sample

SEM works in a vacuum environment and needs conductive surface. These are two main disadvantages of it. It consists of an electron gun, condenser lens, deflection coils, objective lens, detectors and a computer (Figure 3.11).

The electron beam collected by the condenser lens is focused by the objective lens and the

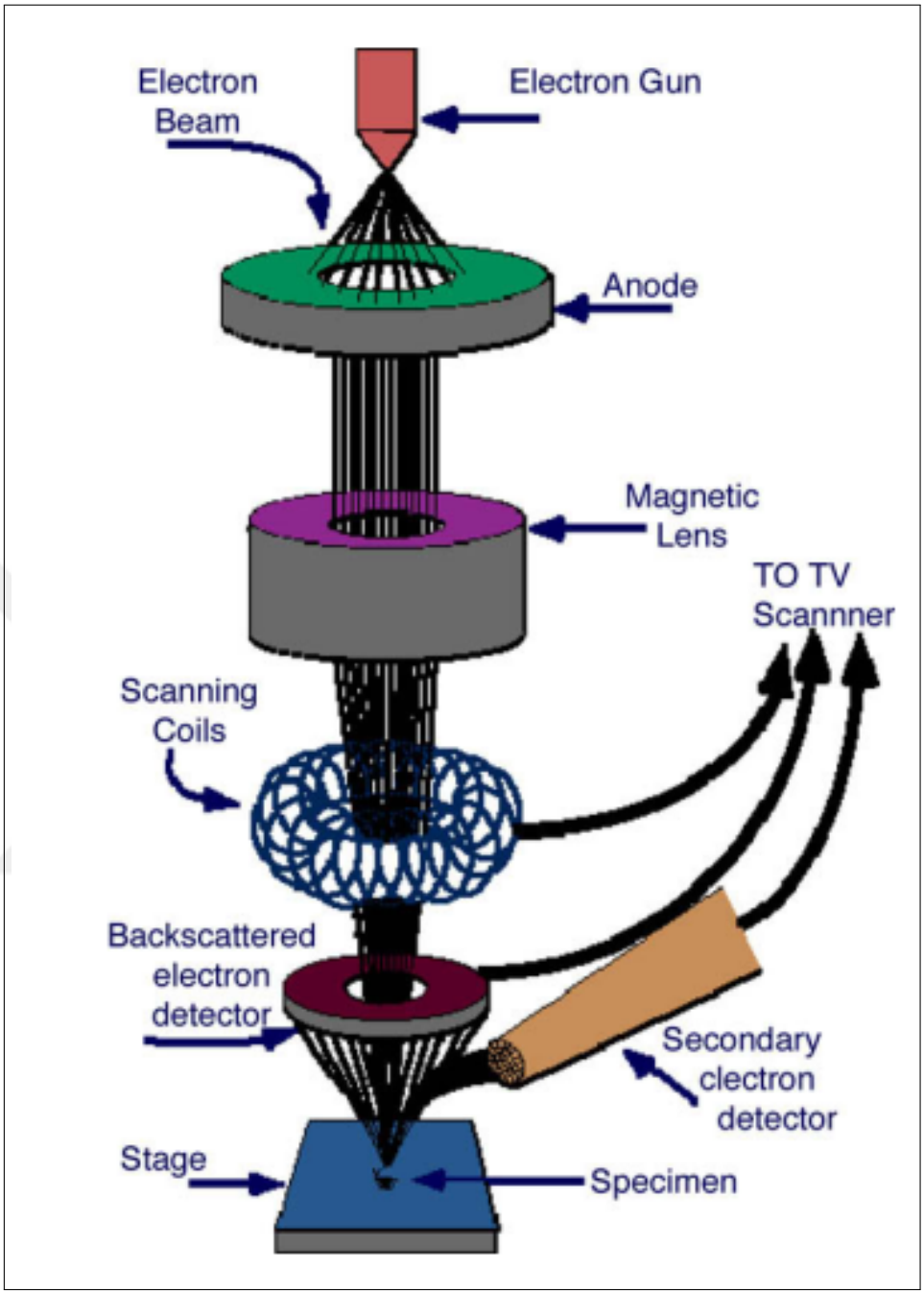


Figure 3.11. Schematic view of SEM components

scanning process is made by the electromagnetic dispersive coils. Elastically backscattered electrons with energies that are roughly equal to the incident electrons, secondary electrons whose energies are lower than $50\,eV$ and X-rays are gathered by the detectors inside the chamber. Owing to this electron and sample interaction, a signal is created, and this signal is sent to the computer to obtain image. The morphology of the sample is shown by secondary electron imaging, the contrasts in the composition of the specimen are highlighted by backscattered electron imaging, and the elemental composition of the material is identified by the help of characteristic X-rays. Moreover, SEM can be utilized for measuring the film thickness. Such an SEM image taken from our coating is presented in Figure 3.12.

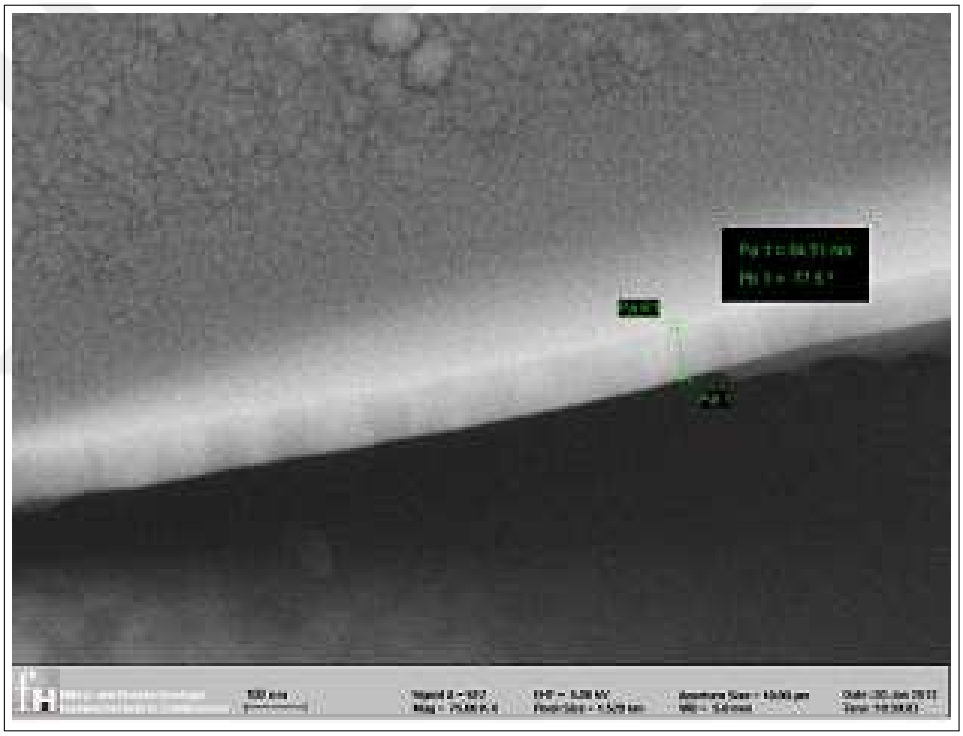


Figure 3.12. Thickness of thin films can be determined by using SEM

3.4.2. Energy Dispersive X-Ray Spectroscopy

Energy Dispersive X-Ray Spectroscopy (EDX) is a method implemented to examine the material's elemental and chemical composition. A beam of high energy particles are sent onto the material surface and X-rays are emitted. When an electron strikes the surface, an electron in an inner shell is ejected by excitation, and an electron hole is created. If a higher energy level electron fills this hole, a characteristic X-ray may be radiated because of the

energy difference between the higher and lower energy levels. The energy of the X-rays radiated from the sample is measured by the spectrometer. This provides information about the structural and elemental properties of the specimen.

EDX systems are usually worked together with SEMs where the electron beam is used for excitation of characteristics X-rays from the sample. An significant variation known as X-ray wavelength dispersive analysis (WDX) increases X-ray linewidth resolution by dispersing wavelength rather than energy [23].

3.4.3. Atomic Force Microscopy

Atomic force microscopy (AFM) is a technique that surface topography can be monitored from $Angstrom$ to $100\,micron$. By scanning the surface with highly sensitive cantilever it can measure atomic forces, i.e. nN. Unlike STM, the sample does not have to be conductive. Therefore, all type of material surfaces such as metals, insulators and biological substances can be easily investigated.

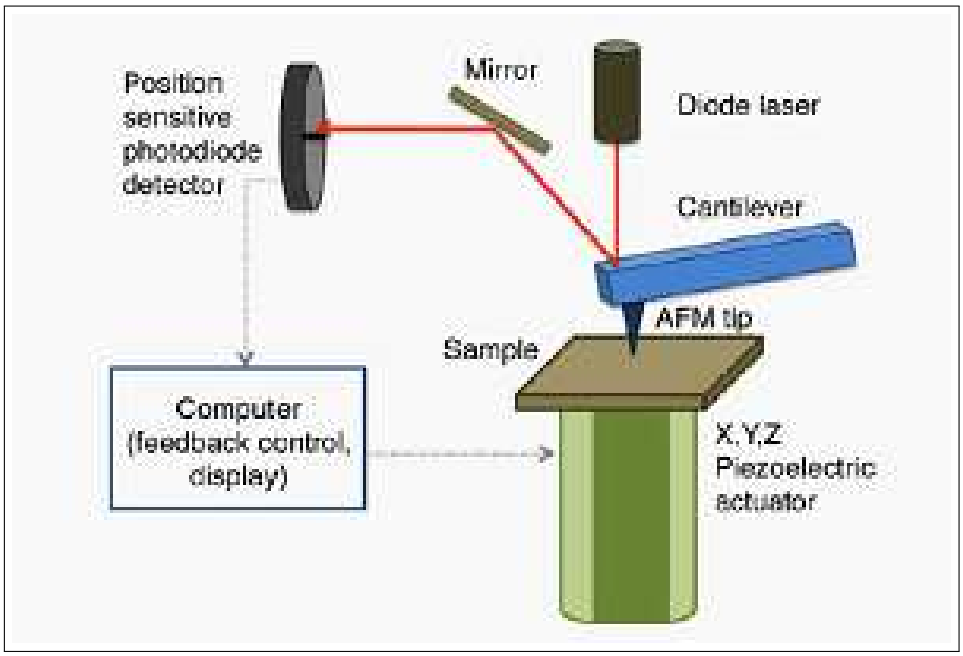


Figure 3.13. Schematic view of AFM components

AFM consists of a piezoelectric actuator, a tip (prob), a cantilever, a diode laser, a photodiode detector, and a computer as shown in Figure 3.13. The piezoelectric actuator serves as a

mounting for the tip. The tip is bonded to the cantilever having a spring constant changes from 0.001 to $100\,N/m$. When the tip is move over the sample surface, due to the forces between the tip and the sample the cantilever is deflected according to Hooke' law

$$F = kx$$

where F is the force exerted on the cantilever, k is the spring constant of the cantilever, and x is the distance of deflection. The position sensitive photodiode detector measures the angular deflection of the cantilever and this gives information about surface morphology. The spring constant of the cantilever is

$$k = \frac{Ywt^3}{4L^3}$$

where Y is the Young modulus of the cantilever material, w, t, L are the width, thickness and length of the cantilever, respectively. The cantilever's resonance frequency can be calculated from

$$f_0 = 0.162\,\frac{t}{L^2}\sqrt{\frac{Y}{\rho}}$$

where ρ is the mass density of the cantilever.

AFM measurements can be performed in three modes:

1. **Contact (Static) Mode**: In firstly developed method, the tip make a small physical contact with the surface of the sample, where the repulsive force is instrumental. In this mode, a soft tip having a lower spring constant is employed. The force between the tip and the sample is measured when the tip is nearly contact with and track over the surface. The tip height (z) is adjustable so that this force remains unchanged.

2. **Non-contact Mode**: In this mode, a stiffer tip having a high k value is employed; the tip is forcibly to oscillate above the sample at a frequency that is close to its natural resonance frequency. The resonance frequency of the tip is decreased by the long range Van der Waals forces, which are strongest in the range of $1 - 10\,nm$ from the surface. The tip is moved while maintaining the same deflection and the change in height is measured. Alternatively, the tip is held at the same distance and the change in deflection is measured. The non-contact AFM is beneficial in studying the particles on a sample and surface coating.

3. **Tapping (Intermittent) Mode**: In tapping mode, the tip occasionally makes physical contact with the surface while vibrating with an amplitude substantially greater than non-contact mode, typically 100 to $200\,nm$. The Van der Waals forces that interact with the surface diminish the oscillation's amplitude, which alters the tip's deflection as detected by the photodiode. Measurements take longer to complete in tapping mode, but there is less damage to the tip and sample during that time.

We used tapping mode AFM and the images were processed with the free software package Gwyddion [24]). For the measurements presented here we have utilized $AC\,200\,TS$ the sharpened tetrahedral tip from Oolympus Micro Cantilever with the spring constant of $9\,N/m$.

3.5. ASSESSMENT OF ANTIBACTERIAL ACTIVITY OF TEXTILES

There are numerous standart test methods have been suggested for evaluation of the antibacterial activity of textiles by bodies such as the International Organization for Standardization (ISO), the American Society for Testing and Materials (ASTM), Japanese Standarts Association (JSA), Swiss Norm (SN) and the American Association of Textile Chemists and Colorists (AATCC). The most commonly used methods are shown in Table 3.1. Those tests can be divided in two groups: agar diffusion test and suspension test. The agar diffusion test is qualitative, easy to conduct and suitable for screening a large amount of samples. In this method, textile samples is placed in contact with nutrient agar plates which contains bacterial cells and the antibacterial activity is determined by the zone of inhibition (the halo formation).

The suspension test is quantitative, and more time and material consuming. In this method, textile samples are in direct contact with small amount of bacteria. After incubation, bacteria from the fabric are eluted and the total bacterial number is determined by serial dilution. Antimicrobial activity is determined by the percentage of reduction [25]. $AATCC\,147$ and $JIS\,L\,1902-Halo$ techniques permits sample removal, enabling the detection of bacterial growth inhibition beneath it.

The conventional methods advise utilization of Gram-positive and Gram-negative bacteria species. Their susceptibility to antimicrobial agents are different since they have different

Reference	Title	Test
ATCC 147-2004	Antibacterial activity assessment of textile materials: Parallel streak method	Zone diffusion
ATCC 100-2004	Antibacterial finishes on textiles	Suspension
JIS L 1902-1998	Testing method for antibacterial activity of textiles: Qualitative test	Zone diffusion
JIS L 1902-1998	Testing method for antibacterial activity of textiles: Quantitative test	Suspension
EN ISO 20645	Textile fabrics - Determination of the antibacterial activity - Agar plate test (ISO 20645-2004)	Zone diffusion
ISO 20743	Textiles-Determination of antibacterial activity of antibacterial finished products: Absorption method and transfer method	Suspension
SN 195920	Examination of the antibacterial effect of impregnated textiles by agar diffusion method	Zone diffusion
SN 195924	Textile fabrics-Determination of the antibacterial activity: Germ counting method	Suspension
ASTM E2149-10	Standart test method for determining the antibacterial activity of immobilized antimicrobial agents under dynamic contact conditions	Suspension

Table 3.1. Overview of well-known standarts to test the antibacterial efficacy of textiles

cell walls. While the former has a discrete cell envelope made of a thin peptidoglycan layer covered by an outer membrane, the latter has a continuous cell wall formed by a thick peptidoglycan. Therefore, the former are more responsive to antimicrobial agents than the latter [26,27].

In our work, we used AATCC-147 protocols for determining the antibacterial efficacy of the coatings.

3.6. HIGH PERFORMANCE LIQUID CHROMATOGRAPHY

An analytical chemistry standard technique for separating, identifying, and/or quantifying chemicals that are dissolved in a solution is high-performance liquid chromatography (HPLC). A pump, an injector, a separation column, and a detector are the components of HPLC device. Onto the column is injected an aliquot of the sample. Each component in the sample interacts with the column material slightly differently, resulting in various flow rates for the various

components and the separation of the components.

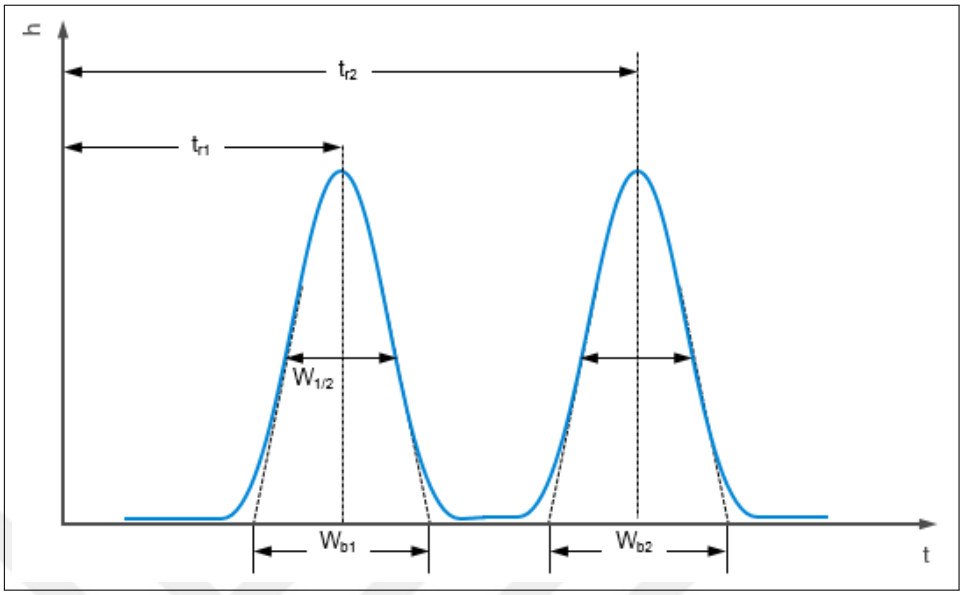


Figure 3.14. Resolution of HPLC

Resolution refers to a column's capacity to distinguish between interest peaks.

$$R = \frac{2(t_{r2} - t_{r1})}{W_{b2} - W_{b1}},$$

where t_{r1} and t_{r1} are the retention times of compounds, and W_{b1} and W_{b2} are the peak widths at baseline as shown in Figure 3.14. Efficiency (N), selectivity (α), and retention (k) are the factors affecting the resolution. The fundamental equation of HPLC is written as

$$R = \frac{\sqrt{N}}{4} \frac{\alpha - 1}{\alpha} \frac{k}{k+1}.$$

Any of these characteristics can be improved to increase resolution. The greatest factor affecting resolution is selectivity. Large swings in resolution are caused by small changes in selectivity. Retention only makes a difference at low k-values. Efficiency is a term used to characterize the column's separation power.

The hormone and antioxidant enzyme activities of tea was analyzed by an Agilent 1200 Series HPLC (Agilent, California, USA) using a Zorbax Eclipse-AAA C-18 column (Agilent, California, USA).

4. ANTIBACTERIAL TEXTILES

Using magnetron sputtering technique, it is possible to obtain hydrophobic, antibacterial, corrosion resistant, flame retardant, or wear resistant textiles, metals, or glasses. In this chapter, antibacterial properties of metal coated cotton textile and lancet by means of magnetron sputtering are investigated for medical applications.

4.1. EXPERIMENTAL DETAILS

4.1.1. Coating of Cotton Textiles

The cotton substrates were cleaned in a mixture of $40\,mL$ water, $0.02\,g$ detergent and $0.02\,g$ sodium carbonate for $1\,g$ textile before deposition. It was heated up to $700\,^{\circ}$ for 45 minutes and then dried.

The cotton samples were stuck on the substrate holder on the top of the magnetron via stickers. The high purity (99.99%) silver (Ag) or copper (Cu) targets (Kurt Lesker, USA) having diameter of $50.8\,mm$ and thickness of $4\,mm$ were placed on the cathode. The sputtered Cu or Ag atoms were deposited independently at the bottom of the cotton sample at room temperature by using magnetron sputtering. The distance between the cotton sample and the metal target was between $5\,cm$ and $8\,cm$.

Prior to deposition, the vacuum chamber was evacuated down until $1x10^{-6}\,Torr$ with help of a turbo pump. After removing the air and all other gases, the argon gas was introduced to the chamber to increase the pressure to $10\,mTorr$. Table 4.1 shows the deposition parameters used in experiments.

4.1.2. Parallel Streak Method

Parallel Streak Method (AATCC TM 147) was used to quantify the antibacterial effectiveness of the coatings. In this method, the bacteria are dispersed on the petri dish filled with agar food, the coated side of the cotton sample is placed on these surfaces and the petri dish is

Table 4.1. Deposition parameters for Ag and Cu coatings

Parameter/Target Type	Silver	Copper
Base Pressure (Torr)	1×10^{-6}	$1 \times 10^{-6} Torr$
Working pressure (Torr)	1×10^{-2}	$1 \times 10^{-2} Torr$
Voltage (V)	$310 - 480$	$440 - 450$
Current (A)	$0.03 - 0.12$	$0.1 - 0.15$
Distance to Target (cm)	$5 - 8$	$5 - 8$
Deposition time (min)	$1 - 20$	$1 - 20$

incubated for 24 hours at $37°$ so that the bacteria can form a colony. If the surfaces are antibacterial, the bacteria can not grow on the agar surface under the cotton, and zones of inhibition are created around the cotton sample. The experiments were conducted with Escherichia coli (E. coli) and Staphylococcus aureus (S. aureus) bacteria. The non-coated cotton was used as the control group.

4.2. RESULTS AND DISCUSSION

In Table 4.2, explanations of the symbols used in the tables for antibacterial activity are listed.

Table 4.2. Explanations of symbols used in tables for antibacterial activity

Symbol	Meaning
*	Uncoated
X	Coated side up
Y	Coated side down
0	Surface does not contain bacteria
+	Surface contain bacteria

4.2.1. Antibacterial Activity of Ag Coated Cotton Towards Escherichia coli and Staphylococcus aureus

E. coli and S. aureus cultures were dispersed on the agar-containing petri dish, and control groups (Figure 4.1) and Ag coated textile was placed on the dishes as shown in Figure 4.2. After the incubation period, the dishes containing both uncoated and Ag coated textiles were observed under the light microscope. A Vernier caliper was used to measure the diameters

of the inactivation zones where the bacteria move away from both sides of the cotton. The diameter of the inhibition zones is shown in Table 4.4 and 4.5.

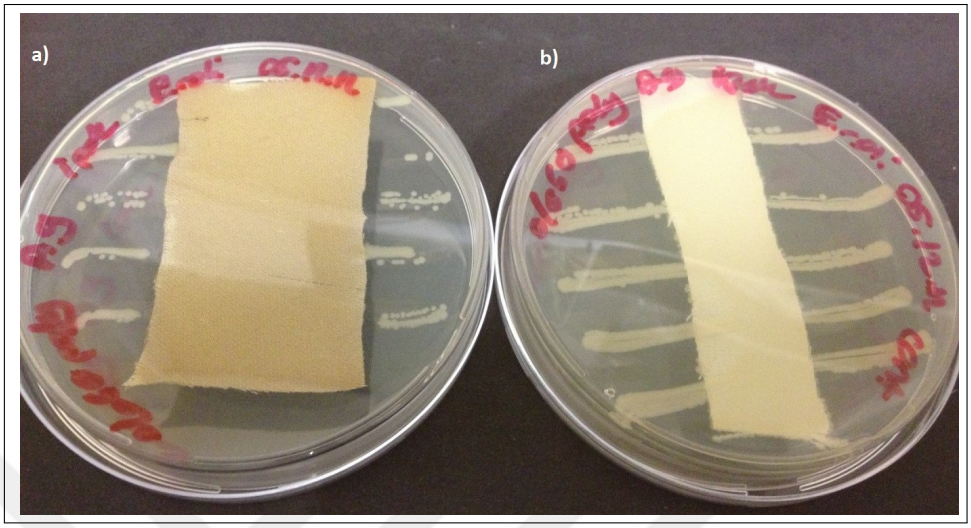


Figure 4.1. E. coli with (a) Ag coated cotton, and (b) uncoated textile

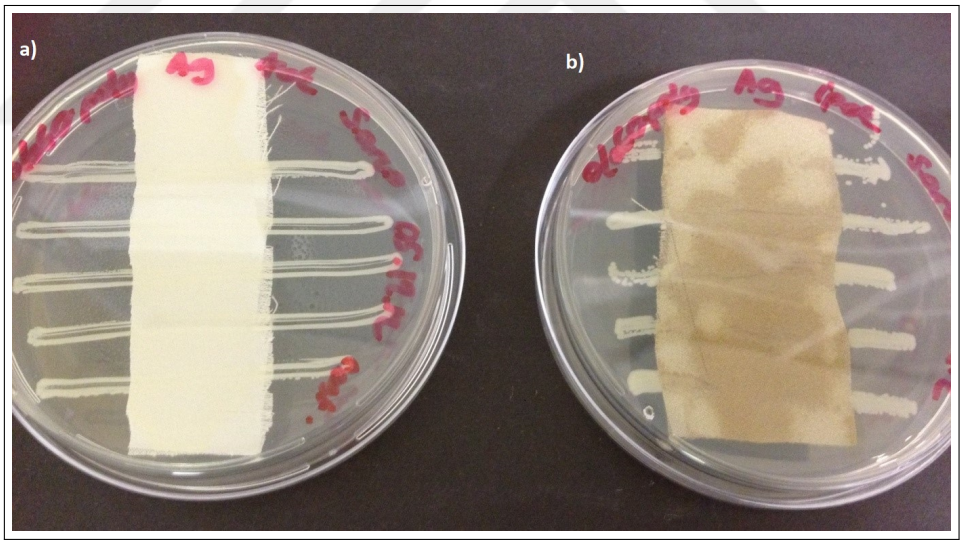


Figure 4.2. S. aureus with (a) uncoated textile, and (b) Ag coated cotton

As can be seen in Table 4.4 and 4.5, Ag-coated cotton is more effective towards S. aureus bacteria.

The inactivation zones around the cotton were about $0.1 - 0.4\,cm$. It indicates that S. aureus did not grow around the Ag-deposited cotton. E. coli grew around the Ag-coated cotton. There was only one strip where $0.2 - 03\,cm$ inhibition zones were measured. In summary, the antibacterial efficacy of silver on S. aureus was significantly higher than E. coli.

Table 4.3. Inhibition zones of uncoated cotton with E. coli and S. aureus

Strip Number	Left (cm)	Right (cm)	Coated side up or down	Surface contain bacteria or not
1	-	-	*	+
2	-	-	*	+
3	-	-	*	+
4	-	-	*	+
5	-	-	*	+

Table 4.4. Inhibition zones of Ag-coated cotton with E. coli

Strip Number	Left (cm)	Right (cm)	Coated side up or down	Surface contain bacteria or not
1	0.1	0.1	Y	0
2	0.8	-	Y	0
3	0.4	0.4	Y	0
4	-	0.2	Y	0
5	0.4	0.2	Y	0

4.2.2. Antibacterial Activity of Cu-Coated Cotton Towards Escherichia coli and Staphylococcus aureus

In a similar way, E. coli and S. aureus bacteria were dispersed on the agar containing petri dish, and control groups (Figure 4.3) and Cu deposited cotton was placed on the dishes as shown in Figure 4.4.

The diameter of the inhibition zones is shown in Table 4.6 and 4.7. As can be seen in Table 4.6 and 4.7, Cu-coated cotton is more effective towards E. coli. The inactivation zones around the cotton were about $0.1 - 0.2\,cm$. It indicated E. coli did not grow around the Cu-coated cotton. S. aureus grew around the Cu-coated cotton. There was only one strip where $0.1\,cm$ inhibition zone was observed. To conclude, the antimicrobial efficacy of copper on E. coli was significantly higher than S. aureus.

Table 4.4, 4.5, 4.6 and 4.7 demonstrate that both Cu and Ag coatings can be used as antibacterial agent on the cotton surfaces. Nevertheless, the Ag-deposited cotton is more effective against E. coli and S. aureus bacteria than the Cu-deposited cotton.

Table 4.5. Inhibition zones of Ag-coated cotton with S. aureus

Strip Number	Left (cm)	Right (cm)	Coated side up or down	Surface contain bacteria or not
1	-	0.1	Y	+
2	-	-	Y	+
3	-	-	Y	+
4	-	-	Y	+
5	-	-	Y	+

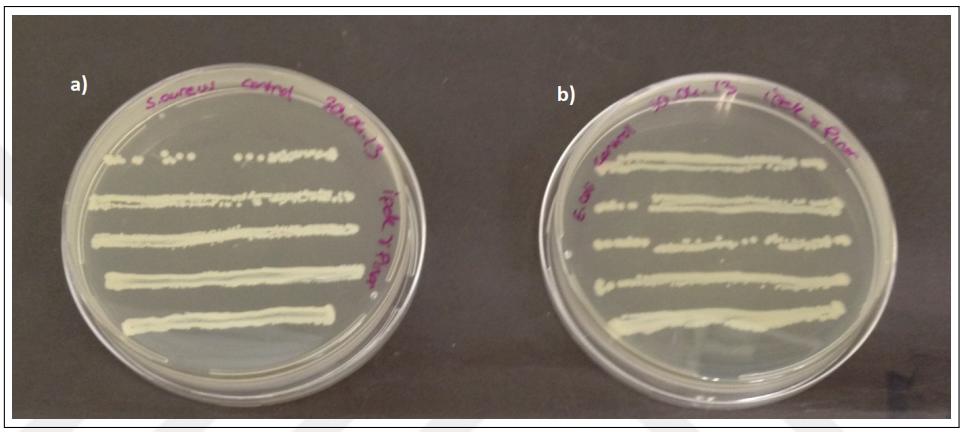


Figure 4.3. Control (a) S. aureus and (b) E. coli

4.2.3. Antibacterial Activity of Ag Coated Lancet Towards Escherichia coli and Staphylococcus aureus

Figure 4.5 shows silver coated lancet. Figure 4.6 shows control groups. Table 4.8 and 4.10 show the results of the measurement of the distance where the bacteria (S. aureus or E. coli) move away from both sides of the lancet coated with and without silver.

Table 4.8, 4.9, and 4.10 indicate that silver-coated lancet is more effective against S. aureus than E. coli.

4.2.4. Mechanism of Action

The mechanism of action of antimicrobial activity of Ag NPs is not yet completely understood. One scientific theory is based on the idea that Ag ions emitted from Ag NPs are the source of

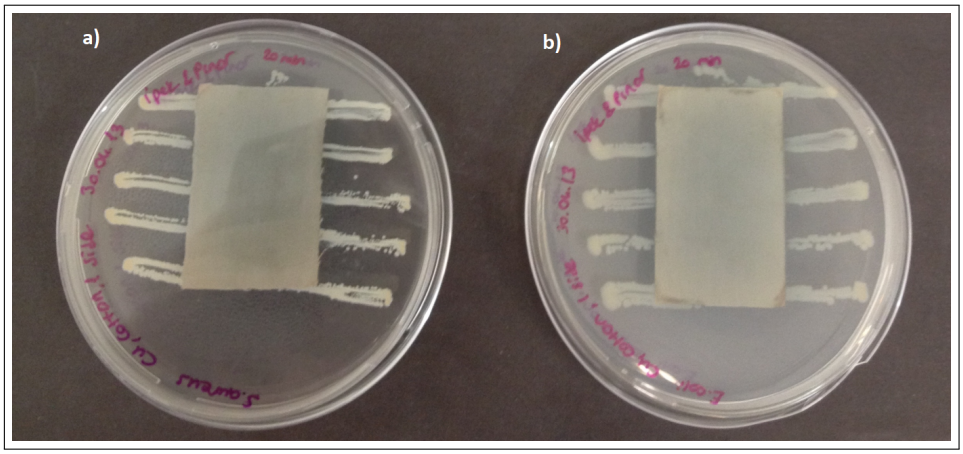


Figure 4.4. Cu coated cotton with (a) S. aureus and (b) E. coli

Table 4.6. Inhibition zones of Cu coated cotton with E. coli

Strip Number	Left (cm)	Right (cm)	Coated side up or down	Surface contain bacteria or not
1	-	-	Y	+
2	0.1	0.1	Y	+
3	0.1	0.1	Y	+
4	0.1	0.2	Y	+
5	-	-	Y	+

the bactericidal effect. [29,30,31,32]. Namely, Ag NPs exposed to dissolved oxygen in water release tiny amounts of Ag^+ according to equation [33]:

$$O_{2(aq)} + 4\,H_3O^+ + 4\,Ag_{(s)} \longrightarrow 4\,Ag^+_{(aq)} + 6\,H_2O$$

Another strategy is based on the findings of Morones et al. [31], who used TEM analysis to discover Ag NPs inside the bacterium and adhered to the cell membrane. Ag NPs are predicted to react with proteins containing sulfur in the membrane and inside of the cell or with phosphorous-containing substances like DNA [34,35] because of Ag's strong affinity for sulphur and phosphorous compounds [36]. As a result, observed morphological changes in bacterial cell membranes and potential DNA damage brought on by reaction with Ag NPs have a negative impact on the cellular processes, ultimately causing the death of the cell [31].

Table 4.7. Inhibition zones of Cu coated cotton with S. aureus

Strip Number	Left (cm)	Right (cm)	Coated side up or down	Surface contain bacteria or not
1	-	-	Y	+
2	0.1	-	Y	+
3	-	-	Y	+
4	-	-	Y	+
5	-	-	Y	+

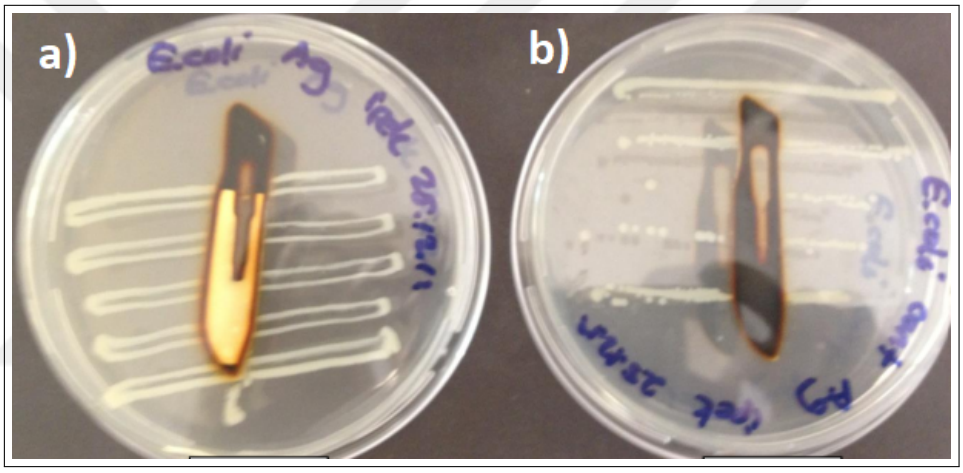


Figure 4.5. E. coli with (a) Ag coated and (b) uncoated lancet

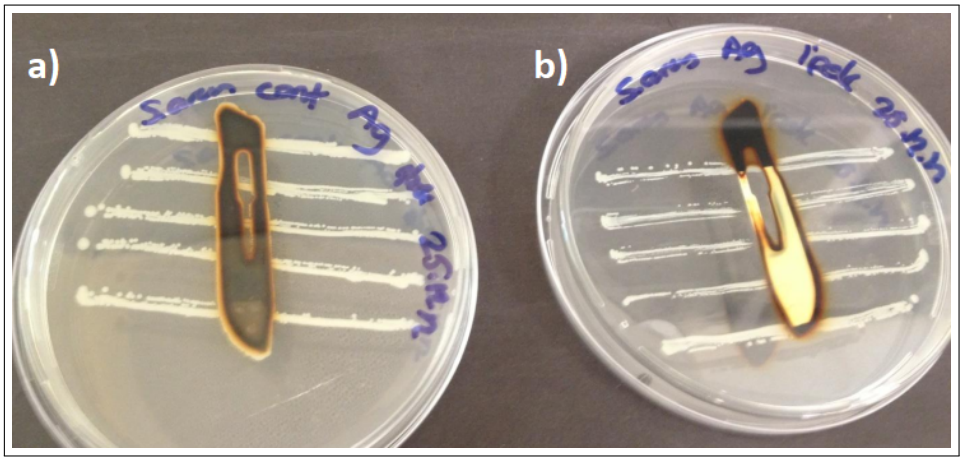


Figure 4.6. S. aureus with (a) uncoated and (b) Ag coated lancet

Table 4.8. Inhibition zones of uncoated lancet (E. coli and S. aureus Control)

Strip Number	Left (cm)	Right (cm)	Coated side up or down	Surface contain bacteria or not
1	-	-	*	+
2	-	-	*	+
3	-	-	*	+
4	-	-	*	+
5	-	-	*	+

Table 4.9. Inhibition zones of silver coated lancet for E. coli

Strip Number	Left (cm)	Right (cm)	Coated side up or down	Surface contain bacteria or not
1	-	-	Y	+
2	-	-	Y	+
3	-	-	Y	+
4	-	-	Y	+
5	-	-	Y	+

Table 4.10. Inhibition zones of silver coated lancet for S. aureus

Strip Number	Left (cm)	Right (cm)	Coated side up or down	Surface contain bacteria or not
1	-	-	Y	+
2	0.3	0.1	Y	0
3	0.2	-	Y	0
4	-	-	Y	0
5	-	-	Y	0

5. TRANSPARENT AND CONDUCTIVE ELECTRODES

5.1. TRANSPARENT CONDUCTIVE OXIDES

Transparent conductive oxides (TCOs) are a type of material, which pose the distinctive capability of being both optically transparent in the visible region of the electromagnetic spectrum and yet electrically conductive. These materials are widely used in optoelectronic device applications such as solar cells, electrochromic devices, LEDs, flat panel displays, touch screens, plasma screens, etc.

Combining high optical transparency and electrical conductance in the film can be done either in thin metallic films (Ag, Au, or Cu), whose thicknesses are a few nanometers or heavily doped metal oxide semiconductor thin films, which are mostly used nowadays.

TCOs are composed of metal (or metal combinations) M and nonmetal N which consists of oxygen. The semiconductor compounds M_xN_y exhibit different optical and electrical characteristics and these properties can be altered by using dopant material D (metals, metalloids, or nonmetals) and the new material can be shown as $M_xN_y : D$.

Two simultaneous requirements are generally accepted to define metal oxide TCOs [37,38]: It must be conducting such that its sheet resistance is lower than $10\,\Omega/cm$. Therefore it should have a carrier density of the order of $10^{21}\ cm^{-3}$, which can be achieved by degenerated doping. Oxygen vacancies and/or interstitial metal atoms are responsible for high concentrations of free electrons [39]. It should be transparent to sunlight, which is fulfilled by band-gap energy above $3\,eV$.

Tin-doped indium oxide or Indium Tin Oxide (ITO), fluorine-doped tin oxide (FTO), aluminum doped zinc oxide (AZO), gallium doped zinc oxide (GZO) and titanium dioxide (TiO_2) are the examples of various materials used as TCO.

ITO is the industry standard TCO due to its two unusual characteristics, its electrical conductivity, and its optical transparency. However, indium is rare metal on the earth. So, it is very expensive compared to conventional metals. Also, Indium is a rare element, therefore, there is a huge amount of research on replacing ITO. For instance, carbon nanotubes

(CNTs), graphene, metallic networks, etc. AZO is the common choice of TCO because of the abundance of Al and Zn.

5.1.1. Indium Tin Oxide

ITO is composed of indium (III) oxide (In_2O_3) and tin (IV) oxide (SnO_2), with typically $90\%wt\ In_2O_3, 10\%wt\ SnO_2$. Indium oxide has a cubic bixbyite structure. The bixbyite structure is analogous to the fluorite structure, but one-fourth of the anions are vacant, allowing for small shifts of the cations. The two non-equivalent In sites present in In_2O_3 cubic bixbyite crystal structure are shown in Figure 5.1. In $In-1$ site, the indium atom has 6 equidistant oxygen anion neighbors and the oxygen atoms are at the corner of the cubes with 2 oxygen vacancies along one body diagonally. While in $In-2$ site, indium atoms are separated from 6 oxygen anions at 3 different distances, the oxygen anions are at the corners of the cube, with 2 oxygen vacancies along one face diagonally. These vacancies are responsible for the high electrical conductance of In_2O_3.

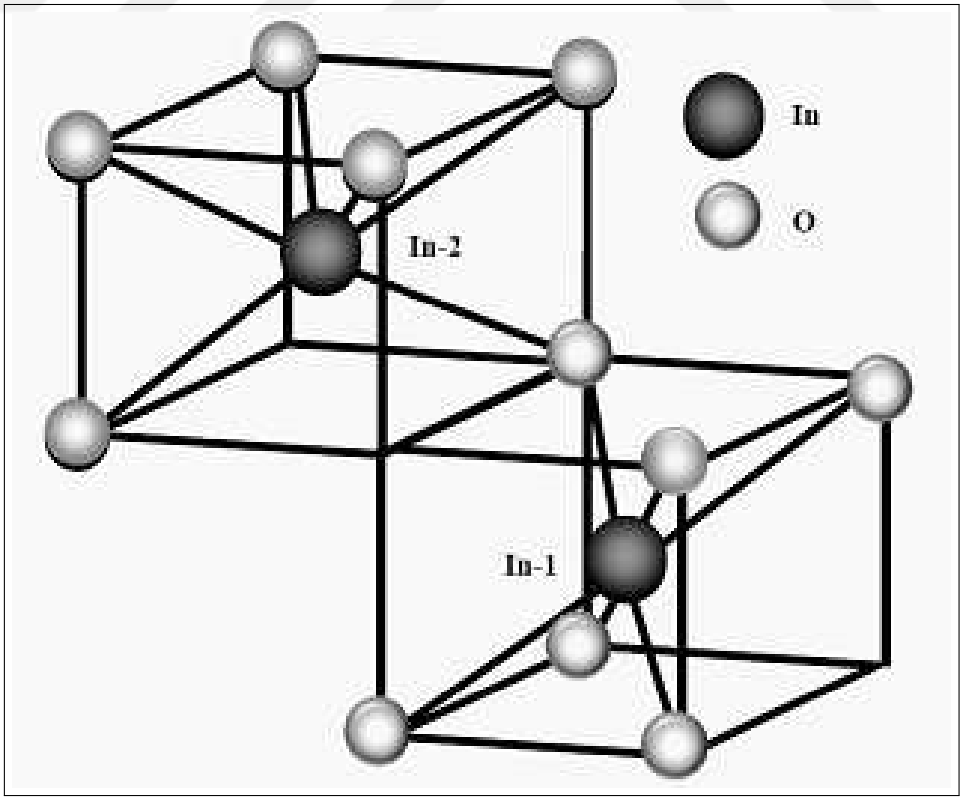


Figure 5.1. Crystal structure of ITO

ITO is formed by substitutional doping of In_2O_3 with tin, which replaces the In^{+3} atoms from the cubic bixbyte structure of indium oxide. The material retains its bixbyite structure and has a lattice parameter close to that of In_2O_3. The doped *Sn* forms an interstitial bond with oxygen either as *SnO* or SnO_2 and accordingly it has a valency of +2 or +4. This valence state plays a crucial role in the conductivity of ITO. At a lower valence state i.e., *SnO* state, a hole is created, which acts as a trap and as a result, a reduction in carrier concentration is observed. On the other hand, the prevalence of the higher valance state i.e. SnO_2 state acts as an *n*-type donor, releasing electrons to the conduction band and increasing the carrier concentration. Nevertheless, in ITO, both substituted tin and oxygen vacancies contribute to high conductivity. However, too many oxygen vacancies and high *Sn* concentration may lead to a reduction in transmission [40]. To optimize the properties, the control of the *Sn* doping and non-stoichiometric are necessary. In solid form ITO is typically pale yellow to greenish yellow colored material which depends on SnO_2 concentration. The density of ITO is $7.14 g/cm^3$ and the melting point is $\sim 1900\,^{\circ}C$. Nowadays ITO has low electrical resistivity ($\sim 10^{-4}\,\Omega.cm$) and excellent transparency ($\sim 80\%$) in the visible range. ITO has the highest carrier density of $1.52 \times 10^{21}\ cm^{-3}$ with 10 percent of tin doping [40].

5.1.2. ITO/Metal/ITO Structures

To increase conductivity while still maintaining transparency, an intermediate metal layer is embedded between two ITO layers [37]. In this way, the usage of indium is decreased, as well. Due to their low surface resistivity, silver [41] and copper [42,43] are widely used as the intermediate metals. Furthermore, gold [44,45], aluminum [46], nickel [47,48], and platinum [49] were also studied. Chen et al [50] used silver-titanium alloy as an intermediate layer for the anti-corrosive property. Chemelli et al [51] used gold-titanium bi-layer for electric field shielding application. Chen et al [52] investigated the insertion of ultrathin titanium nitride as plasmonic material for near-infrared wavelengths.

To the best of our knowledge, this is the first work that titanium (Ti) is used as the incorporated metal. Ti is known as the 9th most abundant metal on the earth [53].

In this work, single ITO layers and ITO/metal/ITO (IMI) multilayer thin films, as shown in

Figures 5.2 and 5.3, were deposited on glass by using magnetron sputtering. The thickness of ITO monolayer and IMI trilayer structures was $90\,nm$ (See Figure 5.4), which is common for photovoltaic applications.

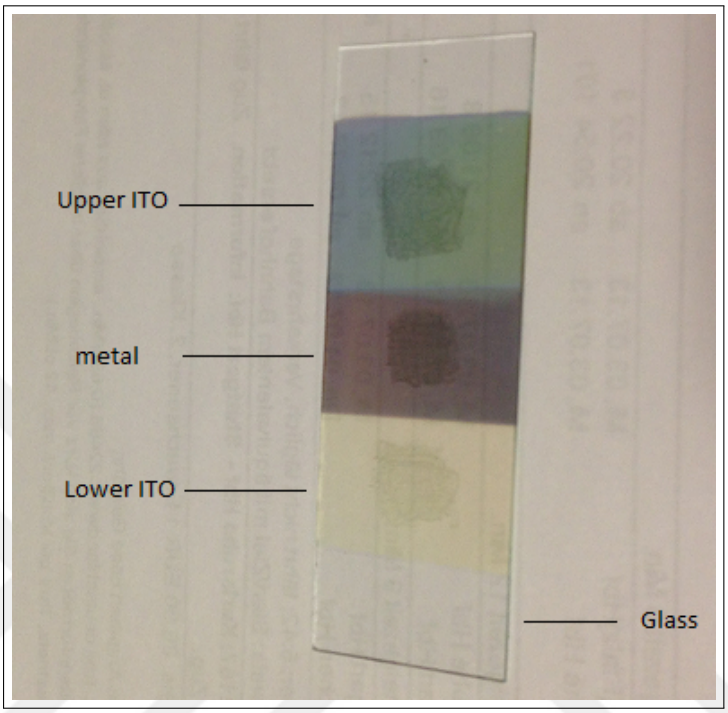


Figure 5.2. Top view of IMI deposition

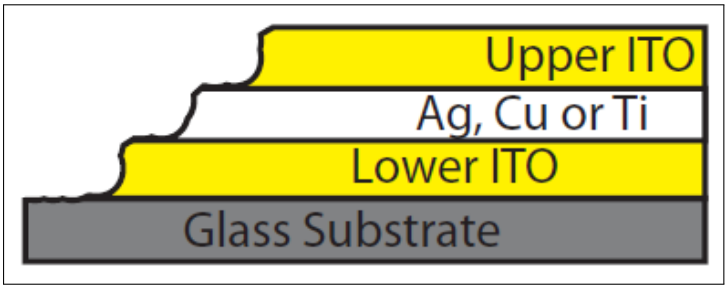


Figure 5.3. Side view of IMI structures

5.2. EXPERIMENTAL DETAILS

All experiments conducted during the thesis can be divided into three sets according to the types of deposited thin films, the carrier gas, and the power supply, as shown in Table 5.1. The structural, optical, and electrical characteristics of ITO monolayers, and the sandwich structures of ITO/Ag/ITO (IAI), ITO/Cu/ITO (ICI), and ITO/Ti/ITO (ITI) multilayer films



Figure 5.4. ITO monolayer and IMI trilayer structures

were investigated by stylus profilometer, scanning electron microscopy (SEM), atomic force microscopy (AFM), energy dispersive X-ray analysis (EDX), photoluminescence spectroscopy, spectroscopic ellipsometry, and four-point probe method.

Table 5.1. The classification of conducted experiments

Set of Experiments	Deposited Thin Films	Carrier Gas	Power Supply
1	ITO, IAI	$Ar + O_2$	DC
2	ITO, IAI, ICI, ITI	Ar	DC
3	ITO, ITI	Ar	DC, RF

5.2.1. The First Set of Experiments

In the first set of experiments (SE-1) ITO single layer and IAI multilayer thin films were deposited on glass microscope slides (Pearl, $26 \times 76 \times 1\,mm$) by magnetron sputtering technique. To prepare a clean adhesion surface, the slides were initially treated with acetone for $10\,min$ and cleaned ultrasonically in ethanol for $20\,min$, and then left to dry for $10\,min$.

The change in color as shown in Figure 5.2 results from stair-like deposition to measure the thickness of the layers. The shadows on the rear of the glass are deliberately made by roughing it to eliminate the back reflection of light in ellipsometric studies. (Another solution is the usage of a immersion fluid having the same index of refraction as the glass) [55]. Table 5.2 shows the deposition parameters for SE-1.

The deposition system (Nanovak NVSS330, Turkey), shown in Figure 2.7, is equipped with both RF and DC sputtering sources. In SE-1, the DC source is used. The Ag target from Nanovak, Turkey ($50,8\,mm$ diameter $4\,mm$ thickness) and ITO target from Kurt Lesker, USA ($50,8\,mm$ diameter $3,2\,mm$ thickness) were used (both of $99,99\%$ purity). The distance between the target and the substrate was kept at $50\,mm$. The vacuum chamber was evacuated

Table 5.2. Deposition parameters of IAI for SE-1

Target Type	Time (min)	O_2 (%)	Pressure ($Torr$)	Voltage (V)	Current (A)
ITO	21	8	5.10×10^{-2}	280	0.15
Ag	3	3	3.30×10^{-2}	380	0.06
ITO	21	7	5.45×10^{-2}	280	0.15

Table 5.3. The coating time and thicknesses of ITO monolayers SE-1

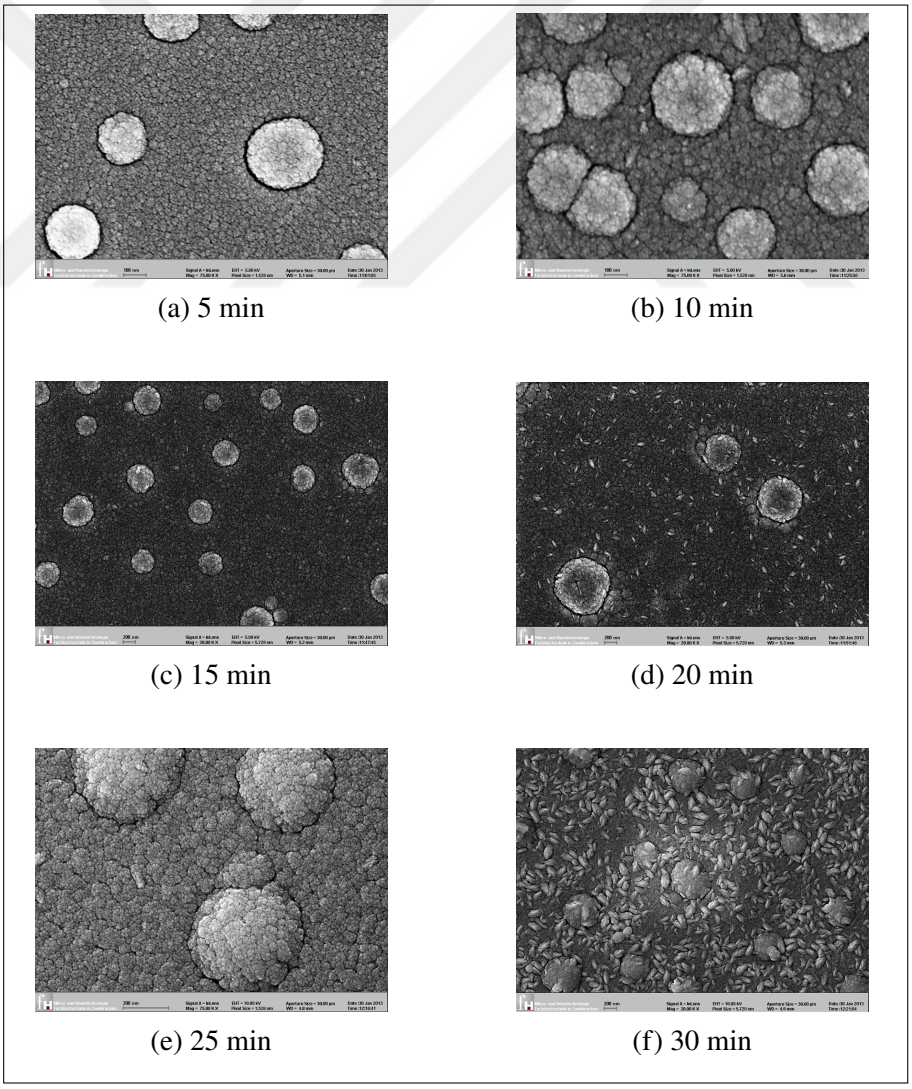
Sample	Time (min)	Thickness (nm)
1	5	150
2	10	360
3	15	590
4	20	930
5	25	1070
6	30	1400

Table 5.4. Measurement of the film thickness of IAI multilayers SE-1

Thickness (nm)	Lower ITO	Ag	Upper ITO
Sample 1	120	55	210
Sample 2	110	40	185

down to pressure $1 \times 10^{-6}\,Torr$ prior to deposition. Then Ar and O_2 gases were sent into the chamber to set the required pressure $1 \times 10^{-2}\,Torr$.

Firstly, ITO monolayers were deposited on the glass slides by using the sputtering system. The oxygen percentage was 8. The power density was greater than recommended power limit of $63\,W$. The first ITO target used was broken due to exceeding the limit. To get thin films with different thicknesses the coating time was changed from 5 to 30 minutes. Then, IAI multilayer thin films were obtained. The deposition time and thickness measurements of single ITO layers are shown in Figure 5.3. The deposition parameters and the thicknesses of IAI thin films for SE-1 are shown in Table 5.2 and Table 5.4. The thickness measurements were done by using a Dektak3 Surface profilometer (See Figure 3.2).

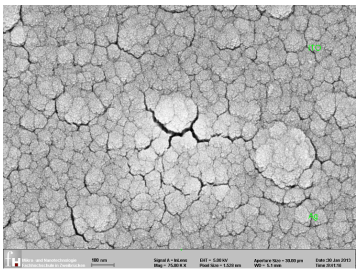


(a) 5 min (b) 10 min

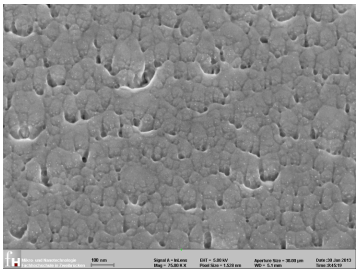
(c) 15 min (d) 20 min

(e) 25 min (f) 30 min

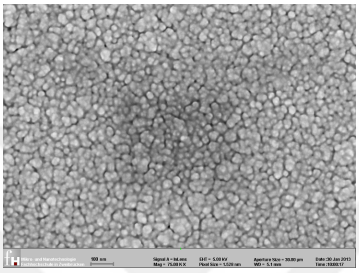
Figure 5.5. ITO monolayer deposition



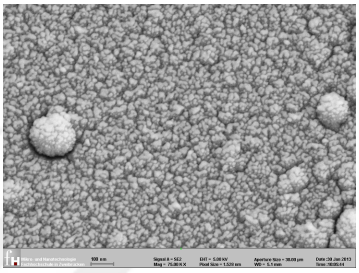
(a) Top ITO layer



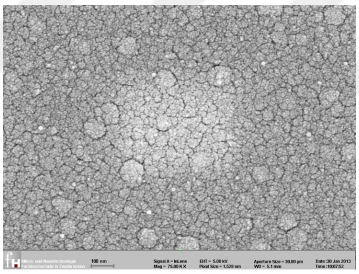
(b) Interface of top ITO layer and Ag layer



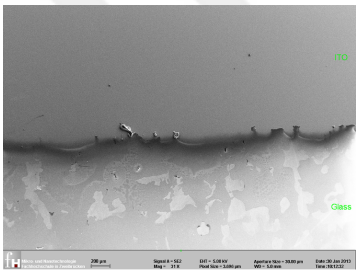
(c) Ag layer



(d) Interface of bottom ITO layer and Ag layer

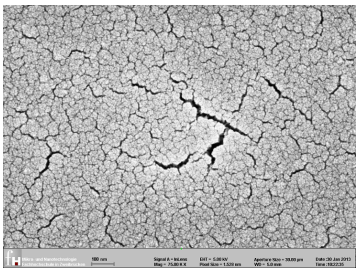


(e) Bottom ITO layer

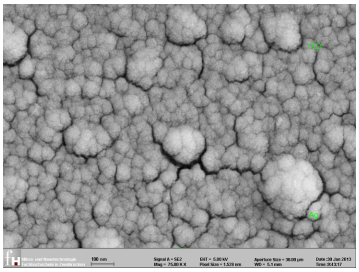


(f) Interface of bottom ITO and glass

Figure 5.6. ITO-Ag-ITO multilayers on glass



(a) Interface of bottom ITO layer and glass



(b) Top ITO layer

Figure 5.7. The cracks due to the temperature of the magnetron sputtering

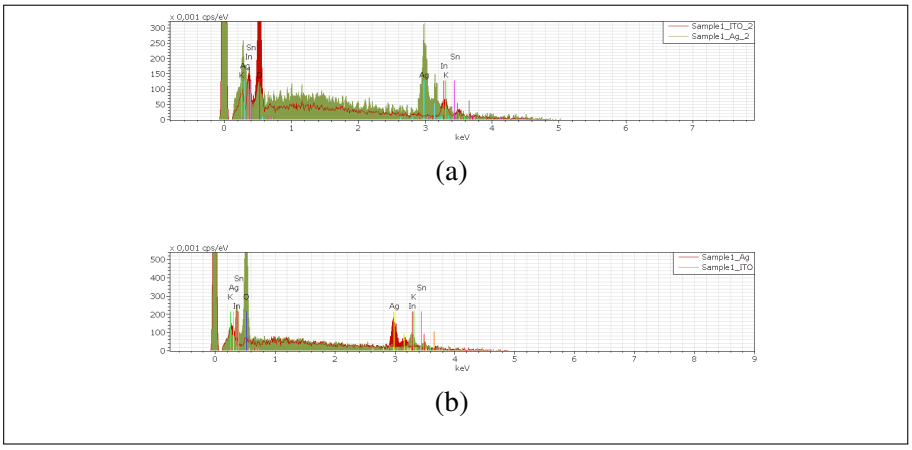


Figure 5.8. EDX analysis of IAI multilayer thin films

Figure 5.5 shows the amorphous cauliflower structure. There are cracks in Figures 5.6-5.7. This is because of the temperature of the sputtering process. There are peaks in EDX.

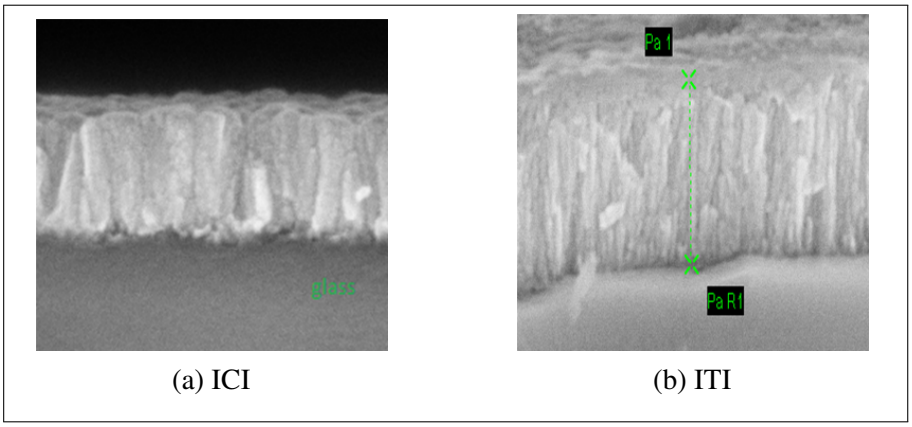
5.2.2. The Second Set of Experiments

The deposition parameters for the second set of experiments (SE-2) are shown in Table 5.5.

Table 5.5. Deposition parameters of SE-2

Parameters	Values
Base pressure (Torr)	1×10^{-6}
Working pressure (Torr)	1×10^{-2}
Voltage (V)	$300 - 450$
Current (A)	$0.02 - 0.15$
Interelectrode distance (cm)	$5 - 8$
Working gas	Ar
Power supply	DC
Targets	ITO, Ag, Cu, Ti
Substrate	Soda lime glass

Even though we implemented the stylus, ellipsometry, and SEM, we could not measure the thickness of the metal layer due to the islands growth or diffusion into the ITO layer. However, EDX analysis has at least shown Ag and Cu peaks, and the existence of Ti nanoparticles. Na, Ca, and Mg peaks, as seen in Figure 5.10 and 5.12, come from the glass and Al is due to the chamber.



(a) ICI (b) ITI

Figure 5.9. SEM images of the cross-sections of ICI and ITI on glass for SE-2

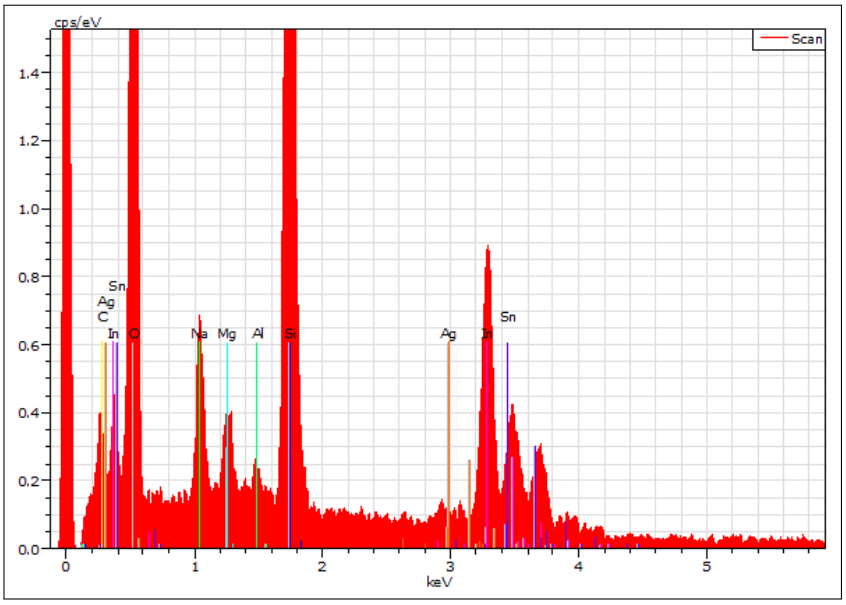


Figure 5.10. EDX Analysis of IAI Multilayer for SE-2

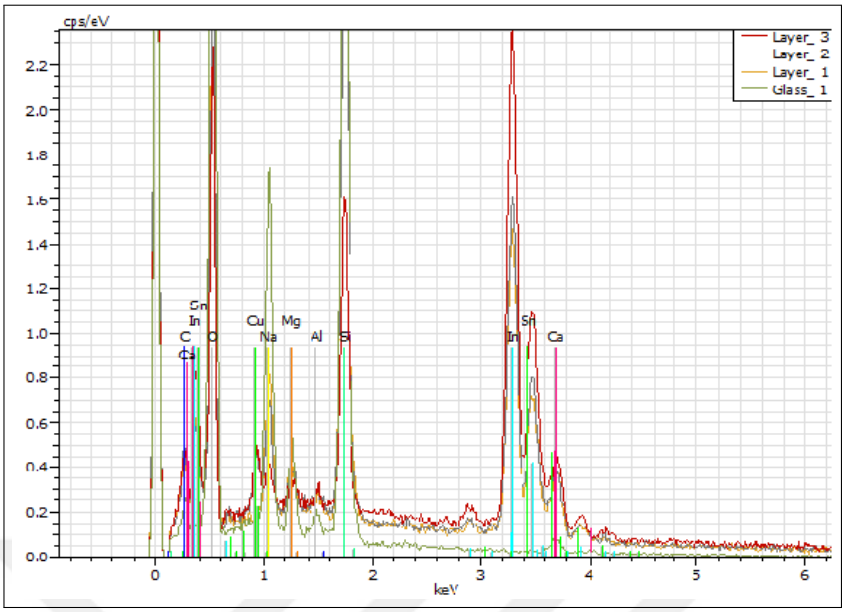


Figure 5.11. EDX Analysis of ICI Multilayer for SE-2

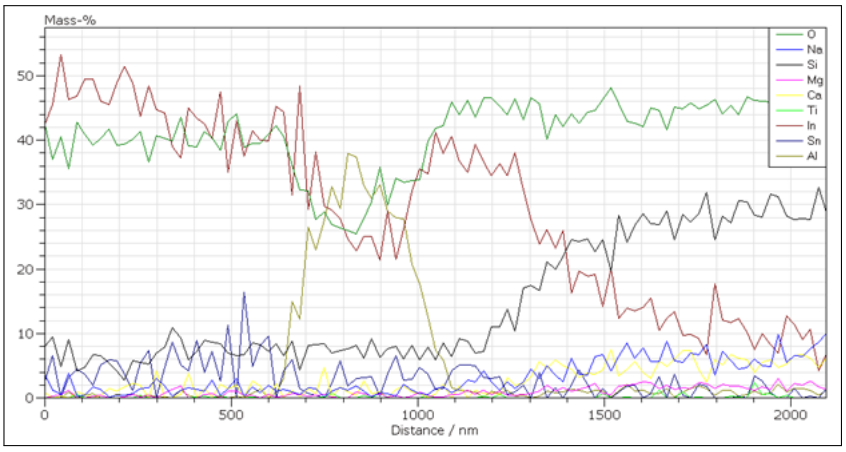
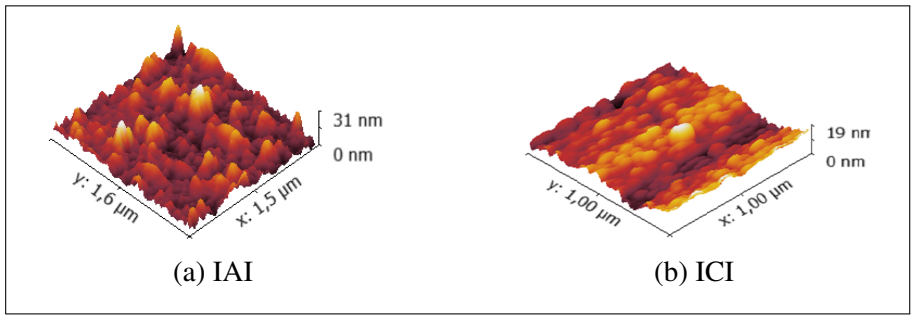


Figure 5.12. EDX Analysis of ITI Multilayer for SE-2

Ag and Cu peaks are seen but those of Ti are not. It means that Ti atoms did not get crystallized. The bright green line near to x-axis shows Ti, which is a tiny amount. There was no Ti peak, so we used the mass-ratio vs distance graph.



(a) IAI (b) ICI

Figure 5.13. AFM images of the intermediate layer of IAI and ICI structures for SE-2

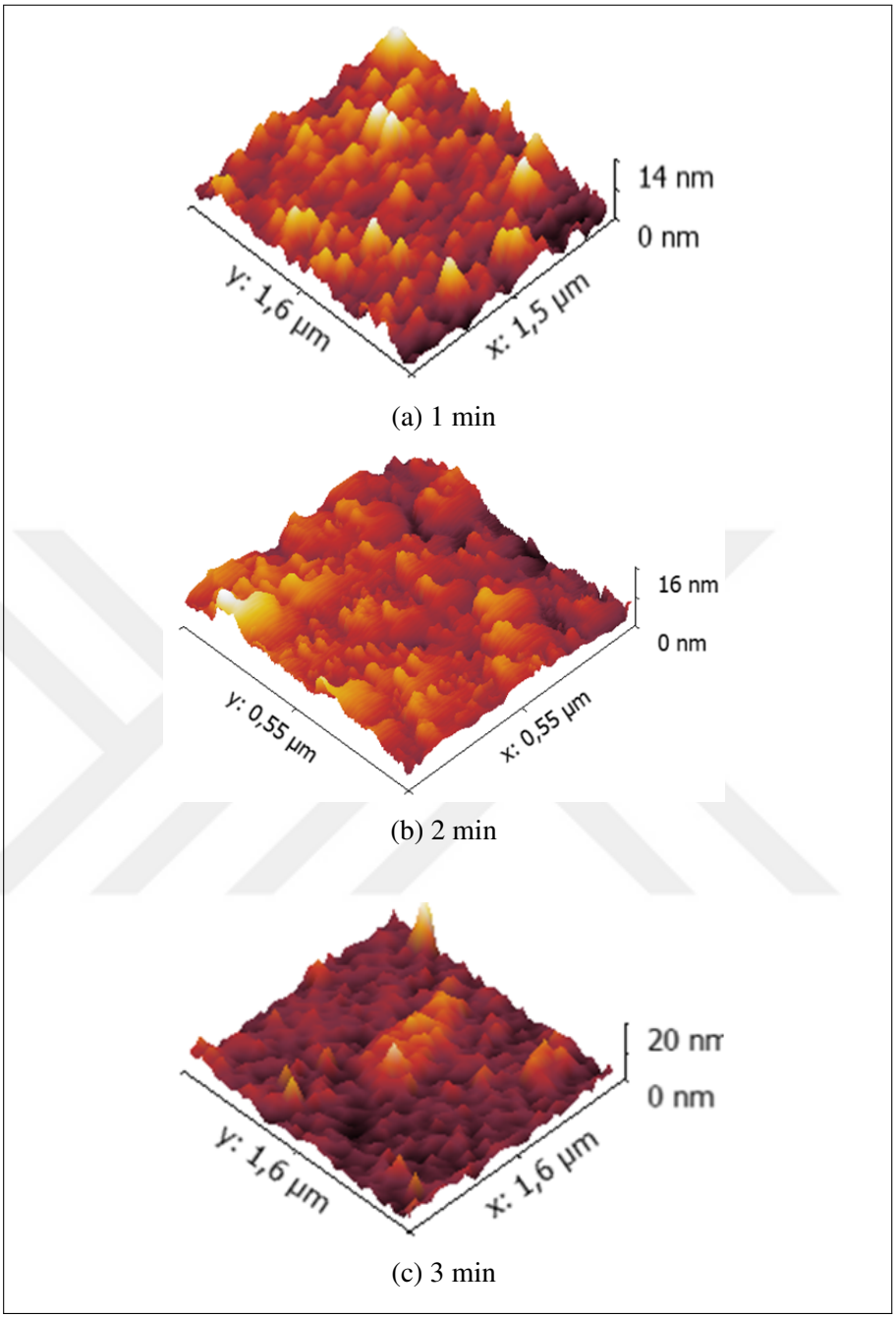
Figure 5.13 shows AFM images of the intermediate layer of IAI and ICI structures for SE-2. The grain size of IAI is greater than that of ICI. Figure 5.14 demonstrated that $1\,min\,Ti$ coating produces an amorphous structure, and $3\,min\,Ti$ coating grain sizes were increased. Furthermore, roughness is increased and grains became coalescent. Figure 5.15 shows the optical transmission spectra of ITO monolayers and ITI trilayers fabricated in SE-2.

5.2.3. The Third Set of Experiments

To overcome the difficulties encountered before, the repeated experiments were conducted in clean room environment using a multi-target sputtering system at the Nanotechnology and Biotechnology Institute of İstanbul University.

We have prepared single ITO layers ($90\,nm$ thick) and ITI multilayers with a total thickness of $90\,nm$ on borosilicate glass (BK7) and soda lime glass (SLG) by magnetron sputtering. The structural properties of the samples prepared are shown in Table 5.6, and the deposition parameters for the third set of experiments (SE-3) are shown in Table 5.7. We have used photolithography for calibrating the magnetron sputter (See Figure 5.16). The thickness was measured by using NanoMap 500LS 3D Scanning Contact Surface Profilometer (See Figure 3.3).

We have used VAKSİS PVD-Handy-3M Dual Magnetron Sputtering System, shown in Figure 2.11 and 2.12 to coat samples in SE-3. The targets were ITO ($In_2O_3 : SnO_2 = 90 : 10 wt.\%$)

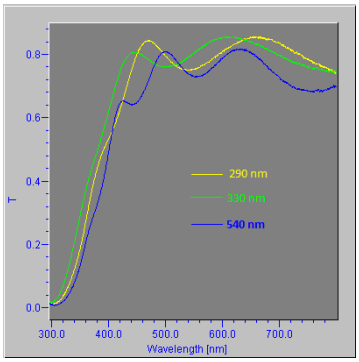


(a) 1 min

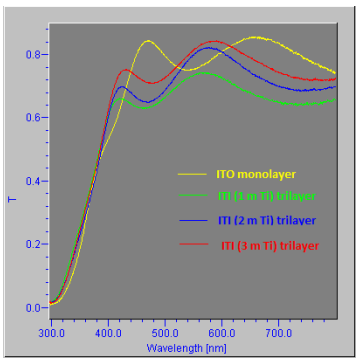
(b) 2 min

(c) 3 min

Figure 5.14. AFM images of the incorporated layer of ITI with different coating times of Ti for SE-2



(a) Single ITO layers with different thicknesses



(b) ITO monolayers and ITI trilayers with different thicknesses

Figure 5.15. Transmission spectra of ITO monolayers and ITI multilayers for SE-2

Table 5.6. The structure of the samples prepared for SE-3

Film Thickness (nm)	Bottom *ITO*	*Titanium*	Top *ITO*
BK7-ITO	90		
BK7-ITI-6	42	6	42
BK7-ITI-10	40	10	40
BK7-ITI-14	38	14	38
SLG-ITO	90		
SLG-ITI-6	42	6	42
SLG-ITI-8	41	8	41
SLG-ITI-10	40	10	40
SLG-ITI-12	39	12	39
SLG-ITI-14	38	14	38

and Ti with a purity of 99.99% from Kurt Lesker Company. The substrates were cleaned prior to deposition by deionized water, acetone, isopropanol (in a ultrasonic bath), deionized water in turn, and then dried by nitrogen gun. The vacuum chamber was evacuated down to a base pressure around $0.05\,mTorr$, and then the argon gas was sent into the chamber yielding a sputtering pressure of $8\,mTorr$. Following the recommendation of Kurt Lesker Company [56], we have used ramp-up and ramp-down procedures when we apply or reduce power with the rate of $10\,\frac{watts}{min}$, since ITO is a ceramic target.

Three ITO monolayer and twelve ITI multilayer thin films having thickness of $90\,nm$ were deposited on BK7 and SLG. Then, the transparency and sheet resistance of these samples were measured by using photoluminescence spectrophotometer, spectroscopic ellipsometry

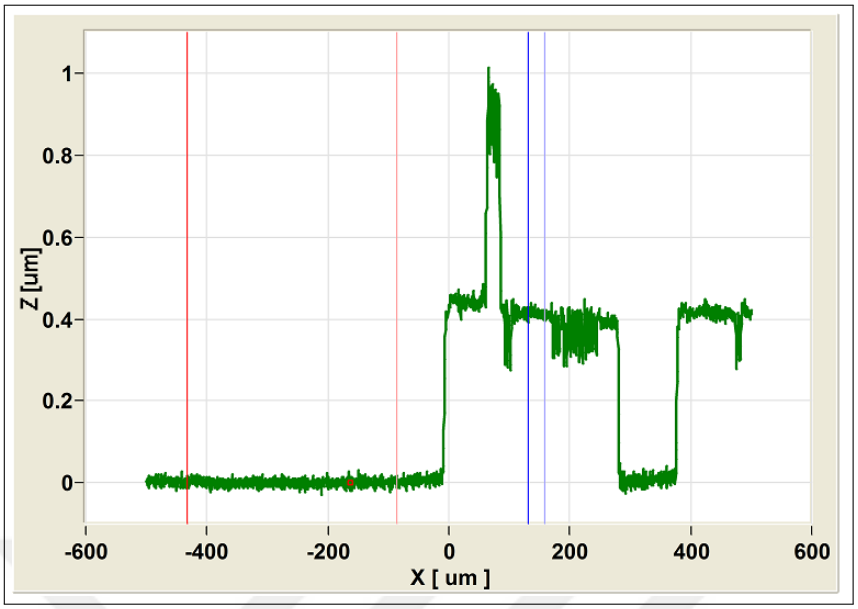


Figure 5.16. Profilometry for deposition rate for ITO (VAKSİS) for SE-3

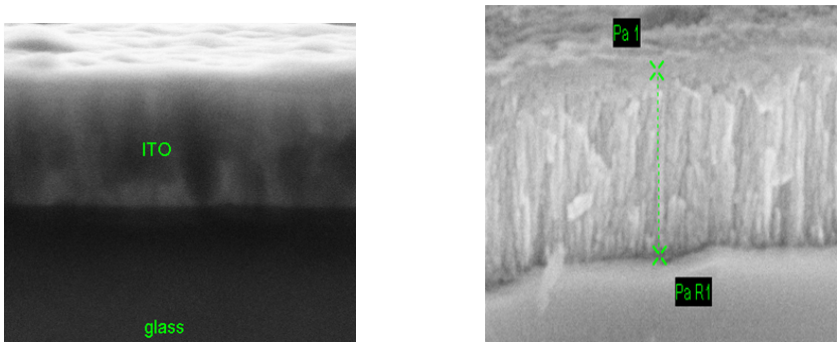
Table 5.7. Deposition conditions for SE-3

Parameters	ITOtarget	Ti Target
Base pressure (mTorr)	0.05	0.05
Working pressure (mTorr)	8	8
Working gas	Ar	Ar
Power supply	RF	DC
Power (W)	60	100
Deposition rate (nm per min)	2	7
Interelectrode distance (cm)	5	5
Substrates	SLG and BK7	

and four-point probe.

The optical transmission of ITO ($90\,nm$) and ITO($40\,nm$)/Ti($10\,nm$)/ITO($40\,nm$) sample as shown in Figure 5.18 was measured by Acton SP2300A Spectrometer of Princeton Instruments, USA (See Figure 3.6).

The optical transmission of the samples listed in Table 5.6 was measured by using spectroscopic ellipsometry of SENTECH SE850, Germany (See Figure 3.5).



(a) ITO (b) ITI

Figure 5.17. SEM images of the cross-sections of ITO and ITI deposited on glass for SE-3

5.3. RESULTS AND DISCUSSION

5.3.1. Structural Composition

The deposition parameters for the sputtering process are important for obtaining a good quality ITO.

There is a big variation in transparency and conductivity when varying the deposition rate. In some cases, one can obtain a good transparent ITO but with very high resistivity. When the deposition rate was very high a totally black and insulating ITO is obtained.

Another important factor is the partial pressure of oxygen in the deposition chamber. ITO conducts electricity because of an under-stoichiometry in oxygen. Therefore the oxygen incorporation level in the film is crucial. In conclusion, deposition parameters play a fundamental role in obtaining good quality ITO. These parameters should be modified carefully.

For a good quality ITO $50\,nm$ thick one should read something in the range of 50 – $100\,ohm/sq$. Once one is confident about the quality and repeatability of ITO, then Ti can be added to see if conductivity improves. Ti is a metal that is easily oxidized.

To deposit a good Ti, one must take care to have a good vacuum base level in the deposition chamber and avoid oxygen contamination. As it is known, Ti is normally used as a getter material for a vacuum chamber, because it absorbs oxygen and other gases very rapidly. This

is the reason why Ti causes a worsening of the conductivity for such samples. It is oxidized, despite all efforts in keeping a good vacuum in the chamber.

For very low thicknesses we obtain not a continuous film but rather a collection of nanoparticles not interconnected among them, therefore we cannot improve electrical conductivity. For gold and silver, it is observed that a thickness of at least $12 - 14\,nm$ is necessary to make the nanoparticles coalesce and form a continuous film. This critical thickness may vary as a function of the metal and also on the deposition method, but as a thumb rule, we assume that at least $10\,nm$ is necessary.

In the first set of experiments, we also used oxygen gas and the results were better. In some coatings with the same deposition time, the different thickness was obtained. This is because the deposition system becomes stable after some time.

5.3.2. Sheet Resistance

Sheet measurements were done by means of a 4-point probe system shown in Figure 3.9. For the IAI electrode, we have found that the sheet resistance of the IAI trilayer is 70 times greater than ITO monolayer [57]. However, we have had difficulty in measuring the sheet resistance. In fact, sometimes we got results with the order of $M\Omega$. The best result for sheet resistance of ITI and ITO were found to be around 300 and $900\,\Omega/square$, respectively, which are similar to the results of Kulkarni et al [58,59,60] and Chauhan et al [61]. Nevertheless, the percentage of average sheet resistances of ITO and ITI was around 3. To improve the results presented here, more experiments should be done by varying the parameters to obtain optimum conditions. In addition, annealing and incorporation of oxygen can give better results. With the results presented here, it was qualitatively demonstrated that ITI multilayers are 3-order more conductive than ITO monolayers, which is a promising observation.

5.3.3. Optical Transparency

It is seen that the transparency of the ITI trilayer structure increases as the thickness of the intermediate metal layer increases in Figure 5.18. A similar phenomenon was also observed in

Figures 5.19 and Figure 5.20. These figures show the optical transparency spectra of ITO and ITI thin films deposited on soda-lime glass (SLG) and boro-silicate glass (BK7), respectively. In those figures, the number shows the thickness of Ti layer in *nm* and the total thickness of each sandwich structure is $90\,nm$. Both graphs demonstrate that the transparency of ITI multilayers is comparable to ITO monolayer, but ITI-6 shows greater transparency which can be explained by the island growth formation (The film is not continuous). Around $450\,nm$, it increases up to $\%90$, behaving like SLG (see Figure 5.19). Between $350 - 570\,nm$ it is more transparent than BK7 (See Figure 5.20). As is seen in Figure 5.19, the transmittance spectrum of ITI-12 is a bit greater than ITI-14. This difference is much more clear in the Figure 5.20, where the optical transparency of ITI-12 is greater than ITI-14. These phenomena can be explained by the surface plasmon resonance (SPR) effect of the intermediate Ti layer. There is absorption around $830\,nm$ in Figure 5.18. That shows that this coating can be used as a filter around $800\,nm$.

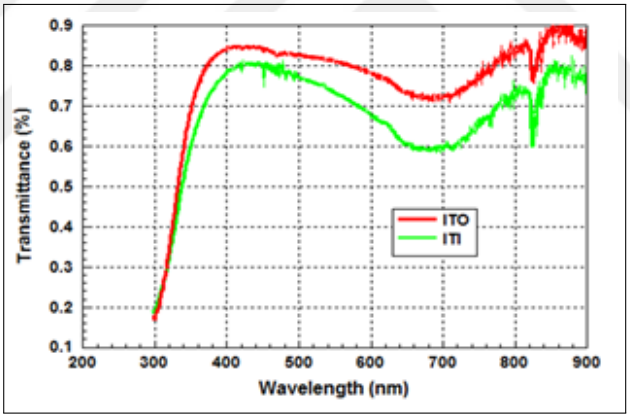


Figure 5.18. Optical transmittance of ITO and ITI thin films on glass for SE-3

5.3.4. Lorentz and Drude Models

Consider a free electron model with damping. Its electronic oscillations with the applied electric field can be found from Newton's second law

$$m\ddot{x} = F_{driving} + F_{damping} + F_{spring} = qE - m\gamma\dot{x} - m\omega_0^2 x$$

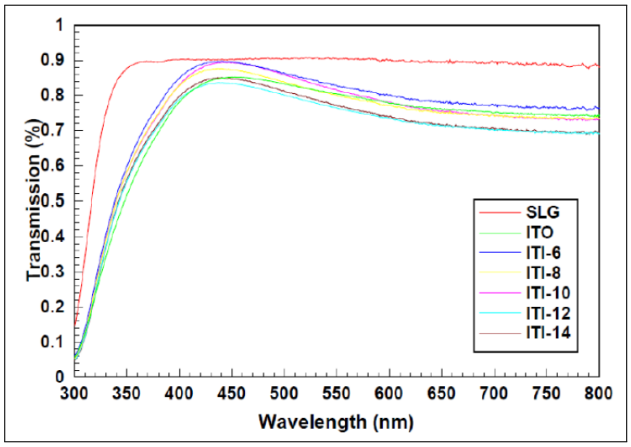


Figure 5.19. Transmittance spectra of ITO and ITI thin films deposited on SLG for SE-3

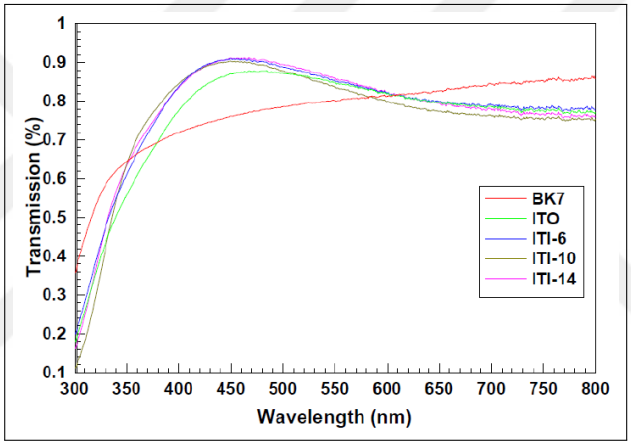


Figure 5.20. Transmittance spectra of ITO and ITI thin films deposited on BK7 for SE-3

where $x, m, q, \gamma, \omega_0$, and ω are the displacement, effective mass, and the charge of an electron; the damping factor, the resonance frequency, and the frequency of the incident light. This equation leads to:

$$\ddot{x} + \gamma\dot{x} + \omega_0^2 x = -\frac{eE_0}{m} e^{i\omega t}, \tag{5.1}$$

where we have used $E = E(t) = E_0 e^{i\omega t}$. To find the solution, it is assumed that

$$x(t) = Ae^{i\omega t},$$

where A is a constant. Substituting this into Equation 5.1, one gets

$$A = \frac{eE_0}{m}\frac{1}{\omega_0^2 - \omega^2 - i\gamma\omega}$$
$$x(t) = \frac{eE_0}{m}\frac{1}{\omega_0^2 - \omega^2 - i\gamma\omega}e^{i\omega t} .$$

Since ex is the polarization of one oscillator, the total polarization becomes

$$P = N_0 ex = \frac{N_0 e^2}{m}\frac{1}{\omega_0^2 - \omega^2 - i\gamma\omega}E_0 e^{i\omega t} = \frac{\omega_p^2}{\omega_0^2 - \omega^2 - i\gamma\omega}\epsilon_0 E .$$

Recall that

$$\omega_p^2 = \frac{N_0 e^2}{m\epsilon_0} .$$

Since,

$$P = \chi\epsilon_0 E ,$$

one gets

$$\chi = \frac{\omega_p^2}{\omega_0^2 - \omega^2 - i\gamma\omega}$$

and the relative dielectric constant $\epsilon = \epsilon_0\epsilon_r$ is

$$\epsilon_r = 1 + \chi = 1 + \frac{\omega_p^2}{\omega_0^2 - \omega^2 - i\gamma\omega} = \epsilon_1 + i\epsilon_2$$

where ϵ_1 and ϵ_2 are the real and imaginary parts of ϵ_r. Since

$$1 + \frac{\omega_p^2}{\omega_0^2 - \omega^2 - i\gamma\omega} = 1 + \frac{\omega_p^2(\omega_0^2 - \omega^2)}{(\omega_0^2 - \omega^2)^2 + \gamma^2\omega^2} + i\frac{\omega_p^2\gamma\omega}{(\omega_0^2 - \omega^2)^2 + \gamma^2\omega^2}$$

we obtain

$$\epsilon_1 = 1 + \frac{\omega_p^2(\omega_0^2 - \omega^2)}{(\omega_0^2 - \omega^2)^2 + \gamma^2\omega^2} \quad , \qquad \epsilon_2 = \frac{\omega_p^2\gamma\omega}{(\omega_0^2 - \omega^2)^2 + \gamma^2\omega^2} . \tag{5.2}$$

The complex refractive index is calculated from ϵ_r as

$$N = \sqrt{\epsilon_r}$$

or

$$\epsilon_1 = n^2 - k^2 \tag{5.3}$$

$$\epsilon_2 = 2nk \tag{5.4}$$

$$n = \sqrt{\frac{\epsilon_1}{2} + \frac{1}{2}\sqrt{\epsilon_1^2 + \epsilon_2^2}} \tag{5.5}$$

$$k = \frac{\epsilon_2}{2n} \, . \tag{5.6}$$

where k is the extinction coefficient, and n is the refractive index. There is a relation between k and the absorption coefficient α of Beer's law

$$I(x) = I_0 \, e^{-\alpha x} \tag{5.7}$$

by the formula

$$\alpha = \frac{4\pi k}{\lambda} \, , \tag{5.8}$$

where λ is the wavelength. Thus, the amount of absorption is determined by the imaginary part ϵ_2 of the dielectric function determines. For $|\epsilon_1| >> |\epsilon_2|$, the real part n of the refractive index, calculating how much the polarization of the material reduces the propagating waves' phase velocity, is mainly determined by ϵ_1 [54].

Lorentz model reduces to Drude model if there is no spring term ($\omega_0 = 0$),

$$\epsilon_r = 1 - \frac{\omega_p^2}{\omega^2 + i\gamma\omega} \tag{5.9}$$

$$\epsilon_1 = 1 - \frac{\omega_p^2}{\omega^2 + \gamma^2} \quad , \quad \epsilon_2 = \frac{\omega_p^2 \gamma}{\omega^2(\omega + \gamma^2)} \, . \tag{5.10}$$

Lorentz model is useful for describing the optical properties of thin films consisting of separated islands [62].

It is useful to study Equation (5.9) for different frequencies with regard to the collision

frequency γ. For convenience, let $\tau = \frac{1}{\gamma}$, and hence (5.10) can be written as

$$\epsilon_1 = 1 - \frac{\omega_p^2 \tau^2}{1 + \omega^2 \tau^2} \tag{5.11}$$

$$\epsilon_2 = \frac{\omega_p^2 \tau}{\omega(1 + \omega^2 \tau^2)} \, . \tag{5.12}$$

Metals retain their metallic character at frequencies $\omega < \omega_p$. For large frequencies close to ω_p, where $\omega\tau >> 1$, (5.9) is mainly real (i.e., $i\gamma\omega$ is negligible), and becomes

$$\epsilon_r = 1 - \frac{\omega_p^2}{1 + \omega^2} \, . \tag{5.13}$$

We can consider Equation (5.13) as the dielectric function of the undamped free electron plasma.

For very low frequencies, i.e. $\omega\tau << 1$, since $|\epsilon_2| >> |\epsilon_1|$ the real and the imaginary part of N have comparable magnitude with

$$n \approx k = \sqrt{\frac{\epsilon_2}{2}} = \sqrt{\frac{\tau \omega_p^2}{2\omega}} \, .$$

In this regime, metals are highly absorbing.

5.3.4.1. Surface Plasmon Resonance

According to the laws of refraction

$$n_1 \, \sin\theta_1 = n_2 \, \sin\theta_2 \, ,$$

where n_1 and n_2 are indexes of refraction in two mediums.

Let us suppose in glass with $n = 1,5$ a light beam hits the surface under an angle of 45^0. Since $n_{air} = 1$ we get

$$\sin\theta_{air} > 1$$

so that θ_{air} does not exist, since the maximum value of θ_{air} is 1. This shows that the light is totally reflected at the glass-air interface.

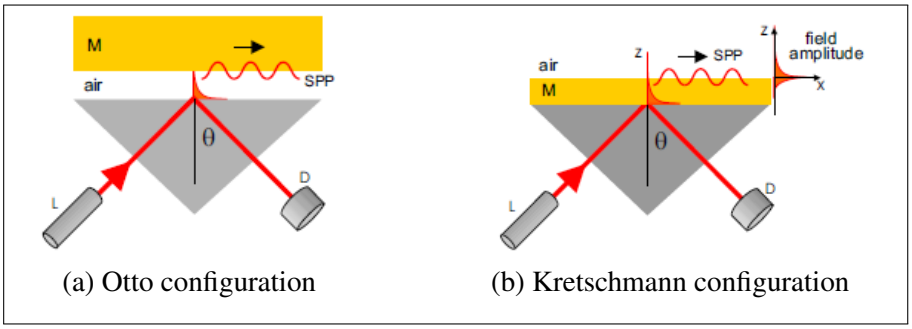
The angle of total reflection θ_T is given by $\theta_1 = 90^0$

$$\theta_T = \sin^{-1} \frac{n_1}{n_2} .$$

For theair-glass interface mentioned above, $\theta_T = 41.81^0$.

Measurement of the angle of total reflection known index of refraction of the material gives an excellent calibration of the angle of incidence. If $\theta > \theta_T$, the reflection is 100%. If $\theta \geq \theta_T$, the transmission looks like a square root function.

At metal-dielectric interfaces, i.e. silver-air, the density of free electrons changes. Metals have a pool of free electrons while there are no free electrons in a dielectric. Similar to the waves on the sea there are electron density waves at the surface, which are called surface plasma oscillations (SPO). However, at a given frequency ν these SPO have a k_x value which cannot be reached by light. Therefore a trick is needed to excite SPO with light. Using a prism with the index of refraction n_p increases the k_x value by a factor of n_p. There are two possible arrangements so-called Otto method and Kretschmann method as shown in Figure 5.21.



(a) Otto configuration (b) Kretschmann configuration

Figure 5.21. Excitation of surface plasmons (D:Dedector, L:Laser,M:metal)

SPO are excited at the metal-air interface, this causes a resonant electric field at the interface and resonant absorption there. The absorbed energy is lost in reflection.

Evaluation of the reflection curve allows us to determine the optical constants and the thickness of the metal film with high precision. Supposing a measurement error of 1% we get ε_r, ε_i and d with a sensitivity of 0.3, 2, and 5%, respectively.

Depending on the type of metal and substrate, and the deposition process the percolation

thickness can be around $6 - 15\,nm$. At percolation thickness, a SPO on the surface of the metal film can be excited by light. The clusters are separated at lower thickness, therefore the SPO could not occur. Instead, some cluster plasmon might exist.

In the resonance wavelengths, the light wave passes through the metal film, and its tail leads to the excitation of a similar SPO on the metal film's other surface. Since the two SPO are in resonance, a powerful wave appears on the metal film's opposite side. Hence, the light wave induces a resonance and arises on the opposite side of the film anyhow amplified rather than being absorbed. As a result, the light is transmitted with a low absorption. If the metal thickness is increased further, the first SPO can not excite the other surface since the surfaces become distant. In addition, the absorption is enhanced as the thickness increases.

5.3.4.2. Plasmonic Quality Factor

The considerations about SPR intensity can be quantified by the plasmonic quality factor Q_{SPR} [64] defined as

$$Q_{SPR} = -\frac{\epsilon_1}{\epsilon_2}\,.$$

Figure 5.22 shows the SPR intensity of titanium. The SPR quality factor of titanium is very small compared to silver and copper as shown in Figure 5.23. Therefore, it is highly striking that ITI multilayer thin films show SPR effect.

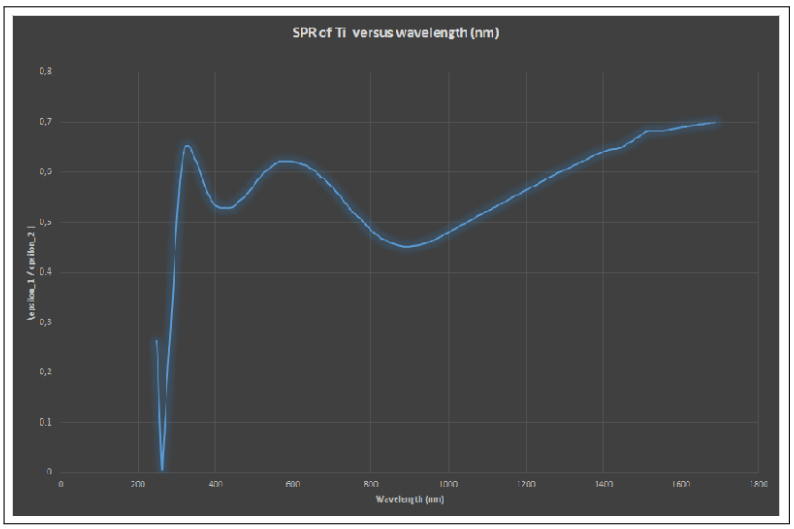


Figure 5.22. SPR intensity of Ti

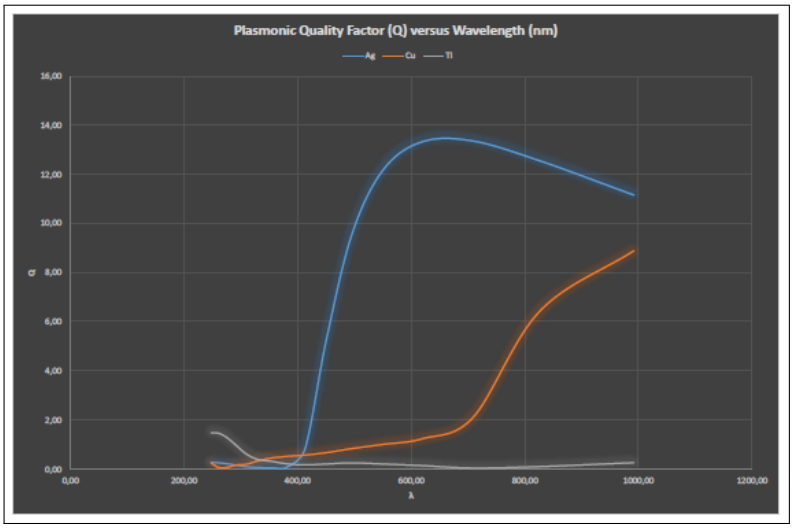


Figure 5.23. Comparison of SPR intensities of Ag, Cu, and Ti

6. COLD ATMOSPHERIC PLASMA TREATMENT OF TURKISH TEA SEEDS

6.1. PLASMA AGRICULTURE

Plasma agriculture is an emerging and innovative field that uses plasma in farming, food production, food processing, and food preservation. Plasmas can be used in agriculture to eliminate all bacterial, fungal, and viral particles from fruits and vegetables. By adding plasma to water to raise the nitrogen content, it can also be utilized to improve plant germination, and it can be also used as disinfection agent in agriculture.

In north-eastern region of Turkey (Black Sea coast) $832 \times 10^6\ kg$ tea were produced by about 200.000 farmers in 2017. Yearly yield of Turkish tea changes between 125 and $135 \times 10^7\ kg$ depending on climate conditions and technical measures [66]. Due to its importance for Turkish economy, tea was chosen to study.

6.2. PLASMA TREATMENT OF TEA

There is little research on cold plasma treatment of tea (Camellia Sinensis [L.] Kuntze) as shown in Table 6.1. The investigations include antibacterial efficacy (ABE), antioxidant activity (AOA), total phenolic content (TPC), total flavonoid content (TFC), volatile compounds profile, microstructure, and sensory properties. Most of the articles are related to the treatment of leaves. Our study is the only work on seed treatment with cold plasma. dielectric-barrier discharge (DBD) plasma is the most commonly used plasma source. Its activity against microorganisms is overwhelmingly investigated.

Kuloba et al. [67] employed nitrogen plasma in the withering stage of tea production to examine its impact on the polyphenol content. They showed that one-hour plasma treatment of green tea leaf gave the highest polyphenol content of $78.56\,mg/g$. The polyphenol concentrations of tea withered with plasma were less than the control group.

Amini and Ghoranneviss [68] discovered that the microorganisms populations in black and green tea were dramatically reduced by this plasma system. Furthermore, the treatment

Table 6.1. Literatur review on plasma treatment of tea

Ref.	Plasma Sources	Type of Tea	Investigations
[67]	DBD	Green tea leaf	Polyphenol content
[68]	Plasma Jet	Black and green tea	ABE, TPC
[69]	DBD	Green tea powder	ABE, flavor component analysis
[70,71]	Plasma Jet		ABE
[72]	DBD	Herbal tea	ABE
[73]	DBD	Green tea leaf	AOA, TPC
[74]	DBD	Green tea powder	TFC, TPC, AOA

period and the type of microorganisms affect the decontamination rate.

Hamajima et al. used cylindrical DBD plasma in the inactivation of E. coli adhering to the tea powder. They reported a 3-fold reduction in E. coli concentration [69] .

Abbasian et al. demonstrated that plasma treatment significantly lowers time-dependent toxins concentrations [70,71].

Chingsungnoen et al. [72] used a low-pressure capacitively coupled discharge plasma to treat herbal tea and to investigate its antibacterial efficacy of it. D-values of 0.73 and $0.67\,min$ were found, respectively, for the decrease of E. coli and S. aureus.

Keshavarzi et al. [73] investigated DBD plasma's capacity to improve the extraction of green tea leaves' TPC and AOA. They demonstrated that after $15\,min$ at $15\,W$ electricity, green tea's TPC and AOA increased by roughly 40%.

Hemmati et al. [74] investigated how cold plasma treatment of green tea powder affected its microstructure, sensory qualities, TPC, TFC, AOA, volatile chemicals profile, and microbiological safety. They demonstrated that 4 or $6\,min$ of plasma treatment at $22\,kV$ significantly reduced the microbial load while preserving the TPC, TFC, AOA, volatile components, and sensory appeal.

The work presented here is the first study on Turkish tea and tea seeds using atmospheric cold plasma.

6.3. EXPERIMENTAL WORK

The experiments were carried out in Trabzon province during the year $2017 - 2021$ under closed and open field conditions. The experimental set-up with atmospheric pressure cold plasma jet is shown in Figure 6.1. The experimental parameters are given in Table 6.2. The seeds collected from local farmland were exposed to various durations of air plasma treatment using CAPPJ (ELES, Turkey). The high power supply provides a maximum voltage of $20\,kV$ at $20\,kHz$.

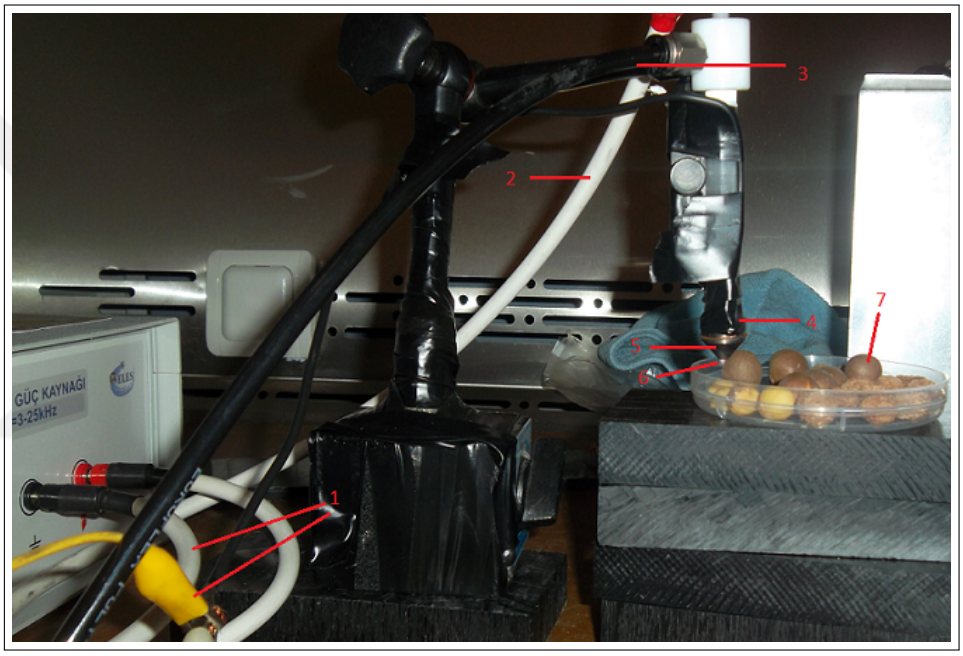


Figure 6.1. Home-made CAP system: 1) Earthing, 2) HV electrode, 3) air inlet, 4) ground electrode, 5) nozzle, 6) plasma plume, and 7) tea seeds

Table 6.2. Process parameters for seed treatment

Parameters	Quantity
Voltage (kV)	18
Frequency (kHz)	12
Airflow (L/min)	10
Exposure time (min)	2 to 10
Seed-to-Plasma Distance (mm)	25-50

The experiments started in November 2017. Seeds were pre-treated for only $4\,min$ using cold plasma jet shown in Figure 6.1. Then, they were soaked into the potting soil and replicated

three times. In 2019, the seeds were pre-treated for various durations of $2, 4, 6, 8$, and 10 minutes. For each treatment time, the samples were replicated three times. All treated seeds were soaked into pots containing 8 seeds. Middle of May, the seeds started to germinate. The ideal conditions for tea seeds are:

- Humidity: $> 70\%$
- Temperature: day $23 - 25°C$ at night $17 - 19\,°C$
- There should be no big difference between day and night temperatures

6.4. RESULTS AND DISCUSSION

6.4.1. Seed Germination and Seedling Growth

The plasma-treated samples (PTS) and the controlled samples of the $2017 - 2018$ and 2019 sets are shown in Figure 6.2, 6.3, and 6.4, respectively. The average length of the seeds treated by cold plasma is $15\,cm$, whereas the control group has an average of $5\,cm$ of $2017 - 2018$. There was no difference in the length of the samples of the 2019 set, but the plasma-treated samples started to grow ten days earlier than the control group. This is attributed to the significant difference between day and night temperatures, which is not favorable, during 2019 season. It was heavy rain mostly.



(a) (b)

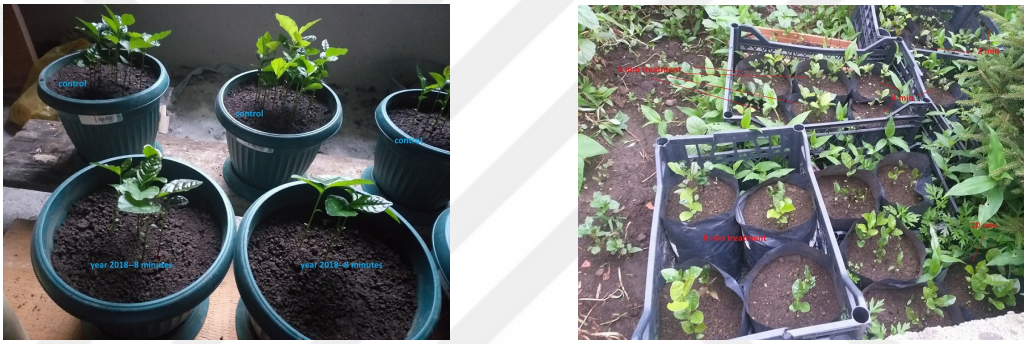
Figure 6.2. Plasma-treated samples are 3-fold greater than the controlled group

There was no difference between the laboratory environment and outside area samples, but



(a) (b)

Figure 6.3. (a) 2-minute, and (b) 4-minute PTS and the control sample



(a) 8-minute PTS and the control samples

(b) 2- to 10-minute PTS and the control samples (open field)

Figure 6.4. 2019 set

most of the samples grown in a closed environment infested by a broad mite (P. Latus). Therefore, characterization studies were conducted on the samples of open field.

The number of germinated seeds was recorded daily. Stem length, shoot length, and shoot width were measured. Based on these data, seed germination (SG), germination index (GI), and seedling vigour index (SVI) were calculated according to the formulas:

$$SG = \frac{\text{The number of the germinated seeds}}{\text{Total number of the seeds}} \times 100$$

$$GI = \sum_{i}^{n} \frac{\text{The number of the germinated seeds}}{\text{The number of the days}}$$

$$SVI = SG \times \text{Seedling length (mm)}$$

Figure 6.5 shows the graph of seed germination rate. At the beginning, 2 and 10 – *min* PTS grew faster. As seen from Figure 6.6, 2 – *min* PTS have the highest germination percentage, and 10 – *min* PTS seems to have the second best germination capability. Similarly, 2 and 10 – *min* PTS have the highest germination index (around 6).

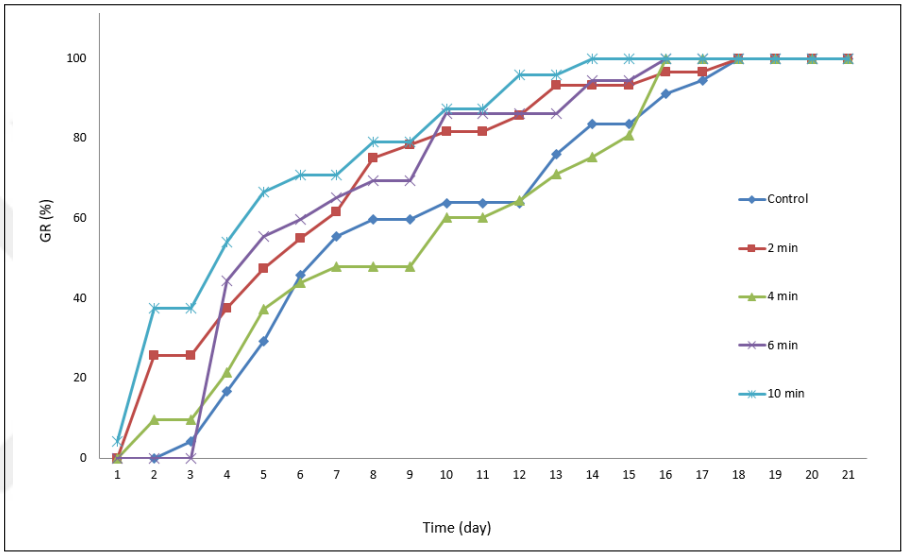


Figure 6.5. Seed germination rate

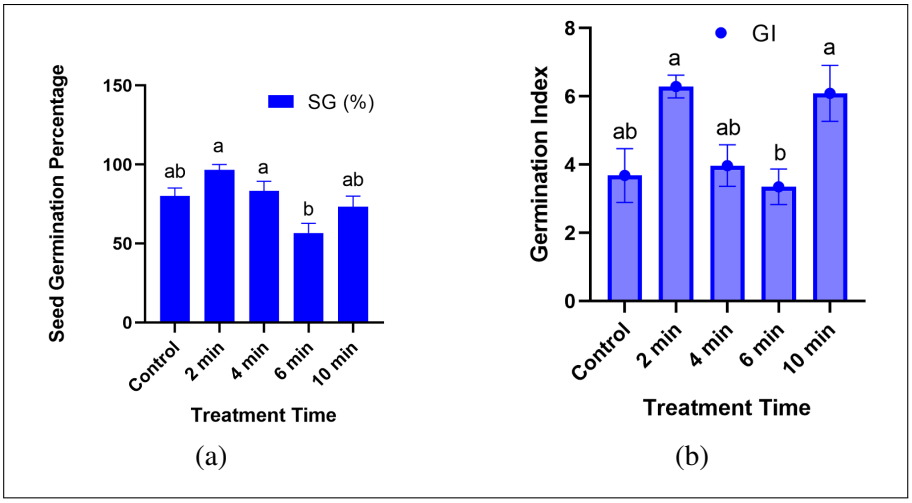
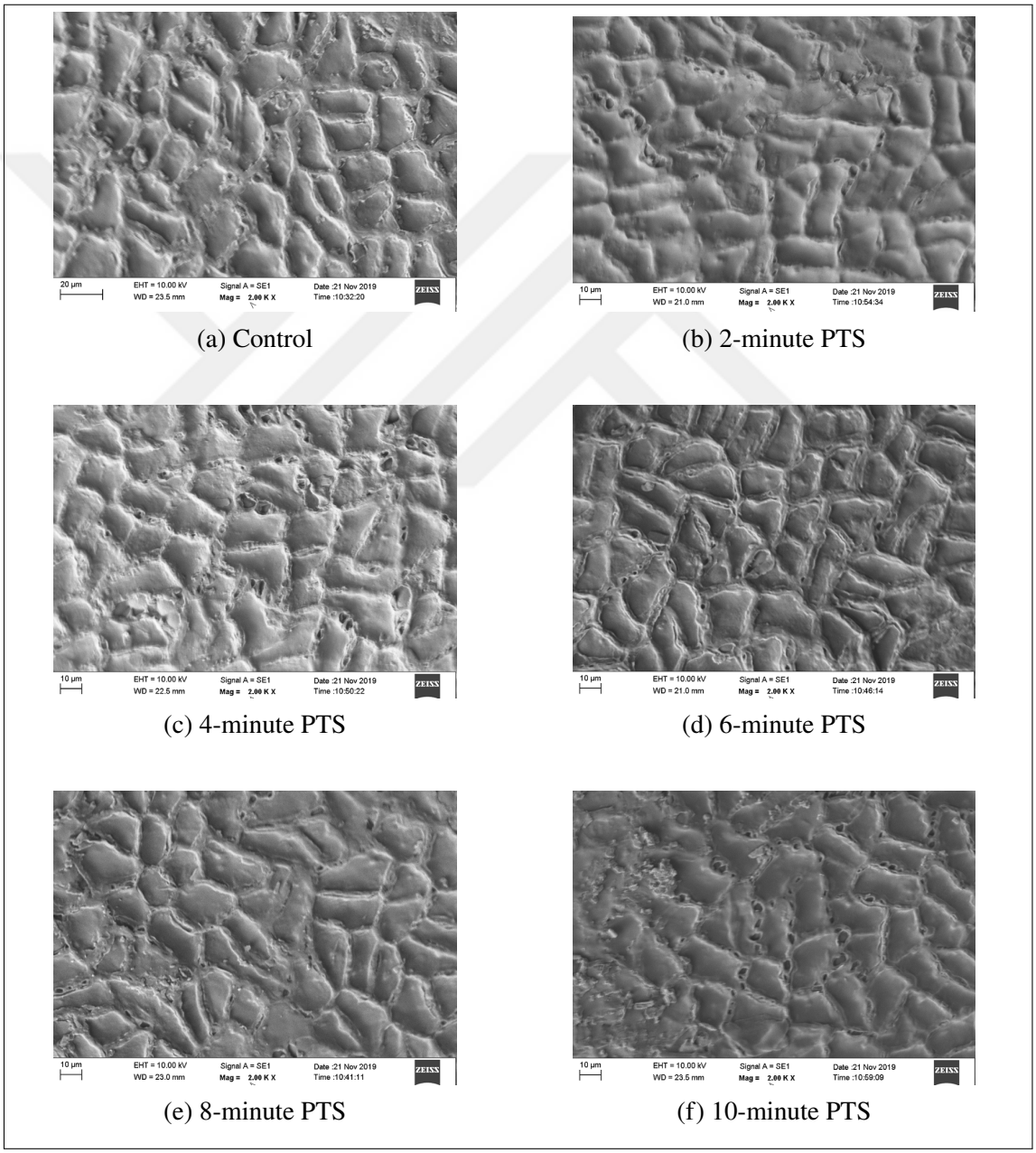


Figure 6.6. (a) Seed germination percentage, (b) Germination index

6.4.2. Surface Properties

Surface properties were monitored by SEM (ZEISS, $20K$ magnification) at the Nanotechnology Laboratory of Yeditepe University. The apparent difference between control and PTS as shown in Figure 6.7 is the black spots on the surface of PTS, which can be attributed to ozone created by cold plasma jet. We have not seen eroded seed coats in the experiments.



(a) Control (b) 2-minute PTS

(c) 4-minute PTS (d) 6-minute PTS

(e) 8-minute PTS (f) 10-minute PTS

Figure 6.7. SEM images plasma treated and untreated tea seeds

6.4.3. Plant Hormones and Antioxidant Enzyme Activity

In 2021, the experiments were repeated at room temperature. The temperature of seed surface after plasma treatment was kept below $45°C$. 6 replicates have been prepared for each treatment time. After 25 days, the seeds became to sprout and following 21 days, germination was completed. Accordingly, seed germination, germination rate, and seedling vigor index were calculated. Since there were 3 replicate for 8 minute plasma treated seeds (PTS), the germination calculations for 8-min PTS was omitted. All data are expressed as the mean plus standard deviation. The one-way analysis of variance (ANOVA) followed by Tukey's HSD test was used for statistics via GraphPad Prism 9.0 software.

By using High-Performance Liquid Chromatography (HPLC), antioxidant enzymes, and hormones which are listed in Table 6.3 were identified and quantified.

Table 6.3. Investigated phytohormones and antioxidant enzymes.

	Name	Abbreviation	Unit
Enzymes	Catalase	CAT	$EU\,gr\,leaf$
	Peroxidase	POD	$EU\,gr\,leaf$
	Superoxide Dismutase	SOD	$EU\,gr\,leaf$
	Hydrogen Peroxide	H_2O_2	$m\,mol/kg$
	Malondialdehyde	MDA	$m\,mol/kg$
Hormones	Abscisic Acid	ABA	$ng/g\,DW$
	Gibberellic Acid	GA	$ng/g\,DW$
	Indol 3-Asetic Acid	IAA	$ng/g\,DW$
	Cytokinin	CK	$ng/g\,DW$
	Zeatin	Z	$ng/g\,DW$
	Jasmonic Acid	JA	$ng/g\,DW$

Plasma treatment increases reactive oxygen species (ROS) in the plant (i.e. Equation 6.1) cause oxidative stress, which is harmful to living plant cells. Plants have an enzymatic defense mechanism as a result. Since ROS also function as signaling molecules that aid in controlling plant growth, these enzymes are antioxidants in nature and control the quantity of ROS in plants [76]. SOD enzyme is the frontrunner for defense against oxidative stress, converting O_2^- radical to O_2 and H_2O_2 (Equation 6.2). CAT enzyme catalyzes H_2O_2 in the plant to O_2 and H_2O (Equation 6.3), thus, it helps to control the H_2O_2 level in the plant. POD is an enzyme found in electron donor proteins, and it catalyzes the oxidation of compounds

(Equation 6.4). Additionally, POD is vital for plants' defensive mechanisms against plant diseases. MDA is a biomarker for lipid peroxidation. MDA concentration increases with time as H_2O_2 increases as shown in Figure 6.8e and 6.8d. Sucrose is the main sugar used as an energy source and a signaling entity in plants.

$$\mathrm{O_2} \xrightarrow{\text{plasma}} \mathrm{O_2^{\cdot -}} \tag{6.1}$$

$$2\,\mathrm{HO_2} \xrightarrow{\text{SOD}} \mathrm{O_2 + H_2O_2} \tag{6.2}$$

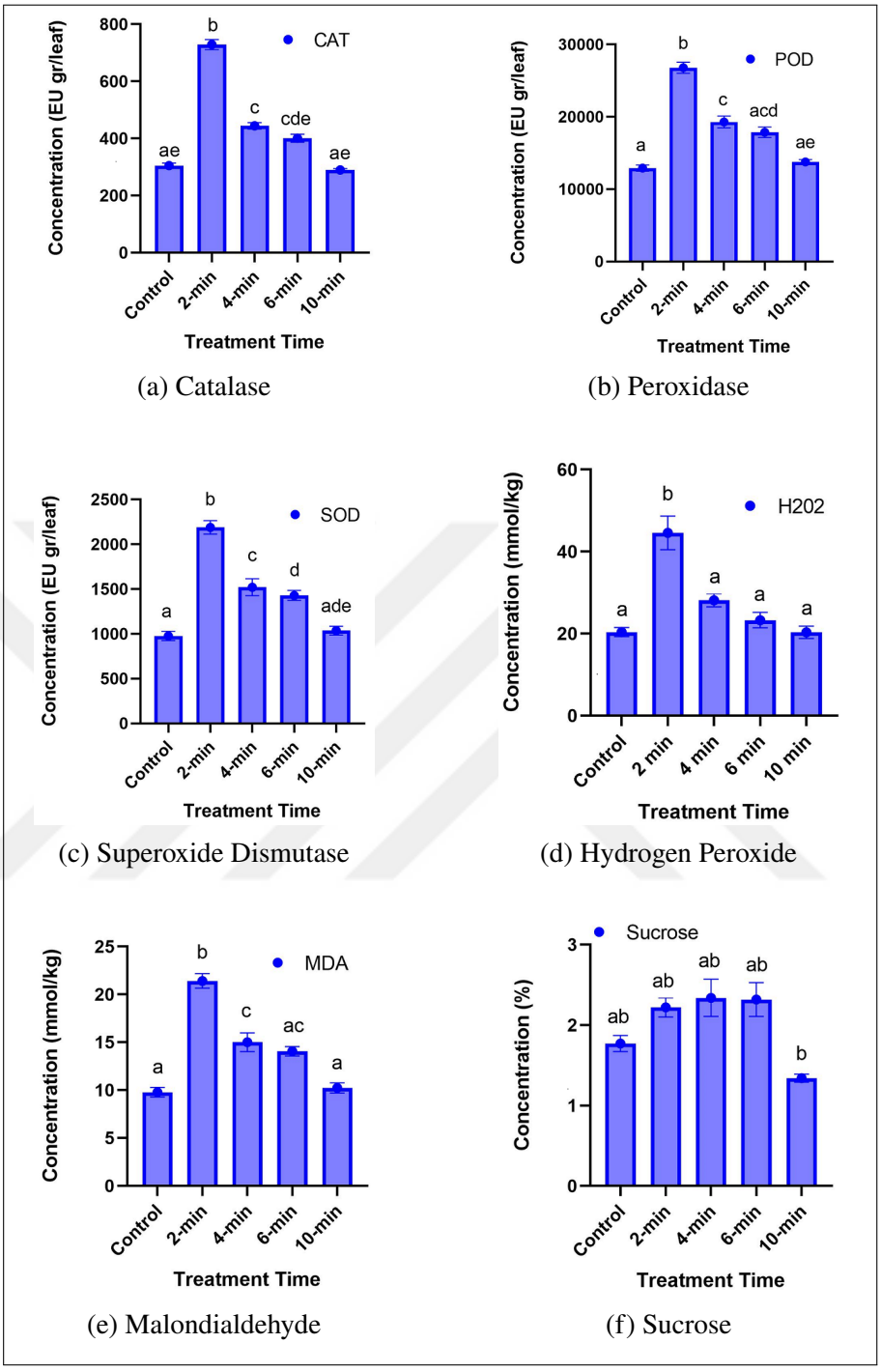
$$2\,\mathrm{H_2O_2} \xrightarrow{\text{CAT}} 2\,\mathrm{H_2O + O_2} \tag{6.3}$$

$$\mathrm{ROOR^{'} + 2e^{-} + H^{+}} \xrightarrow{\text{POD}} \mathrm{ROH + R^{'}OH} \tag{6.4}$$

Seed germination is a complex process controlled by numerous plant hormones. Among them, the competition between gibberellic acid (GA) and abscisic acid (ABA) is crucial in regulating seed germination. As shown in Figure 6.9a and 6.9b, ABA concentration decreases steadily while GA concentration increases with ascending treatment time.

Our results have indicated that the antioxidant enzymes and plant hormones activities were affected by cold plasma treatment as shown in Figure 6.8 and 6.9. It is evident that low treatment time promotes antioxidant enzyme activity, and high exposure time increases plant hormone activity.

In summary, we can state that cold plasma treatment affects seed germination and seedling growth, and changes phytohormone balance and antioxidant enzyme activity of tea.

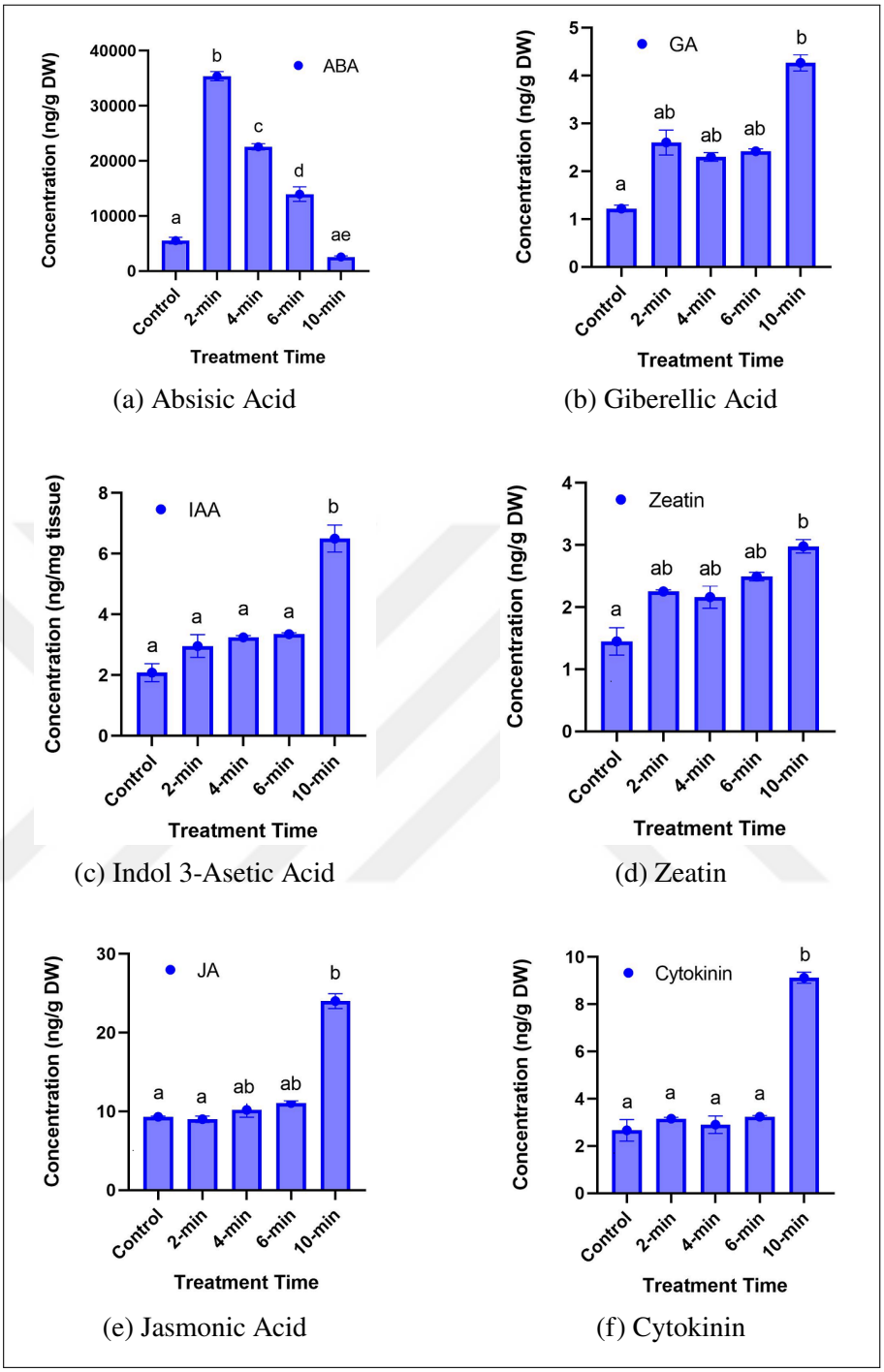


(a) Catalase (b) Peroxidase

(c) Superoxide Dismutase (d) Hydrogen Peroxide

(e) Malondialdehyde (f) Sucrose

Figure 6.8. HPLC results for antioxidant enzyme activities



(a) Absisic Acid

(b) Giberellic Acid

(c) Indol 3-Asetic Acid

(d) Zeatin

(e) Jasmonic Acid

(f) Cytokinin

Figure 6.9. HPLC results for plant hormones activities

7. CONCLUSIONS

In this dissertation, the utilization and characterization of low and atmospheric pressure plasmas in medicine, energy, and agriculture have been experimentally studied. The main results and original scientific contributions are as follows:

- The antibacterial efficacy of Ag or Cu coated cotton is greater than the uncoated ones; and Ag is more effective towards E. coli and S. aureus bacteria than Cu.
- We have used Ti alone in the sandwich structure of ITO/Ti/ITO, and shown that ITI multilayer thin films can be used as transparent conducting electrode production.
- We demonstrated for the first time that Ti in ITO/Ti/ITO structure shows SPR effect.
- We demonstrated for the first time that cold atmospheric plasma treatment promotes seed germination and seedling growth of tea by changing plant hormone and antioxidant enzyme activities.

REFERENCES

1. Chen FF. *Introduction to plasma physics and controlled fusion*. Springer International Publishing; 2016.

2. Hoffmann C, Berganza C, Zhang J. Cold atmospheric plasma: methods of production and application in dentistry and oncology. *Medical Gas Research*. 2013;3(21):1-15.

3. Gurnett DA, Bhattacharjee A. *Introduction to plasma physics with space, laboratory and astrophysical applications*. Cambridge University press; 2017.

4. Jögi I. Characteristics and classification of plasmas. PlasTEP trainings course and Summer school 2011, Warsaw.

5. Keudell AV, Gathen VS. Foundations of low temperature plasma physics-an introduction. *Plasma Sources and Science and Technology*. 2017;26:11301.

6. Eliezer S, Eliezer Y. *The fourth state of matter: An introduction to plasma science*. IOP; 2001.

7. Chopra KL, Kaur I. *Thin film device applications*. Plenum Press; 1983.

8. Movchan BA, Demchishin AV. Structure and properties of thick condensates of Ni, Ti, W, Al_2O_3 and ZrO_2 in vacuum (in Russian). *Physics of Metals and Metallography*. 1969;28:653-60.

9. Thornton JA. Influence of apparatus geometry and deposition conditions on the structure and topography of thick sputtered coatings. *Journal of Vacuum Science and Technology*. 1974;11:666-70

10. Anders A. A structure zone diagram including plasma-based deposition and ion etching. *Thin Solid Films*. 2010;518(15):4087-90.

11. Kaiser N. Review of the fundamentals of thin-film growth. *Applied Optics*. 2002;41(16):3053-60.

12. Oura K, Katayama M, Zotov AV, Lifshits VG, Saranin AA. Growth of thin films. *Surface*

Science. 2003:357-387.

13. Greene JE. Thin film nucleation, growth, and microstructural evolution: An atomic scale view. 0 *Handbook of deposition technologies for films and coatings*. 2010:554-620.

14. Shigesato S, Koshi-ishi R, Kawashima T, Ohsako J. Early stages of ITO deposition on glass or polymer substrates. *Vacuum*. 2000;59(2-3):614-21.

15. Bogaerts M. Plasma diagnostics and numerical simulations: insight into the heart of analytical glow discharges. *Journal of Analytical Atomic Spectrometry*. 2007;22:13-40.

16. Varvara E. Study in analytical glow discharge spectrometry and its application in materials science. Doctoras Thesis, TUD, 2011.

17. Chapman BN. *Glow discharge processes-Sputtering and plasma etching*. John Wiley and Sons; 1980.

18. Baer DR, Thevuthasan S. Characterization of thin films and coatings. *Handbook of deposition technologies for films and coatings*. 2010:749-864.

19. Honsberg C, Bowden S's homepage [Cited 2022 31 May]. Avaliable from: http://pveducation.org/pvcdrom/characterisation/four-point-probe-resistivity-measurements.

20. Valdes LB. Resistivity measurements on germanium for transistors. *Proceeding of I.R.E.*. 1954;42:420-7.

21. Smith FM. Measurement of sheet resistivity with the four point probe. *The Bell System Technical Journal*. 1957;(37)3:711-18.

22. Schroder DK. *Semiconductor material and device characterization*. John Wiley and Sons; 2006.

23. Ohring M. *Materials Science of Thin Films*. Academic Press; 2002.

24. Horcas I, Fernandez R. WSXM: A software for scanning probe microscopy and a tool for nanotechnology. *Review of Scientific Instruments*. 2007;78:013705.

25. Hoefer D. Antimicrobial textiles - Evaluation of their effectiveness and safety. *Current problems of dermatology*. 2006;33:43-50.

26. Baron S. *Medical microbiology*. Churchill Livingstone; 1996.

27. Madigan MT, Martinko JM, Parker J. *Brock biology of microorganisms*. Prentice-Hall; 2000.

28. HPLC Separation Fundamentals: Agilent; [Cited 2022 11 November]. Avaliable from: https://www.agilent.com/slidepresentation/Public.

29. Perelshtein I, Applerot G. Perkas N, Guibert G, Mikhailov S, Gedanken A. Sonochemical coating of silver nanoparticles on textile fabrics (nylon, polyester and cotton) and their antibacterial activity. *Nanotechnology*. 2008;19:245705.

30. Pohle D, Damn C, Neuhof J, Roesch A, Muenstedt H. Antimicrobial properties of orthopaedic textiles after in-situ deposition of silver nanoparticles. *Polymers and Polymer Composites*. 2007;15(5):357-363.

31. Morones JB, Elechiguerra JL, Camacho A, Holt K, Kouri JB, Ramirez JT, Yacaman MJ. The bactericidal effect of silver nanoparticles. *Nanotechnology*. 2005;16:2346-53.

32. Damm C, Muenstedt H, Roesch A. Long-term antimicrobial polyamide 6-silver-nanocomposites. *Journal Material Science*. 2007;42:6067-73.

33. Hoskins JS, Karanfil T, Serkiz SM. Removal and sequestration of iodide using silver-impregnated activated carbon. *Environmental Science and Technology*. 2002;36(4):784-9.

34. Feng QL, Wu j, Chen GQ, Cui FZ, Kim TN, Kim JO. A mechanistic study of the antibacterial effect of silver ions on Escherichia coli and Staphylococcus aureus. *Journal of Biomedical Material Research*. 2000;52(4):662-8.

35. Kim JS. Antibacterial activity of Ag ion-containing silver nanoparticles prepared using the alcohol reduction method. *J. Ind. Eng. Chem.*. 2007;13(4):718-722.

36. Hatchett DW, White HS. Electrochemistry of sulfur adlayers on the low-index faces of silver. *Journal of Physical Chemistry*. 1996;100:9854-9.

37. Guillen C, Herrero J. TCO/metal/TCO structures for energy and flexible electronics. *Thin Solid Films*. 2011;520:1-17.

38. Minami T. Transparent conducting oxide semiconductors for transparent electrodes. *Semiconductor Science and Technology*. 2005;20(4):35-44.

39. Minibaev RF, Bagatur'yants AA, Bazhanov DI, Knizhnik AA, Alfimov MV. First principles investigation of the electron work function for the (001) surface of Indium Oxide and ITO as a function of the surface oxidation level. *Nanotechnologies in Russia*. 2010;5(3-4):185-190.

40. Jia J, Takaya A, Yonezawa T, Yamasaki K, Nakazawa H, Shigesato S. Carrier densities of Sn-doped In_2O_3 nanoparticles and their effect on XPS emission. *Journal of Applied Physics*. 2019;125:245303.

41. Lee JY, Yang JW, Chae JH, Park JH, Choi JI, Park HJ, Kim D. Dependence of intermediated noble metals on the optical and electrical properties of ITO/metal/ITO multilayers. *Optics Communications*. 2009;282:2362-66.

42. Park HJ, Park JH, Choi JI, Lee JY, Chae JH, Kim D. Fabrication of transparent conductive films with a sandwich structure composed of ITO/Cu/ITO. *Vacuum*. 2009;83:448-450.

43. Kim D. Properties of ITO/Cu/ITO multilayer films for application as low resistance transparent electrodes. *Transactions on Electrical and Electronic Materials*. 2009;10(5):165-8.

44. Kim D. Characterization of low pressure annealed ITO/Au/ITO films prepared by reactive magnetron sputtering. *Journal of Alloys and Compounds*. 2010;493(1-2):208-211.

45. Kim D. Low temperature deposition of transparent conducting ITO/Au/ITO films by reactive magnetron sputtering. *Applied Surface Science*. 2010;256(6):1774-7.

46. Cho EN, Moon P, Kim CE, Yun I. Modeling and optimization of ITO/Al/ITO multilayer films characteristics using neural network and genetic algorithm. *Expert Systems with Applications*. 2012;39(10):8885-9.

47. Park JH, Chae JH, Kim D. Influence of nickel thickness on the properties of ITO/Ni/ITO thin films. *Journal of Alloys and Compounds*. 2009;478:330-3.

48. Kim JC, Shin CH, Jeong CW, Kwon YJ, Park JH, Kim D. Investigation of conductive

and transparent ITO/Ni/ITO multilayer films deposited by a magnetron sputter process. *Nuclear Instruments and Methods in Physics Research B*. 2010;268(2):131-4.

49. Choi JI, Lee JY, Park JH, Chae JH, Park HJ, Kim D. Fabrication and characterization of Pt intermediate transparent and conducting ITO/Pt/ITO multilayer films. *Journal of Physics and Chemistry of Solids*. 2009;70(2):272-5.

50. Chen SW, Koo CH, Huang HE, Chen CH. Ag-Ti Alloy Used in ITO/Metal/ITO Transparency Conductive Thin Film with Good Durability against Moisture. *Materials Transactions*. 2005;46(11):2536-40.

51. Chemelli C, Maria LD, Marchionna S, Malgesini R, Pirovano G. Transparent conductive multilayer films on flexible substrate for electric field shielding application. *18th Italian National Conference on Photonic Technologies*. 2016.

52. Chen C, Wang Z, Wu K, Chong H, Xu Z, Ye H. ITO/TiN/ITO Sandwiches for Near-Infrared Plasmonic Materials. *ACS Applied Materials and Interfaces*. 2018;10:14886-14893.

53. Wikipedia contributors: Titanium [cited 2022 19 July]. Avaliable from https://en.wikipedia.org/w/index.php?title=Titanium&oldid=1099274791.

54. Maier SA. *Plasmonics:Fundamentals and Applications*. Springer, 2007.

55. Synowicki RA. Suppression of backside reflections from transparent substrates. *Physica Status Solidi C*. 2088;5(5):1085-8.

56. Ramp Procedure for Ceramic Target Conditioning: Kurt J. Lesker Company; [Cited 2022 7 July]. Avaliable from: https://www.lesker.com/newweb/deposition materials/rampprocedure ceramictarget materials.cfm?pgid=0.

57. Aslan N, Şen T, Çoruhlu T, Şenturk K, Keskin SS, Şeker S, Dobrovolsky AM. Investigation on surface, electrical and optical properties of ito-ag-ito coated glass. *Problems of Atomic Science and Technology*. 2015;1(95):256-8.

58. Kulkarni AK, Schulz KH, Lim TS, Khan M. Dependence of the sheet resistance of ITO thin films on grain size and grain orientation determined from XRD techniques *Thin Solid*

Films. 1999;345(2):273-7.

59. Kulkarni AK, Lim T. Electrical, optical, and structural properties of ITO thin films deposited on PET substrates by RF sputtering. *Journal of Vacuum Science and Technology A*. 1998;16(3):1636-40.

60. Kulkarni AK, Schulz KH, Lim TS, Khan M. Electrical, optical and structural characteristics of ITO thin films deposited on glass and polymer substrates. *Thin Solid Films*. 1997;308-309:1-7.

61. Chauhan RN, Singh I, Anand RS, Kumar J. Effect of sheet resistance and morphology of ITO thin films on polymer solar cell characteristics. *International Journal of Photoenergy*. 2012;87926.

62. Elofsson V. Nanoscale structure forming processes:Metal thin films grown far-from-equilibrium. Doctoral Thesis, Linköping University, 2016.

63. Park YS, Park HK, Jeong JA, Kim HK, Choi KH, Na SI, Kim DY. Comparative investigation of transparent IAI and ICI electrodes grown by dual-target DC sputtering for OPV. *Journal of the Electrochemical Society*. 2009;156(7):H588-H594.

64. Amendola V, Pilot R, Frasconi M, Marago OM, Iati MA. Surface plasmon resonance in gold nanoparticles: a review. *Journal of Physics: Condensed Matter*. 2017;29:203002.

65. Werner WSM, Glantschnig K, Ambrosch-Draxl C. Optical constants and inelastic electron-scattering data for 17 elemental metals. *J. Phys. Chem. Ref. Data*. 2009;38(4):1013-92.

66. Seyis F, Yurteri E, Ozcan A, Savsatli Y. Organic tea production and tea breeding in Turkey: Challenges and possibilities. *Ekin Journal*. 2018;4(1):60-69.

67. Kuloba PW, Gumbe LO, Okoth MW, Obanda M, Nganga FM. An investigation into low-temperature nitrogen plasma environment effect on the content of polyphenols during withering in made Kenyan tea. *International Journal of Food Science & Technology*. 2014;49(4):1020-26.

68. Amini M, Ghoranneviss M. Black and green tea decontamination by cold plasma.

Research Journal of Microbiology. 2016;11:42-46.

69. Hamajima S. Kawamura N., Nagatsu M. Low-temperature disinfection of tea powders using non-equilibrium atmospheric pressure plasma. *Recent global research and education:technological challenges, advances in intelligent systems and computing 519*. Springer International Publishing AG; 2017:269-75.

70. Abbasian EG, Bayat M, Nosrati AC, Hashemi SJ, Ghoranneviss M. Study of the effect of plasma jet on Fusarium isolates with ability to produce DON toxins. *Clinical Research and Methods*. 2017;15(9):204-7.

71. Abbasian EG, Bayat M, Nosrati AC, Hashemi SJ, Ghoranneviss M. The effect of atmospheric plasma jet on Fusarium species producing mycotoxins T2 and DON: An approach for physical and chemical investigation. *Euroasian Chemical Communication*. 2020;2(3):340-8.

72. Chingsungnoen A, Maneerat S, Chunpeng P, Poolcharuansin P, Nam-Matra R. Antimicrobial treatment of E. coli and S. aureus in herbal tea using low-temperature plasma. *Journal of Food Protection*. 2018;81(9):1503-7.

73. Keshavarzi M, Najafi G, Gavlighi HA, Seyfi P, Ghomi H. Enhancement of polyphenolic content extraction rate with maximal antioxidant activity from green tea leaves by cold plasma. *Journal of Food Science*. 2020;85(10):3415-22.

74. Hemmati V, Garavand F, Khorshidian N, Cacciotti I, Goudarzi M, Chaichi M, Tiwari BK. Impact of cold atmospheric plasma on microbial safety, total phenolic and flavonoid contents, antioxidant activity, volatile compounds, surface morphology, and sensory quality of green tea powder. *Food Bioscience*. 2020;44A:1-8.

75. Shu K. Zhou W, Chen F, Luo X, Yang W. Abscisic acid and gibberellins antagonistically mediate plant development and abiotic stress responses. *Frontiers in Plant Science*. 2018;9(416):1-8.

76. Rathore V, Tiwari BS, Nema SK. Treatment of pea seeds with PAW to enhance germination, plant growth, and plant composition. *Plasma Chemistry and Plasma Processing*. 2022;42:109-29.